The role of primary cilia in adipose tissue

Doctoral thesis

to obtain a doctorate (PhD)

from the Faculty of Medicine

of the University of Bonn

Maria Katharina Sieckmann

from Düsseldorf, Germany

2025

Written with authorization of

the Faculty of Medicine of the University of Bonn

First reviewer: Prof. Dr. Dagmar Wachten

Second reviewer: Prof. Dr. Elvira Mass

Day of oral examination: 18.06.2025

From the Institute of Innate Immunity

Table of Contents

List of abbreviations

AC	Adenylyl cyclase
AgRP	Agouti-related protein
AKP	A-kinase anchoring protein
ANOVA	Analysis of variance
APC	Adipocyte Progenitor Cell
BBS	Bardet-Biedl-Syndrome
BSA	Bovine serum albumin
C/EBP	CCAAT-enhancer-binding protein
cAMP	Cyclic adenosine monophosphate
CCT	Chaperonin containing tailless complex polypeptide 1
CD	Cluster of differentiation
CEBPβ	CCAAT-enhancer-binding protein β
CREB	cAMP responsive element-binding protein
DAG	Diacylglycerol
DAPI	4′,6-Diamidin-2-phenylindol
DC	Dendritic cell
DEG	Differently expressed genes
DHH	Desert Hedgehog
DMSO	Dimethylsulfoxide
DN	Double negative
DNA	Deoxyribonucleic acid
DP	Double positive
DPP4	Dipeptidyl peptidase 4
ECM	Extracellular matrix
EDTA	Ethylenediaminetetraacetic acid
EMT	Epithelial-to-mesenchymal transition
ERK	Extracellular-related kinase
FABP4	Fatty-acid acid binding protein 4
FACS	Flourescence-activated cell sorting
FAP	Fibro-/adipogenic progenitor

FFAR4	ω-3 free fatty-acid receptor 4
FIP	Fibro-inflammatory progenitors
FlpE	FLP1 recombinase
FPC	Fibrogenic Precursor Cells
FRT	Flippase recognition target
FTOC	Fetal thymic organ culture
GEF	Rho guanine exchange factor
GLI	Glioma-associated transcription factors
GLI-FL	Full-length glioma-associated transcription factors
GLI-R	Glioma-associated transcription factor repressor form
GO	Gene ontology
GPCR	G-protein coupled receptors
gWAT	Gonadal white adipose tissue
HFD	High-fat diet
Hh	Hedgehog
IBMX	Isobutylmethylxantine
IFT	Intraflagellar transport
IGF1R	Insulin growth factor 1 receptor
IHH	Indian Hedgehog
ILC	Innate lymphoid cell
IP3	Inositol 1,4,5-triphosphate
iWAT	Inginal white adipse tissue
lacZ	β-galactosidase
MACS	Magnetic-activated cell sorting
MAP	Mitogen-activated protein
MC4R	Melanocortin-4 receptor
MCHR1	Melanin-concentrating hormone receptor
MEF	Mouse embryonic fibroblats
MFI	Median fluorescence intensity
MMP	Matrix metalloproteinase
mRNA	Messenger ribonucleic acid
MSC	Mesenchymal stem/stromal cells

mTOR	Mammalian target of rapamycin
MuSC	Muscle stem cells
n.s.	non-significant
neo	Neomycin-resistance cassette
NPY	Neuropeptide Y
NPY2R	Neuropeptide Y receptor Y2
PBS	Phosphate buffered saline
PC	Phosphatidylcholine
PCA	Principal component analysis
PCR	Polymerase chain reaction
Pdgfra	Platelet-derived growth factor receptor α
PI(4,5)P2	Phosphatidylinositol 4,5-biphosphate
PI3K	Phosphatidylinositol 3 kinase
PKA	Protein kinase A
PKA-RIα	Protein kinase A regulatory subunit I α
PLIN1	Perilipin
POMC	Pro-opiomelanocortin
PPARγ	Proliferator-activated receptor γ
PRRX1	Paired related homeobox 1
PTCH1	Patched 1
qPCR	quantitative PCR
RNAseq	RNA sequencing
RPE	Retinal pigment epithelium
RSPO2	R-spondin 2
RT	Room temperature
SAG	SMO agonist
SCA1	Stem-cell antigen
SHH	Sonic Hedgehoc
ShhN	N-terminal SHH
SMO	Smoothened
SP	Single-positive
SREB1	Sterol regulatory element-binding protein 1

SSTR3	Somatostatin receptor 3
SVF	Stromal vascular fraction
TAG	Triacyl glycerides
TEC	Thymic epithelial cell
TTR	Tetratricopeptide repeats
TGFβ	Transforming growth factor beta
TOM1L2	Target of myb1 membrane trafficking protein-like protein 2
TRA	Tissue-restricted antigens
Treg	Regulatory T cell
TULP3	Tubby-like protein 3
TZ	Transition zone
UMAP	Uniform Manifold Approximation and Projection
VEGF	Vascular endothelial growth factor
WAT	White adipose tissue
Wnt	Wingless-Int1
α-MSH	α-melanocyte-stimulating hormone

1. Introduction

1.1 The primary cilium – a sensory organelle

The primary cilium is a small, microtubule-based organelle that emanates from the plasma membrane of most vertebrate cells. In contrast to motile cilia, the primary cilium is a solitary and immotile organelle. The cilium is highly enriched in receptors, ion channels, and downstream effectors enabling the sensing of local signals and transduction of this information into a cellular response (Wachten & Mick, 2021).

1.1.1 Structure and organization of the primary cilium

The axoneme is the core of the primary cilium and is formed by the cylindrical array of nine doublet microtubules with a 9 + 0 configuration, which extends from the mother centriole (Poole et al., 1985). The doublet microtubules are formed by a complete A-tubule and an incomplete B-tubule. Ciliary microtubules are more stable compared to microtubules in the cytoplasm to maintain cilia stability and mechanical strength (Deretic et al., 2023). This is ascribed to different microtubule-associated proteins, as well as specific post-translational modification of microtubules i.e., acetylation, glutamylation, and glycylation (Behnke & Forer, 1967; Conkar & Firat-Karalar, 2021; Wloga et al., 2017; Wloga & Gaertig, 2010).

Assembly of the cilium is dependent on the cell cycle (Gopalakrishnan et al., 2023). During specific phases of the cell cycle, the cilium is dismantled to free the mother centriole, which is part of the centrosome and functions as a microtubule organization center (Fig. 1) (S. Kim & Dynlacht, 2013). During G0/G1 phase, the mother centriole anchors to the plasma membrane, forming the basal body (Tanos et al., 2013), while the distal appendage matures into transition fibers, forming the transition zone (TZ) (Fig. 1) (Garcia-Gonzalo & Reiter, 2017). The TZ is characterized by Y-shaped linkers that connect the microtubule doublets of the axoneme to the ciliary membrane (Fig. 1). Thereby, it forms a selectively permeable diffusion barrier between the cell body and cilium (Dean et al., 2016). To pass this border, proteins are actively transported into the cilium via the intraflagellar transport (IFT) machinery (Fig. 1) (Rosenbaum & Witman, 2002). The motor protein kinesin carries the cargo-laden IFT ‘trains’ along B-microtubules from the base to

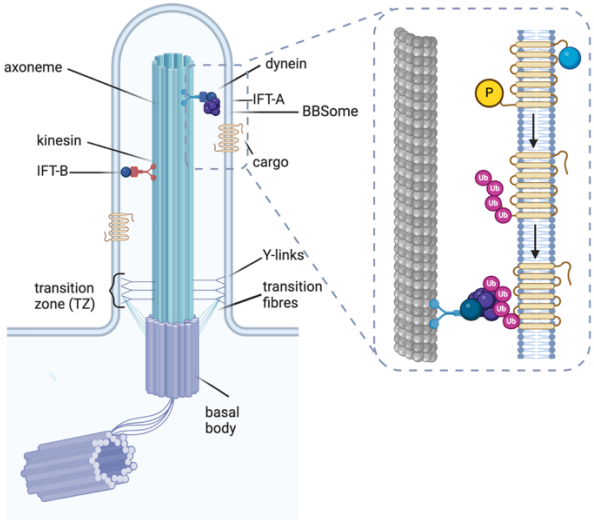

the tip of the cilium (anterograde transport). At the ciliary tip, the IFT is remodeled and moves along A-microtubules back to the base (retrograde transport), driven by the motor protein dynein (Lacey & Pigino, 2024).

Fig. 1: Structure and trafficking of the primary cilium. For further explanation, see text.

1.1.2 Ciliary trafficking

The ciliary membrane maintains a distinct lipid and protein composition, which is tightly regulated to fulfill tissue- and cell-specific functions (Garcia et al., 2018; Rohatgi & Snell, 2010). In addition to the TZ and IFT machinery, multiple proteins and protein complexes regulate ciliary trafficking. Protein entry into the cilium relies on post-translational modification, e.g., palmitoylation, prenylation, or myristylation, and a ciliary targeting sequence (Mukhopadhyay et al., 2017). The latter is recognized by the tubby-like protein (TULP3), which coordinates ciliary import of integral membrane proteins in a phosphoinositide 4,5-bisphosphate ($PI(4,5)P_2$)-dependent manner and by binding to the IFT-A core (Badgandi et al., 2017; Mukhopadhyay et al., 2010).

Ciliary exit is regulated by the BBSome, an octameric protein complex, which facilitates retrograde transport of activated G-protein coupled receptors (GPCRs) (Lechtreck et al., 2009; Nachury, 2018). Therefore, the BBSome is essential in regulating stimulus-dependent control of ciliary signaling events. Activated receptors accumulate at the ciliary tip where they are tagged for export by ubiquitination (Fig. 1) (Shinde et al., 2020). The ubiquitinated proteins couple to the BBSome and are subsequently moved towards the ciliary base, where the BBSome mediates lateral transport of the proteins across the transition zone (Fig. 1) (Gopalakrishnan et al., 2023; Ye et al., 2018).

The intricate regulation of the IFT, the TZ, and the proteins that mediate import and export are key to dynamically regulating the molecular landscape of the primary cilium.

1.1.3 The Hedgehog pathway as a model ciliary signaling pathway

The primary cilium functions as a cellular antenna by harboring specific receptors. Activation of those receptors engages signaling pathways, which transduce information by local production of second messengers, e.g., cyclic adenosine monophosphate (cAMP), and subsequently evoke an intracellular response. One of the best-described pathways that highlights this mechanism is the Hedgehog (Hh) signaling pathway. The Hh signaling pathway is conserved amongst vertebrates and plays a crucial role in embryonal development, adult stem cell homeostasis, and cancer (Armas-López et al., 2017; Jing et al., 2023).

In the absence of Hh ligands, the pathway remains inactive: The constitutively active, orphan receptor GPR161 resides in the cilium, stimulating transmembrane adenylate cyclases (ACs), which leads to an increase of the intraciliary cAMP concentration (Fig. 2) (Mukhopadhyay et al., 2013). GPR161 also functions as an A-kinase anchoring protein (AKAP) for the protein kinase A (PKA) regulatory subunit I α (PKA-RIα), thereby promoting ciliary PKA activity (Fig. 2). As a result, the catalytic subunit of PKA phosphorylates full-length glioma-associated transcription factors (GLI-FL) 2 and 3, which stimulates proteolysis into their repressor from (GLI-R). The GLI-R translocate to the nucleus and repress Hh-dependent gene expression (Fig. 2). The 12-transmembrane receptor Patched1 (PTCH1) also resides in the ciliary membrane under basal conditions. PTCH1 blocks Smoothened (SMO) activation and induces SMO ubiquitylation and removal from the cilium (Rohatgi et al., 2007).

Indian HH (IHH), Desert HH (DHH), and Sonic HH (SHH) are Hh ligands that bind to PTCH1. Ligand binding inhibits PTCH1, causing it to leave the cilium. This enables SMO to enter the cilium, where it is activated by its sterol ligands (Fig. 2) (Deshpande et al., 2019). SMO has been proposed to be a $G_{\alpha i}$-coupled GPCR, inhibiting ACs, whereby ciliary cAMP levels decrease. Moreover, SMO also directly inhibits PKA activity. Consequently, GLI phosphorylation is inhibited, and the proteins accumulate at the ciliary tip. Here, the GLI proteins are converted into their activator forms and can translocate to the nucleus to activate expression of Hh target genes (Fig. 2).

Notably, the controlled export of Hh receptors is facilitated by the BBSome and regulated via ubiquitination. For example, in the basal state, SMO is ubiquitinylated, which allows its

interaction with the BBSome for removal by retrograde IFT (Lv et al., 2021). Similarly, GPR161 and PTCH1 are ubiquitinylated once the pathway is activated to ensure their exit from the cilium (Ye et al., 2018).

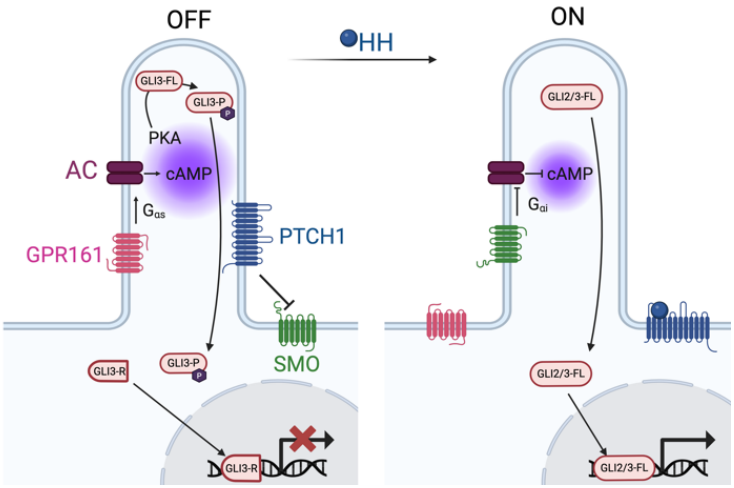

Fig. 2: Model of ciliary Hedgehog signaling. Left: Hedgehog signaling in a ligand-free state (OFF). Right: Hedgehog signaling in the presence of the ligand Sonic hedgehog (SHH) (ON). For further explanation, see text.

1.1.4 Ciliopathies

Primary cilia dysfunction leads to the development of a variety of diseases, collectively termed ciliopathies (Hildebrandt et al., 2011). Ciliopathies are genetic disorders. So far, 180 ciliopathies have been identified, and many more genes are still under investigation (Reiter & Leroux, 2017). As cilia are present on almost every mammalian cell, ciliopathies affect all organs. Consequently, ciliopathies display pleiotropic phenotypes and include a wide range of symptoms, e.g., retinal degradation, polydactyly, liver and kidney dysfunction, and obesity (Bisgrove & Yost, 2006). Studying ciliopathies enables better understanding of the role of the primary cilium in health and disease.

1.2 The role of the primary cilium in stem cell maintenance

Nearly all stem cells possess a primary cilium, and ciliary signaling is crucial for both differentiation and maintenance of stem cells throughout the mammalian life cycle (Shimada & Kato, 2022). During early embryonic development, the role of ciliary signaling has been extensively studied in the context of neural tube development and patterning. The time- and concentration-dependent activation of the Hh signaling pathway by a gradient of SHH is essential for the specification of distinct cell fates within the ventral

neural tube (Chiang et al., 1996; Yamada et al., 1993). Mutations in ciliary genes have profound effects on neural tube patterning and result in neural tube defects, such as spina bifida or anencephaly (L. Yan & Zheng, 2022). In radial glial cells, a population of neural stem cells residing in the cerebral cortex during development, ciliary function is linked to cell cycle regulation. Radial glia cells undergo either symmetric division to self-renew and expand the progenitor pool or asymmetric division to generate neuronal or glial precursor cells (Bear & Caspary, 2024). Primary cilia have an important role in balancing these two fates, and loss of cilia on these cells leads to the development of an enlarged forebrain (Wilson et al., 2012).

Primary cilia are also essential for maintaining the stem-cell identity of mesenchymal stem/stromal cells (MSCs) in the bone marrow. MSCs possess significant regenerative potential and can differentiate into multiple lineages, including osteogenic, adipogenic, and chondrogenic lineages. MSC cilia have been implicated in mechano-transduction and oxygen sensing, both of which influence cell fate decisions (Brown et al., 2014; Johnson et al., 2021).

Tissue homeostasis relies on a hierarchical organization of adult stem cells, in which one subset preserves self-renewal capacity, while another subset commits to terminal differentiation to fulfill physiological functions. This principle is well demonstrated in adult muscle, where muscle stem cells (MuSC) remain quiescent and undifferentiated but re-enter the cell cycle upon muscle injury. While most MuSCs proliferate to regenerate damaged myofibers, a minor subset follows a distinct program to replenish the quiescent MuSC pool (Brun et al., 2022; Venugopal et al., 2020). Genetic ablation of primary cilia significantly reduces the self-renewal capacity of MuSCs, while activation of the Hh pathway enhances their regenerative potential (Palla et al., 2022). With aging or prolonged injury, functional muscle tissue is gradually replaced by fat and fibrotic scarring, as stem cells increasingly give rise to fibro-/adipogenic progenitors (FAPs). Intriguingly, genetic ablation of cilia in FAPs reverses this pathological phenotype and even promotes myofiber regeneration (Kopinke et al., 2017).

Thus, the primary cilium is critical in maintaining stem-cell fate across different developmental stages and tissues. However, the interpretation of ciliary signaling cues is highly dependent on the tissue and cellular context and between physiological and pathological conditions. The underlying molecular mechanisms remain enigmatic.

1.3 Adipocyte progenitor cells and the adipose tissue

The parenchymal function of the adipose tissue is to store free energy in the form of lipid droplets. In states of energy surplus, white adipose tissue (WAT) expands to store energy in form of lipids. Expansion through increased lipid uptake leads to an increase in adipocyte size (hypertrophy) and is associated with pathophysiological effects of obesity (Ghaben & Scherer, 2019; Vegiopoulos et al., 2017). In contrast, recruitment and differentiation of adipocyte progenitor cells (APCs) into adipocytes (hyperplasia) is associated with a metabolically healthy obese state (Sakers et al., 2022). Notably, only precursor cells transiently possess a primary cilium, whereas mature adipocytes lack cilia (Christodoulides et al., 2009; Marion et al., 2008a). The importance of precise ciliary signaling has been characterized in the WAT.

1.3.1 APC Function – Adipogenesis

APCs originate from MSCs in the bone marrow and migrate to the adipose tissue. Their differentiation occurs in a stepwise manner, driven by the sequential activation of transcription factors. Differentiation is induced by various factors, including insulin, glucocorticoids, and an increase in intracellular cAMP (Fig. 3 a) (Klemm et al., 2001).
The first differentiation phase is the commitment step, during which MSCs restrict their fate to the adipogenic lineage (Fig. 3 b). Subsequently, APCs expand via mitotic clonal expansion, followed by a phase of growth arrest, which precedes the accumulation of lipid droplets and the final differentiation into mature adipocytes (Fig. 3 b). An increase in intracellular cAMP concentration is crucial during the early stages of differentiation, as it promotes PKA activation. PKA, in turn, activates the cAMP responsive element-binding protein (CREB), which induces expression of CCAAT-enhancer-binding protein β (CEBPβ) (Fig. 3 a) (Petersen et al., 2008). Members of the CEBP-family are transiently expressed during adipocyte differentiation and direct the process by binding to adipocyte-specific promotors (Cao et al., 1991; Yeh et al., 1995). The glucocorticoid dexamethasone induces CEBPδ expression, which acts in concert with CEBPβ to stimulate peroxisome proliferator-activated receptor γ (PPARγ) transcription (Fig. 3) (Rosen det al., 2002; Wu et al., 1995).

Insulin promotes adipogenic differentiation by inducing transcription of sterol regulatory element-binding protein 1 (SREB1), which enhances glucose and fatty acid uptake, initiates lipid synthesis, and activates PPARγ transcription (Fig. 3 a) (Cignarelli et al., 2019; J. B. Kim et al., 1998). All adipogenic signaling pathways converge on the activation of PPARγ, the master regulator of adipogenesis (Barak et al., 1999; Rosen et al., 2002). No other factor has been identified that can induce adipogenesis in the absence of PPARγ (Gurnell et al., 2003; Rosen & MacDougald, 2006). Together with CEBPα, PPARγ drives the expression of adipocyte-specific genes, including those encoding Fatty-acid acid binding protein 4 (FABP4), Perilipin, and the secreted factors adiponectin and leptin (Lefterova et al., 2008; Nielsen et al., 2008).

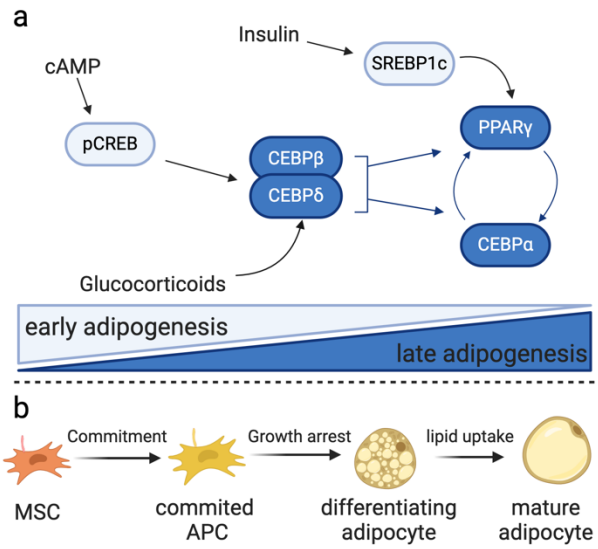

Fig. 3: Adipogenesis. a. Sequential activation of transcription factors during different phases of adipogenesis. b. Stages of precursor cells undergoing adipogenic differentiation to become mature adipocytes. For further explanation, see text.

1.3.2 APC Fate – Subpopulations

APCs have been extensively characterized on the single-cell level, revealing their heterogenic nature (Burl et al., 2018; Cho et al., 2019; Merrick et al., 2019; Nahmgoong et al., 2022; Schwalie et al., 2018; Shao et al., 2021; Spallanzani et al., 2019; H. Wang et al., 2024). Although a consistent definition of APCs is lacking, they are commonly identified by the absence of Lin markers (Lin: TER119, CD45, and CD31, markers for erythrocytes, immune- and endothelial cells, respectively), and enrichment for CD29 (Integrin b1) and SCA1 (stem-cell antigen) (Ferrero et al., 2020; Rodeheffer et al., 2008). Despite the heterogeneity of APCs, which varies with age, sex, and adipose tissue depot, different subpopulations exist along a differentiation spectrum, ranging from a more stem cell-like state to a high commitment to the adipocyte lineage (Ferrero et al., 2020). The

stem cell-like APC subpopulations express higher levels of stem-related genes, such as *Ly6a, Dpp4,* and *Cd55*, while lacking adipocyte-specific genes, such as *Fabp4* or *Pparg* (Merrick et al., 2019; Saygin et al., 2017). These cells also exhibit high proliferative capacity *in vitro* and have multilineage potential, as they still can differentiate into osteoblasts (Merrick et al., 2019). The stem cell-like APCs can undergo adipogenesis *in vitro*; however, only upon treatment with a complete induction cocktail (containing insulin, dexamethasone, and IBMX), indicating that they require specific cues to fully commit to the adipocyte lineage (Merrick et al., 2019; Schwalie et al., 2018).

In contrast, committed APCs readily differentiate into adipocytes with insulin alone (Merrick et al., 2019; Schwalie et al., 2018). These cells are less proliferative and express high levels of adipocyte-specific genes, such as *Fabp4*, *Pparg*, and *Perilipin* ((Burl et al., 2018; Merrick et al., 2019; Schwalie et al., 2018; Yang Loureiro et al., 2023). *In situ* trajectory studies and transplantation studies have established a lineage hierarchy, where stem cell-like ASCs give rise to committed APCs (Schwalie et al., 2018).

Beyond this differentiation trajectory, single-cell transcriptomics have identified other APC subpopulations with distinct functions. A subset of APCs was shown to be refractory to adipogenesis *in vitro*, and to actively suppress adipogenic differentiation of other APCs both *in vitro* and *in vivo* (Schwalie et al., 2018). This population, termed Aregs, expandes in obese mice and inhibits adipogenesis via paracrine secretion of R-spondin 2 (RSPO2) (Dong et al., 2022). Another APC subpopulation, which increased during obesity, exhibits a fibrogenic and immunogenic gene signature (Hepler et al., 2018; Joffin et al., 2021; Shao et al., 2021). These fibro-inflammatory progenitors (FIP) also exert an anti-adipogenic effects and activate a pro-inflammatory cytokine signature upon high-fat diet (HFD) feeding of mice (Shao et al., 2021).

Factors such as diet and age significantly influence APC subpopulation abundance. The increase in fibrogenic APCs that are refractive to adipogenesis happens on the expense of the stem cell-like APCs (Cho et al., 2019; Dong et al., 2022; Shao et al., 2021). Moreover, obesity also impairs the adipogenic potential of committed APCs, as they exhibit reduced differentiation capacity when isolated from obese mice (Merrick et al., 2019).

The rapid advancement of single-cell transcriptomics has reshaped our understanding of the highly heterogenic nature of APCs. However, the molecular mechanisms governing

APC fate determination remain elusive. Investigating ciliary signaling in APCs will provide novel insights, as the cilium plays a unique role in shaping stem cell behavior.

1.3.3 Ciliary control of APCs in the white adipose tissue

The presence of the cilium is crucial for adipogenic differentiation, as shown by several studies and data from our lab (Hilgendorf et al., 2019; Zhu et al., 2009). Notably, APC cilia mediate both anti- and pro-adipogenic signaling pathways. Activation of the Hh signaling pathway has a conserved role in inhibiting adipogenesis *in vivo* (Suh et al., 2006) and preventing adipogenic differentiation *in vitro* (Fontaine et al., 2008; Spinella-Jaegle et al., 2001). Interestingly, the APC differentiation state influences its response to Hh pathway activation. Hh stimulation of APCs in an early, stem cell-like state, inhibits adipogenic differentiation and promotes commitment to the osteogenic lineage (James et al., 2010). In contrast, committed APCs are less responsive to the anti-adipogenic effects and still undergo differentiation (Forcioli-Conti et al., 2015). Another ciliary pathway, Wingless-Int1 (Wnt) signaling, represses *Pparg* expression, maintaining APCs in an undifferentiated state (Okamura et al., 2009). Additionally, the melanin-concentrating hormone receptor 1 (MCHR1), known for its role in hypothalamic neurons, also localizes to cilia of the immortalized 3T3-L1 pre-adipocyte cell line, where its activation inhibits adipogenesis (Cook et al., 2021). However, while these pathways suppress differentiation, genetic ablation of cilia also inhibits adipogenesis, showing that cilia must also play a role in activating this process.

Indeed, insulin signaling in APCs may also be regulated by the primary cilium, as insulin growth factor 1 receptor (IGF-1R) localizes to the ciliary membrane (Zhu et al., 2009). Although IGF1R is also found in the plasma membrane, ciliary IGF1R is more sensitive and rapidly responds to low dosages of insulin (Zhu et al., 2009). Another pro-adipogenic ciliary receptor in APCs is the free fatty-acid receptor 4 (FFAR4), which increases ciliary cAMP levels upon activation, promoting of adipogenic genes expression (Hilgendorf et al., 2019).

The integration of these diverse and, at times, opposing signaling cascades suggests that the ciliary molecular composition must dynamically adapt to the cellular state. Precise regulation of receptor localization enables APC cilia to sense and appropriately respond

to extracellular signals. Effective trafficking and recruitment of ciliary cargo are therefore essential processes for proper signaling.

1.4 The Bardet-Biedl Syndrome

The Bardet-Biedl syndrome (BBS) is a rare, autosomal-recessive ciliopathy caused by mutations in any of the 26 genes encoding for the BBSome or the chaperonin complex (Forsyth and Gunay-Aygun, 2023). Its prevalence ranges from 1 in 100,000 in North America and Europe to 1 in 13,500-17,500 in isolated minorities, such as Kuwaiti Bedouins or Newfoundland (Farag & Teebi, 1989; Hjortshøj et al., 2008; D. Klein & Ammann, 1969). The phenotype is complex and affects multiple organs. Diagnosis requires four of six primary features (rod-cone dystrophy, obesity, polydactyly, hypogonadism, renal defects, and learning defects/cognitive impairment) or three primary features and two secondary features (anosmia, congenital heart disease, dental abnormalities or developmental delays) (Forsythe & Beales, 2013).

The genes that are causative to BBS can be divided in functional classes: (1) genes encoding for the subunits of the octameric BBSome (*BBS1, 2, 4, 5, 7, 8, 9, 18*), (2) genes encoding for the chaperonin complex that is supposed to stabilize complex-formation (BBS6, 10, 12), (3) *BBS3*/*ARL6* encoding for a GTPase that cooperates with the BBSome, or (4) non-canonical BBS genes (Forsythe & Beales, 2013; Niederlova et al., 2019; Novas et al., 2015). BBS mutations do not impair ciliogenesis or the ciliary structure *per se*, but disrupt ciliary protein composition by impairing the ciliary export machinery, particularly for GPCRs (Wachten & Mick, 2021). The mechanisms of linking BBSome dysfunction to organ-specific pathologies are only partially understood.

BBS-associated obesity results from excessive energy intake due to hyperphagia, highlighting the role for primary cilia in regulation of food intake. Ciliated neurons in the hypothalamus regulate hunger and satiety through melanocortin-4 receptor (MC4R) signaling. MC4R localizes to cilia and is activated by α-melanocyte-stimulating hormone (α-MSH) secreted from pro-opiomelanocortin (POMC)-expressing neurons. Activated MC4R couples to $G\alpha_s$ and increases ciliary cAMP levels, which inhibits feeding behavior. Conversely, inhibition of MC4R by Agouti-related peptide (AgRP)-, and neuropeptide Y (NPY)-expressing neurons promotes feeding behavior. In BBS, mislocalization of MC4R

signaling leads to an increased hunger feeling (Ayers et al., 2018). Additionally, BBS proteins regulate ciliary trafficking of the leptin receptor in POMC-neurons and, impaired leptin signaling contributes to hyperphagia (Guo et al., 2019; Seo et al., 2009).
However, ciliary dysfunction in BBS extends beyond the central nervous system. In mouse models mimicking BBS, normalizing the food intake to *wild-type* littermates still results in increased fat mass (Marion et al., 2012; Rahmouni et al., 2008). Mislocalized ciliary receptors in APCs may disrupt environmental sensing, affecting their fate and function. However, the exact molecular changes of ciliary signaling in driving WAT expansion in BBS are still not clear.

1.5 Hypothesis and research aims

I hypothesize that signaling via the primary cilium is required for APCs to sense external stimuli and respond to changes in the environment, and, thereby, governs fate and function of these cells. In my doctoral thesis, I aim to comprehensively investigate the APC subpopulations in WAT under physiological conditions and during primary cilia dysfunction in a BBS mouse model before the onset of obesity. Furthermore, I aim to investigate the role of the Hh pathway in APCs in governing cell fate and, whether this is disrupted in BBS.

2. Material and Methods

2.1 Material

2.1.1 Chemicals and reagents

Chemicals in *pro analysis* quality, kits, and other reagents were purchased from AppliChem (Darmstadt, Germany), BioLegend (San Diego, USA) BioRad (Munich, Germany), Eppendorf (Hamburg, Germany), Invitrogen (Karlsruhe, Germany), Merck (Darmstadt, Germany), Miltenyi Biotec (Bergisch Gladbach, Germany), Promega (Madison, USA), Quiagen (Hilden, Germany), Roth (Karlsruhe, Germany), Sigma (Steinheim), Roche (Basel, Switzerland), R&D Systems (Minneapolis, USA), and Thermo Fisher Scientific (Waltham, USA).

All buffers and solutions were prepared using double-distilled water (ddH2O). Autoclaving for sterilization was performed at 121°C for 20 min, if necessary. Sterile filtering of buffers was achieved using 0.45 µm or 0.22 µm pore filter membranes (Millipore) in vacuum filtration.

Phosphate buffered saline (PBS) was prepared in a 10-fold stock with 1.3 M NaCl, 70 mM Na_2HPO_4, 30 mM NaH_2PO^4, and adjusted to pH 7.4 at RT using 1 M NaOH. For usage, the 10-fold PBS stock was diluted to a 1-fold concentration in H2O. Sterile PBS that was used for cell culture was purchased from Gibco (DPBS).

2.1.2 Antibodies

Table 1: List of primary antibodies for immunocytochemistry.

Antigen	Species	Dilution	Supplier	Cat. Number
ARL13B	Mouse	1:1,000	Abcam	ab136648
ARL13B	Rabbit	1:150	Proteintech	17711-1-AP
CD9	Rat	1:200	Thermo Fisher	12-0091-81
FABP4	Goat	1:400	R&D Systems	AF1443
FIBRONECTIN (FBN)	Rabbit	1:500	Sigma	F3648
GLI1	Goat	1:2,000	R&D Systems	AF3455-SP
GLI3	Goat	1:500	R&D Systems	AF3690-SP

GPR161	Rabbit	1:200	Mukhopadhyay Lab	-
HA-tag	Rat	1:1,000	Roche	11 867 423 001
Ki-67	Rat	1:500	Invitrogen	14-5698-82
PDGFRA	Goat	1:500	R&D Systems	AF1062-SP
PERILIPIN (PLIN1)	Goat	1:400	Abcam	Ab61682
SHH	Rabbit	1:2,000	Santa Cruz	SC-9024
SMO	Rabbit	1:500	Anderson Lab	-
TUBULIN, β	Mouse	1:5,000	Sigma	T4026
TUBULIN, γ	Mouse	1:1,000	Sigma	T6793

Table 2: List of secondary antibodies.

Antigen	Fluorophore	Species	Dilution	Supplier	Cat. Number
Goat IgG	Cy3	Donkey	1:1,000	Dianova	705-165-147
Goat IgG (H+L)	Alexa Fluor 594	Donkey	1:1000	Abcam	ab150136
Goat IgG (H+L)	IRDye® 800RD	Donkey	1:5,000	LICORBio	926-32214
mouse IgG1 (y1)	Alexa Fluor 488	Goat	1:1,000	Thermo Fischer	A-21121
mouse IgG2a (y2a)	Alexa Fluor 647	Goat	1:1,000	Thermo Fischer	A-21241
Mouse IgG	Cy3	Donkey	1:500	Dianova	715-165-151
Mouse IgG (H+L)	IRDye® 680RD	Goat	1:20,000	LICORBio	926-68070
Rabbit IgG (H+L)	Alexa Fluor 488	Donkey	1:1000	Abcam	ab150065
Rabbit IgG	Alexa Fluor 488	Goat	1:500	Invitrogen	A11034
Rabbit IgG	Cy3	Goat	1:250	Dianova	711-165-152

Rabbit IgG	Alexa Fluor 647	Donkey	1:150	Dianova	712-605-153
Rat IgG	Alexa Fluor 647	Donkey	1:150	Dianova	712-605-153
Rat IgG (H+L), pre-absorbed	Alexa Fluor 555	Donkey	1:1000	Abcam	ab150155

Table 3: List of antibodies for flow cytometry and FACS.

Antigen	**Fluorophore/ Conjugate**	**Clone**	**Dilution**	**Supplier**	**Cat. Number**
Streptavidin	BV785	-	1:200	Biolegend	405249
CD140a (PDGFRA)	BV421	APA5	1:400	Biolegend	135923
CD142	PE	1	1:400	SinoBiological	50413-R001
CD25	PE	PC61	1:200	Biolegend	102007
CD26 (DPP-4)	PE/Cy7	H194-112	1:400	Biolegend	137809
CD29	PerCP-efluor710	eBioHMb1-1 (HMb1-1)	1:100	eBioscience (Thermo)	46-0291
CD3	APC	17A2	1:200	Biolegend	100236
CD31	Biotin	MEC13.3	1:400	Biolegend	102503
CD31	BV785	390	1:800	Biolegend	102435
CD4	PerCP-Cy5.5	GK1.5	1:400	Biolegend	100434
CD44	APC-Cy7	IM7	1:200	Biolegend	103028
CD45	Biotin	30-F11	1:400	Biolegend	103103
CD45	AF700	I3/2.3	1:800	Biolegend	147716
CD45	BV711	30-F11	1:400	Biolegend	103147
CD54	APC-Fire 750	YN1/1.7.4	1:800	Biolegend	116125
CD55	APC	RIKO-3	1:800	Biolegend	122513
CD8a	BV510	53-6.7	1:200	Biolegend	100751

CD9	PerCP/Cy5.5	MZ3	1:400	Biolegend	124818
Foxp3	AF488	150D	1:50	Biolegend	320012
SCA1	BV510	D7	1:200	Biolegend	108129
TER119	Biotin	TER-119	1:400	Biolegend	116203
TER119	AF700	TER-119	1:800	Biolegend	116220

For CD142 antibody was conjugation with fluorophore was done with a kit following the manufacturers instruction. Kit: LYNX Rapid Conjugation Kit for PE (BioRad, LNK021RPE).

Table 4: List of antibodies used for MACS.

Antigen	**Conjugate**	**Dilution**	**Supplier**	**Catalog Number**
CD26 (DPP4)	Biotin	1:400	Biolegend	137809
CD31	Biotin	1:400	Biolegend	102503
CD45	Biotin	1:400	Biolegend	103103
CD45	Biotin	1:800	Biolegend	116103
TER-119	Biotin	1:400	Biolegend	116203
VAP-1	Biotin	1:800	abcam	ab81673

The anti-VAP1 antibody, the concentration of the antibody was too low, so it was concentrated via centrifugal filters (Amicon® Ultra) before conjugation. Conjugation kit: Lightning-Link® for Biotin (Abcam, ab201796),

2.1.3 Plasmids and primers

Table 5: Plasmid information.

Name	**Internal identifier**	**Vector backbone**	**Expresses**	**Reference / produced by**
pcDNA3.1-Shh-N	DW-0497	pcDNA3.1 (+)	*ShhN*	Addgene #37680
hCMV-mTtc8--3 x HA-hPGK-Blasticidin	2865	hCMV	*Ttc8 (Bbs8)*	Rainer Stahl

Table 6: RT-qPCR primer information.

PCR	Forward primer sequence	Reverse primer sequence
Col1a1	GAGATGATGGGGAAGCTGGC	CTCGGTGTCCCTTCATTCCG
Col5a1	CTTGTCCGATGGCAAGTGGC	CATCATCCAGAATCCGGGAGC
Col6a1	CAGGTACTACCGGTGTGACC	GAAGTACTTGACCGCATCCAC
Fibronectin	CTCCGAGACCAGTGCATCG	GAATCTTGGCACTGGTCAATGG
Loxl2	CTGCCTGGAGGACACTGAGT	CTGCCTGGAGGACACTGAGT
Sparc	CGGTGATGTCTATCCACTGGC	CGGTGATGTCTATCCACTGGC
TnC	CCACACTCACAGGTCTAAGGC	GATGGTTGCTGGATCACTCTCC
Gli1	TACCATGAGCCCTTCTTTAGGA	GCATCATTGAACCCCGAGTAG
Ptch1	GCCTTGGCTGTGGGATTAAAG	CTTCTCCTATCTTCTGACGGGT
Gapdh	AGGTCGGTGTGAACGGATTTG	TGTAGACCATGTAGTTGAGGTCA
Tatabp	GAGCTCTGGAATTGTACCGCAG	CATGATGACTGCAGCAAATCGC

2.1.4 Instruments

Table 7: List of instruments.

Product	Company	Project Number DFG
4D-Nucleofector® X- and Core Unit	Lonza Bioscience	-
Attune NxT Flow Cytometer	Thermo Fischer	-
BD FACSAria III	BD Biosciences	216372545
ID7000 Spectral Cell Analyzer 5L	Sony Biotechnology	471514137
Leica SP8 AOTF	Leica	266686698
Leica Stellaris 8	Leica	01EO2107
PCR cycler	SensoQuest	-
QuantStudioTM 6 Pro Real-Time PCR	Thermo Fischer	
Vi-CELL BLU	Beckmann Coulter	-
Zeiss AXIO SCAN.Z1	Zeiss	388168919
Zeiss CELLDISCOVERER 7	Zeiss	388158066

2.2 Mice

2.2.1 Licenses

All animal experiments were performed in agreement with the German law of animal protection and local institutional animal care committees (Landesamt für Natur, Umwelt und Verbraucherschutz, LANUV). Mice were kept in individually ventilated cages in the mouse facility of University Hospital Bonn (Haus für Experimentelle Therapie [HET] and Immunological Facility of Experimental Therapy [iFET], Universitätsklinikum, Bonn). Mice were raised under a normal circadian light/dark cycle (each 12 h) and animals were given water and complete diet (ssniff Spezialdiäten) ad libitum (LANUV Az 81-02.04.2019.A170). Mice were sacrificed by cervical dislocation. Genotyping of mice was based on isolation of genomic deyoxyribonucleic acid (DNA) from tail tips or ear clips and performance of a polymerase chain reaction (PCR).

2.2.2 Mouse lines

2.2.2.1 *Bbs8*$^{-/-}$ line

Bbs8$^{-/-}$ mice were generated in the laboratory of Prof. Rendall R. Reed and kindly provided by Prof. Helen May Simera (Johannes-Gutenberg-Universität, Mainz). To generate the knockout, the start codon and the first two exons of the *Bbs8* gene were deleted, and a tau:YFP reporter was inserted at the start codon (Tadenev et al., 2011).

2.2.2.2 *Bbs8*$^{-(KOMP)/(KOMP)-}$ line

C57BL/6N-Ttc8tm1a(KOMP)Wtsi/MbpMmucd mice were purchased from MMRRC (Mutant Mouse Resource & Research Centers supported by NIH). Animals were generated by inserting a LacZ reporter/neomycin resistance cassette between exon 2 and 3 of the Bbs8 gene, effectively blocking all transcription (Dilan et al., 2018).

2.2.2.3 *Pdgfra*-Cre line

C57BL/6-Tg(Pdgfra-cre)1Clc/J (Pdgfra-Cre, Stock No.: 013148) mice were purchased from the Jackson Laboratory. The cre recombinase is expressed under the control of the *Platelet derived growth factor receptor α* (*Pdgfra*) promotor, which can be used to breed conditional knockout mouse lines.

2.2.2.4 *Pdgfra*^{Cre}-Bbs8$^{flox/flox}$ line

The conditional knockout mouse line was generated based on the *Bbs8*$^{-(KOMP)/(KOMP)-}$ mouse line. Mice were first crossed to Flp-deleter mice (Rodríguez et al., 2000) to generate *Bbs8*$^{flox/flox}$ mice, which were crossed to the Pdgfra-Cre mouse line to create a conditional knockout.

2.3 Maintenance of cell lines

Cells were grown in their respective growth medium (Table 8) on 10 cm plastic dishes at 37°C with 5% CO_2 and passaged every 3-4 days at around 70% confluency using the following protocol: Cells were washed once with Dulbecco's phosphate buffered saline (PBS, Gibco/ Life Technologies) and incubated with 0.05 % Trypsin-Ethylenediaminetetraacetic acid (Trypsin-EDTA, Gibco/Life Technologies) at 37°C until they detached. The reaction was stopped by the addition of 9 mL growth medium and resuspension of the cells. Then, cells were resuspended in medium and counted using a Neubauer counting chamber (LO-Laboroptik Ltd). The required cell number was seeded into a new cell culture dish (10 cm, Greiner Bio-One), containing medium. Cells older than passage 15 were discarded. Cells were tested for mycoplasma twice a year and were free from mycoplasma.

Table 8: Cell line-specific information.

Cell line	Origin	Growth Medium
3T3-L1	Kindly gifted from Prof. Christoph Thiele	DMEM + 1 % GlutaMAX™-I + 10% FCS
HEK293T	ATCC (CRL-3216)	DMEM + 1 % GlutaMAX™-I + 10% FCS
Mouse embryonic fibroblasts (MEF)	Dr. Christina Klausen	DMEM + 1 % GlutaMAX™-I + 10 % FCS + 1 % Pen/Strep

For long-term storage and resetting of the passage number, cells were cryopreserved. Cells were detached from the plate and pelleted by centrifugation at 500 x g for 5 min at room temperature (RT). The cell pellet was resuspended in 1 mL growth medium

containing 10 % Dimethylsulfoxide (DMSO, Sigma) and transferred into a cryotube. The cryotube was placed at -80°C inside a freezing container. For long-term storage, cells were transferred into a -150°C freezer. Re-culturing of cryopreserved cell was done by gently thawing the vial at 37°C. Subsquently, cells were mixed with 10 mL of pre-warmed growth medium. Then, the cells were pelleted at 500 x g for 5 min at RT. Subsequently, the cell pellet was resuspended in 10 mL growth medium and distributed equally on 10 cm plastic dishes and cells were maintained at 37°C with 5% CO_2.

2.4 Isolation of primary cells

2.4.1 Primary cell medium

Table 9: Primary cell-specific information.

Cell type	Growth Medium
Primary SVF	DMEM/Ham's F-12 (1:1) + 1 % GlutaMAX™-I + 10 % FCS + 1 % Pen/Strep + 0.1 % Biotin (33 µM) + 0.1 % D-Pantothenic acid (17 µM)
Primary TEC	DMEM/Ham's F-12 (1:1) + 1 % GlutaMAX™-I + 10 % FCS + 1 % Pen/Strep
Thymus organ	DMEM + 10 % FCS + 1 % Pen/Strep + 1 % HEPES

2.4.2 Stromal vascular fraction isolation

Gonadal (g) or inguinal (i) WAT were surgically removed from mice and processed for stromal vascular fraction (SVF) isolation as follows. After removal, WAT was transferred into 2 mL tubes containing ice-cold WAT buffer (PBS + 0.5 % bovine serum albumin (BSA)) and minced into small pieces (approx. 2 mm). An enzyme solution (Table 10) was freshly prepared each time and tissues were digested for 30 min at 37°C with agitation. The digestion was quenched by adding WAT buffer and the dissociated cells were passed through a 100-µm filter (Corning) and subjected to centrifugation at 500 × g for 10 min.

The resulting supernatant containing mature adipocytes was aspirated, and the pellet, consisting of the stromal vascular fraction (SVF), was resuspended in red blood cell lysis buffer (BioLegend) for 2 min at RT. The reaction was stopped by adding WAT buffer and another round of centrifugation at 500 × g for 10 min. Isolated cells were then further subjected to antibody staining for sorting of cells.

Table 10: SVF isolation enzyme solution.

Volume (per tissue)	**PBS + 0.5 % BSA**	**Collagenase II (200 mg/mL)**	**Ca_2Cl (1 M)**	**DNase I (15,000 U/mL)**
3 mL	3 mL	30 µL	15 µL	15 µL

2.4.3 Isolation of thymic epithelial cells

Isolation of thymic epithelial cells (TEC) was done according to a protocol from Xing and Hogquist with some modifications (Xing & Hogquist, 2014). After removal, the thymus was transferred into a 6-well plate containing 2.5 mL freshly prepared enzyme solution and small incisions to the thymus lobe were done (Table 11). Following 20 min incubation at 37°C, the digested thymus tissue was pipetted up- and down several times and the supernatant was collected in a fresh tube containing 5 mL ice-cold WAT buffer. Another 2.5 mL of enzyme solution were added to the remaining thymus tissue and the plate was incubated again at 37°C for 15 min. Using a 2.5 mL syringe (B. Braun) with a 20 G needle, the tissue was further broken up and the supernatant was collected again. Following another round of 15 min of incubation with 2.5 mL of enzyme solution, the process was repeated with a 25 G needle and finally the remaining tissue was incubated for 10 min at 37°C again. All supernatant was collected in WAT buffer and the following centrifugation at 400 x g for 8 min at 4°C, the cell pellet was resuspending in 10 mL WAT buffer and filtered through a 100 µM cell strainer. Subsequently, removal of CD45+ cells was done using the EasySepTM CD45 depletion kit (STEMCELL technologies) according to the manufacturer's protocol. Briefly, $1x10^8$ cells were resuspended in 1.5 mL FACS buffer (PBS + 0.5 % BSA + 2 mmol/L EDTA)) and 75 µL FcBlock were added to each sample. The mix was transferred to a FACS tube and 15 µL of anti-CD45 (Biotin conjugated) were added to each sample and incubated for 10 min at RT. The RapidSpheres were vortexed for 30 sec before adding 180 µL of RapidSpheres to each sample. Following an incubation step of 2:30 min, the volume was topped up to 2.5 mL per sample, and the sample was

placed into the EasySep™ Magnet for approx. 3 min. Subsequently, the cell suspension was poured into a fresh tube and cells were counted. The cells were cultured in their respective medium at 37°C and 5 % CO_2.

Table 11: TEC enzyme solution.

Volume (per tissue)	RPMI1640	Liberase TH (2.5 mg/mL)	DNase I (15,000 U/mL)
10 mL	8 mL	2 mL	66 µL

2.5 Thymic organ culture

For thymic organ culture, mouse pups were sacrificed at postnatal day 0 (P0) by decapitation. The thymus was carefully dissected and placed into 24-well plate in WAT buffer. Then, the thymus was placed onto a 0.4 µm polycarbonate transwell insert (Corning® #3413) which was placed in a well containing thymus organ culture medium (Table 9), creating an air-liquid interface.

2.6 Flow cytometry

Pre-adipocyte subpopulations within the WAT or T cell populations of the thymus were analyzed and sorted by flow cytometry. SVF was isolated as described above. Thymocytes were isolated by removing the thymus from the insert, washing it one time with FACS buffer and subsequently meshing it through a 100 µm cell strainer. If the flow analysis was done on the next day, cells were stored in 1 mL MACS Cell Storage Solution (Miltenyi Biotec) at 4°C over night. Cells were resuspended in 50 µL FcBlock (anti-mouse CD16/32 (Biolegend) + 2 % rat serum (BioRad)) or FcBlock (Miltenyi Biotec) and incubated for 10 min, before FACS buffer was added to the desired volume. The cell suspension was transferred to a U- or a V-bottom 96-well plate. Cells were resuspended in 20 µL of antibody mix (Table 3) and incubated for 30 min on ice. Following another washing step cells were, incubated either with 100 µL of the secondary antibody or LIVE/DEAD™ Near IR (780) Viability Kit (1:1,000 in PBS) on ice for 15 min. After this, cells were washed, and the cells were resuspended in 100 µL of FACS buffer. After the immunostaining of the T cell antibody panel, the samples were fixed and permeabilized with eBioscience™ Foxp3/Transcription Factor Staining Buffer Set (ThermoFisher)

following the manufacturer's protocol and immunostained with FOXP3-AF488 (Biolegend). For flow cytometry measurements the sample was filtered with a cell strainer (70 µm diameter) right before acquisition. If cells were not stained with LIVE/DEAD™ Near IR (780) Viability Kit, live-dead staining was done by adding Hoechst (1:5,000, Thermo Fischer) or 7-AAD (1:100, Biolegend) to the cells. If needed, the cell suspension was further diluted with FACS buffer. Samples were analyzed on the AttuneTM Nxt, BD FACSAria III, or the ID700 Spectral Analyzer (Table 7).

2.7 Sorting of cells

2.7.1 Fluorescent-activated cell sorting

Pre-adipocyte subpopulations within the WAT were sorted by fluorescent-activated cell sorting (FACS) with the BD FACSAria III. SVF isolation and staining for flow cytometry was done as described above. If cells were sorted for culturing, isolation and staining were done under sterile conditions. Cells were sorted either in 1 mL SVF medium for further cultivation or in 1 mL of a monophasic solution of phenol and guanidine isothiocyanate reagent (TRI Reagent®, Sigma-Aldrich) for subsequent ribonucleic acid (RNA) isolation.

2.7.2 Magnetic-activated cell sorting

MACS was performed according to manufacturer's instructions (Miltenyi Biotec). Isolated SVF cells were incubated with biotinylated anti-CD45, anti-CD31, and anti-TER119 antibodies (Biolegend), followed by incubation with Streptavidin MicroBeads (Miltenyi Biotec). Alternatively, SVF cells were incubated with the non-adipocyte progenitor depletion cocktail of the Adipose Tissue Progenitor Isolation Kit (1:10; Miltenyi Biotec). Samples were run through LD columns (Miltenyi Biotec) followed by three washes with MACS buffer (= FACS buffer). Unlabeled cells were collected and either cultured (referred to as SVF Lin- cells) or further incubated with biotinylated anti-CD54, anti-VAP1, or anti-CD26 antibodies followed by incubation with Streptavidin MicroBeads. Cells were separated using MS columns (Miltenyi Biotec), and either the bead-bound fraction (positive selection) or the wash-through (negative selection) was collected and cultured.

2.8 *In-vitro* adipogenesis assay

For the adipogenesis assay, 3T3-L1 cells or isolated APCs were seeded on CellCarrier Ultra 96- or 384-well plates. When cells reached confluency, adipogenesis was induced by switching to their respective induction cocktail: a) Full Induction (FI) containing 5 µg/ml insulin (Sigma), 1 µM Dexamethasone, 100 µM 3-isobutyl-1-methylxanthine (IBMX; Sigma), and 1 µM rosiglitazone (Sigma) or b) Minimal Induction (MI) (Hilgendorf et al., 2019) containing 0.4 µg/ml insulin, 0.1 µM Dexamethasone, and 20 µM IBMX. TUG891 (Tocris) was added at a concentration of 100 µM and DMSO was used as a vehicle control. The medium was exchanged to freshly prepared maintenance medium, containing 1 µg/ml insulin on day 3 and 5. Additionally, as a negative control, undifferentiated cells without induction medium were kept in maintenance medium.

2.9 Pharmacological manipulation of the Hh signaling pathway

To induce Hh signaling, cells were then stimulated with either 100 nM or 1 µM Smoothend Agonist (SAG, Sigma) or H_2O (vehicle) for 24 h or 48 h. To inhibit SMO signaling, primary APCs were treated with 2 µM Vismodegib (LC Labs/V-4050) for 48 h. Subsequently, cells were harvested for analysis via flow cytometry, RNA isolation, or fixed for immunocytochemistry.

2.10 Production of ShhN

For alternative activation of the Hh pathway via the biologically active N-terminal ligand of SHH (ShhN), I produced ShhN in HEK293T cells using PEI transfection. Cells were seeded to 6-cm dishes one day prior to transfection to reach a confluency of 80 % on the day of transfection. HEK293T cells were transfected using PEI. Transfection mix was prepared according to Table 12 and incubated for 10 min at room temperature (RT). In the meantime, medium of HEK293T cells was replaced with 4 mL medium containing 2 % FCS. Subsequently, the transfection mix was added. Cells were incubated at 37°C with 5 % CO_2 for 48 h.

Table 12: PEI transfection mix.

Reagent	Added
DNA	4.5 µg

PEI stock (1 µg/µL)	10 µL
OptiMEM	470 µL

To harvest ShhN, the supernatant of transfected cells was transferred into 1.5 mL reaction tubes and cleared of cell debris by centrifugation with 20,000 x g for 10 min at 4°C. The ShhN supernatant was used for stimulation within 24 to 48 h post harvesting. Simultaneously, successful ShhN production was assessed by Dot Blot.

2.11 Transient gene expression using electroporation

For transient expression of *Bbs8* in MEFs, cells were used at a confluency of 78-80 %. 200,000 cells were spun down at 400 × g for 4 min at RT. Cells were resuspended in 20 µl of nucleofection master mix (Amaxa™ P4 Primary Cell 4D-Nucleofector™ X Kit) (Table 13). Cell suspension was transferred into separate wells in the Nucleostrip and electroporated in the 4D-Nucleofector X Unit (Lonza) with the pulse code CZ 167. After electroporation, the cell suspensions were incubated at RT for 10 min before the addition of 40 µl of pre-warmed media. The cell suspension was seeded at a density of 20,000 cells per well of a black PhenoPlate 96-well plate (Revvity) and incubated at 37 °C and 5 % CO_2 for 48 h before fixation for immunocytochemistry or stored for RNA isolation.

Table 13: Nucleofection mix.

Reagent	**Added**
DNA	1 µg
Supplement 1	7.2 µL
Nucleofector solution P4	32.8 µL

2.12 Pulse-Chase analysis of fatty acid incorporation

Pulse chase analysis using alkyne-labeled fatty acids followed the protocol described in (Wunderling et al., 2023). MACS-isolated P1 cells were seeded on 48-well plates and adipogenesis was induced by adding a full induction cocktail for three days and then switching to 1 µg/ml insulin for one more day. Subsequently, cells were fed with growth medium containing 50 µM of each alkyne-fatty acids (FA): FA 11:0;Y (TCI Deutschland GmbH), FA 18:2;Y (multistep synthesis done by Dr. Christoph Thiele) and $^{13}C_6$-FA 16:0;Y

(multistep synthesis done by Dr. Christoph Thiele), for 1 h. After 1h media were removed, cells were washed once with medium and fresh medium was added for the chase times 24 h, 8 h, 4 h, and 0 h. After the chase, media were removed, and cells were washed with PBS and processed for extraction and analysis.

Lipid extraction and click reaction were performed by Dr. Jelena Zurkovich in the Lab of AG Thiele and have been described in detail in Sieckmann *et al.,* 2024 (bioxRiv) (Sieckmann et al., 2024). Briefly, extraction mix, internal standards containing alkyne-labeled standard lipids and a non-alkyne internal standard for triglycerides (TG) were added to the plate and sonicated. The extract was centrifuged at 20,000 x g for 5 min to pellet protein. After addition of $CHCl_3$ and 1 % AcOH in water, samples were shaken and centrifuged at 20,000 x g for 5 min. The upper phase was removed, the lower phase transferred into a fresh tube and dried for 20 min at 45°C in a speed-vak. $CHCl_3$ was added, tubes were vortexed, and Click mix (100 mM C175-7x in 50 % MeOH with 5 mM Cu(I)$AcCN_4BF_4$ in AcCN and ethanol) was added, followed by sonication for 5 min and incubation at 40°C for 16 h. $CHCl_3$ was added per sample was added and samples pooled were pooled. Water was added and pools briefly shaken and centrifuged for 20,000 x g for 2 min. The upper phase was removed and the lower phase dried in a speed-vak. Spray buffer was added, the tubes sonicated, and the dissolved lipids analyzed by mass-spectrometry on am Thermo Q Exactive Plus spectrometer. Instrument parameters and data analysis procedure (Wunderling et al., 2023). Raw files were converted to .mzml files using MSconvert and analyzed using LipidXplorer for lipid species that incorporated the alkyne fatty acid.

2.13 Immunocytochemistry

Cells were fixed with 4 % paraformaldehyde (PFA, 16% wt/vol ag. Soln., methanol free, Alfa Aesa) for 10 min and subsequently washed with PBS before blocking with CT (0.5 % Triton X-100 (Sigma-Aldrich), 5 % ChemiBLOCKER (Merck Millipore) in 0.1 M NaP, pH 7.0) for 30 min at RT. Primary and secondary antibodies were diluted in CT and incubated for 60 min at RT. 4′,6-diamidino-2-phenylindole, dihydrochloride (DAPI, 1:10,000, Invitrogen) was used as a DNA counterstain together with the secondary antibody. For staining of lipid droplets, cells were incubated with the lipophilic dye LD540 (1:10,000) for 15 min and washed again with PBS. All antibodies are listed in Table 1 and Table 2.

2.14 Whole mount staining

Whole mount staining was performed by Luis Henrique Corrêa in the lab of Prof. Lydia Sorokin. Briefly, tissues were fixed with 4 % PFA for 2h at 4°C and subsequently washed with PBS. Tissues were then cut into small pieces (~2 x 2 mm) and placed into a 24-well plate. Blocking solution (1 % (w/v) BSA + 1 % (v/v) Triton X-100 in PBS) was added, and samples were incubated for 2 h at RT. Following fixation and blocking, primary antibodies were added. Antibodies were diluted in blocking solution, and tissues were incubated overnight at 4°C. After washing samples with PBS, secondary antibodies, diluted in DAPI solution, were added to each sample. Tissues were incubated overnight at 4°C, protected from light. Afterwards, samples were washed with PBS and mounted in Elvanol, covered with a glass cover slip, and stored at 4 °C until imaged. The mounting medium was prepared by dissolving Mowiol® 4-88 (Merck) in PBS to prepare a 25 %(w/v) solution and stirred continuously at RT overnight. Then the solution was heated to 50°C and stirred for an additional 2–3 hours. Afterward, 50 ml of glycerol was added, and the mixture was stirred at RT overnight. The solution was then centrifuged at 12,000 × g for 30 min at 4°C, and the supernatant was carefully transferred to a fresh tube. Next, 30 mg of p-phenylenediamine were gradually introduced at 4°C while stirring continuously. Following this step, 1 M NaOH was slowly added dropwise to adjust the pH to 8.0. From this point forward, the solution was kept protected from light. To achieve the desired color transition, β-mercaptoethanol was added gradually until the solution shifted from brown to light yellow. Finally, the Elvanol solution was aliquoted and stored at -20°C for later use.

2.15 Histological staining

Histological analysis was performed as previously described (Sieckmann et al., 2022). Briefly, WAT was fixed and further processed using the automated Epredia Excelsior AS Tissue Processor (ThermoFisher Scientific). Tissues were dehydrated, cleared in a clearing agent and xylene (AppliChem) before incubating in molten paraffin wax (Labomedic). Tissues were cast into molds together with liquid paraffin and cooled to form a solid paraffin block with embedded tissue (Leica EG1150 H Paraffin Embedding Station and Leica EG1150 C Cold Plate). Paraffin-embedded WAT was sliced into 5-µm sections using a ThermoScientific HM 355S Automatic Microtome and mounted on Surgipath X-tra Microscope Slides (Leica Biosystems).

For histological analysis WAT sections were stained with Hematoxylin and Eosin (H&E) using the Leica ST5020 Multistainer combined with Leica CV5030 Fully Automated Glass Coverslipper. Deparaffinization of paraffin-embedded WAT slices was performed and three subsequent steps in xylene before incubation in a graded alcohol series (100–70 % ethanol) to rehydrate the tissue sections and ending with a final rinsing step in sterile distilled water (dH2O). Next, tissue slices were stained with Mayer′s hemalum solution (Sigma Aldrich). To counterstain with Eosin Y solution (1 % in water, Roth), slides were immersed in eosin. Afterwards, slides were incubated in a graded alcohol series (70–100 % ethanol) to dehydrate the tissue. Paraffin embedding, slicing, and staining were conducted by the histology facility at University Hospital Bonn.

2.16 Microscopy and image analysis

Confocal z-stacks were recorded with a confocal microscope at the Microscopy Core Facility of the Medical Faculty at the University of Bonn (Leica SP8. Leica Stellaris, Zeiss CellDiscoverer7). The whole mount imaging was performed by Luis Henrique Corrêa in the lab of Prof. Lydia Sorokin using Zeiss laser scanning confocal microscopes (LSM 900), and images were captured using Zen Blue 3.0 or 3.1 software from Zeiss.

For quantifying fluorescence signals, z-stacks were recorded from at least two random positions per experiment and analyzed using “CiliaQ” (Hansen et al., 2021). CiliaQ was developed to fully automatically quantify the ciliary intensity levels in the different channels. Whole mount images were generated using Z-projections (spanning 50–150 µm across optical planes.

Fluorescence images of adipogenesis assays were taken using automated image acquisition. Depicted images are shown as a projection of the sharpest plane including the plane above and below. A maximum projection around the sharpest plane was generated using the ImageJ plugin ExtractSharpestPlane_JNH (https://doi.org/10.5281/zenodo.5646492) (Hansen et al., 2021).

Histological sections were imaged with the Zeiss Axio Scan.Z1 Slide Scanner.

Adipogenesis and adipocyte morphology was quantified using “AdipoQ” (Sieckmann et al., 2022). Briefly, custom preferences for AdipoQ Preparator and AdipoQ were used to identify and analyze adipocytes.

2.17 Protein Biochemistry

2.17.1 Preparation of protein lysates and determination of protein concentrations

All steps were performed on ice in the presence of mPIC (Sigma). Cells were washed once with PBS and scraped in 1 mL PBS and subsequently transferred into a 1.5 µL reaction tube. Cells were pelleted by centrifugation at 500 x g for 5 min at 4°C. The pellet was resuspended in lysis buffer (in mM: 10 Tris/HCl pH 7.6, 140 NaCl, 1 EDTA, 1 % (v/v) TritonX-100, 1:500 mPIC) and incubated for 30 min on ice. Following centrifugation at 10,000 x g for 10 min, the supernatant was used in further steps.

Protein concentration was determined with the Pierce® bicinchoninic acid Protein Assay Kit (Thermo Scientific) according to the manufacturer's instruction. For every experiment, the assay was calibrated using the protein standard included in the kit. Absorption at 570 nm was measured in a plate reader (FluoStar; BMG Labtech). Linear regression of the BSA standard allowed to calculate the protein concentrations.

2.17.2 Sodium dodecyl sulphate-polyacrylamide gel electrophoresis (SDS-PAGE)

Denaturing sodium dodecyl sulfate polyacrylamide gel electrophoresis (SDS-PAGE) was performed to separate proteins according to Laemmli (Laemmli, 1970). Discontinuous gels were casted with a 10 % separation gel (1.5 mL Tris-HCl (pH 8.8), 60 µL 10 % (w/v) SDS, 40 µL (w/v) APS, 6 µL TEMED, 2 mL 30 % (v/v) acrylamide/bis-acrylamide (37.5:1) solution, and 2.42 mL H_2O), and a 5 % stacking gel (0.5 mL Tris-HCl (pH 6.8), 20 µL 10 % (w/v) SDS, 40 µL (w/v) APS, 6 µL TEMED, 340 µL 30% (v/v) acrylamide/bis-acrylamide (37.5:1) solution, and 1.12 mL H_2O). Alternatively, NuPAGE™ 4-12 % Bis-Tris Gels (Invitrogen) were used. Protein samples were prepared in SDS sample buffer and boiled for 5 min at 95°C. Electrophoretic separation was performed in SDS running buffer using the Mini-PROTEAN Tetra Cell system at 15-25 mA until the 25 kDa band of the Protein Marker VI (AppliChem) reached the bottom of the gel. Proteins that were separated using SDS-PAGE were subjected to Western Blot analysis.

2.17.3 Western Blot analysis and immunostaining of immobilized proteins

Proteins were blotted from the SDS-PAGE gel onto the PVDF membrane using discontinuous semi-dry Western blotting in the Semi-dry-blotter as follows: two filter papers, soaked in Western Blot Anode buffer 1, were placed on the anode, followed by

one filter paper soaked in Anode buffer 2 above, followed by the methanol-activated PVDF membrane above, followed by H_2O-rinsed SDS- PAGE gel above, followed by three filter papers soaked in Cathode buffer above, followed by the cathode above. The PVDF membrane and filter papers were cut to fit on the SDS-PAGE gels. Proteins were blotted for 50 min at 2.4 mA per cm^2.

SDS-PAGE separated proteins in precast gels were transferred to methanol-activated PVDF membrane by wet transfer. Wet transfer was performed in a blotting chamber with ice-cold transfer buffer (48 mM Tris-base, 39 mM glycine, 0.037 % SDS and 20 % methanol) for 2 h at 120 mA per membrane.

After blotting, the PVDF membrane was briefly placed in methanol and washed with PBS. Western blot analysis was performed by immunostaining of proteins. To this end, the PVDF membrane was incubated for 30 min at RT in blocking buffer (Odessey Intercept PBS), followed by incubation with the primary antibody overnight at 4°C (Table 1). The membrane was washed three times for 20 min in PBS-T at RT. Subsequently, the membrane was incubated with the secondary antibody (Table 2) for 1 h at RT and, subsequently, washed three times for 20 min in PBS-T at RT. After the final washing step, the membrane was imaged at the Odyssey Imaging System (LI-COR Biosciences).

2.17.4 Dot Blot analysis

To verify presence of SHH in the supernatant of *pcDNA3.1-Shh-N* transfected HEK293T cells, Dot Blot analysis was performed. Therefore, 10 µL of the supernatant were pipetted on a methanol-activated PVDF membrane and dried for approx.10 min at RT. The membrane was re-activated in methanol and immunostaining was performed as described above.

2.18 Gene expression analysis

2.18.1 RNA isolation and cDNA synthesis

To isolate total RNA from cells, the PureLink® RNA Mini or Micro kit (Thermo Fisher Scientific) was used according to the manufacturer's instructions. To avoid any RNase activity, RNase-free water and RNase-free reaction tubes were used. Additionally, all equipment used was wiped with RNase ZAP (Merck). Total RNA was extracted by adding lysis buffer containing 1 % β-mercaptoethanol to cells. The lysis buffer contained

guanidinium isothiocyanate, a chaotropic salt capable of protecting the RNA from endogenous RNases (Chirgwin et al., 1979). Lysates were scraped from the wells into microcentrifuge tubes and homogenized by vortexing.

To cells that were lysed within TRI Reagent®, chloroform was added and incubated for 2-3 min. Samples were centrifuged at 12,000 x g for 15 min at 4°C to separate different phases. The colorless, upper phase, containing the RNA, was transferred to a fresh tube. An equal amount of 70 % ethanol was added, and samples were vortexed. Samples were processed via silica-based RNA spin column enrichment and eluted in 30 µl RNase-Free water and directly put on ice. The RNA concentration and purity was measured using a spectrophotometer (Nanodrop, NanoDrop Products).

For complementary DNA (cDNA) synthesis, the iScript TM cDNA synthesis Kit (Biorad) was used according to the manufacturer's instructions. Via reverse transcription, cDNA was synthesized from an RNA template. Synthesis was performed in a Thermocycler (Labcycler, SensoQuest). cDNA was subsequently stored at -20°C.

2.18.2 Quantitative real-time PCR (qPCR)

Relative expression levels of genes of interest were evaluated by quantitative real-time PCR (qPCR), using gene specific primer pairs (Table 6). The reactions were carried out by amplification through PowerTrack™ SYBR Green Master Mix (ThermoFisher Scientific) for, following manufacturer's instructions. Mix and cDNA were pipetted in 384-well plates and read using the Quant Studio 6 Pro instrument (ThermoFisher Scientific). Detection for each sample was done in duplicates. The Design & Analysis Software (Version 2.6.0) was used to design the plate layouts and for processing of data. Gene expression analysis was performed according to Pfaffl using one or two reference genes (Pfaffl, 2004).

2.19 Transcriptomic analysis

2.19.1 Bulk RNA-sequencing and analysis

Subpopulations were sorted as described above and immediately stored in TRIzol. RNA library preparation and bulk sequencing was done by the PRECISE platform (Bonn). Total RNA was extracted using the miRNeasy Micro kit (Qiagen) according to manufacturer's protocol. RNA was quantified and RNA integrity was determined using the HS RNA assay on a Tapestation 4200 system (Agilent). Smart-seq2 was used for the generation of non-

strand-specific, full transcript sequencing libraries using standard reagents and procedures as previously described (Picelli et al., 2014). Briefly, 250 pg of total RNA was transferred to buffer containing 0.2 % TritonX-100, protein-based RNase inhibitor, dNTPs, and oligo-dT oligonucleotides to prime the subsequent RT reaction on polyadenylated mRNA sequences. The SMART RT reaction was performed at 42°C for 90 min using commercial SuperScript II (Invitrogen) and a TSO. A preamplification PCR of 14 cycles was performed to generate double-stranded DNA from the cDNA template. At least 200 pg of amplified cDNA were used for tagmentation reaction and subsequent PCR amplification using the Nextera XT kit (Illumina) to construct sequencing libraries. Libraries were quantified using the Qubit HS dsDNA assay, and library fragment size distribution was determined using the D1000 assay on a Tapestation 4200 system (Agilent). Samples were pooled and clustered at 1.25 nM on a NovaSeq6000 system (Illumina) to generate ~10 M single-read (75 bp) reads per sample using a NovaSeq6000 XP kit. Raw sequencing data were demultiplexed using bcl2fastq2 v2.20.

The RNA-seq 3' data were processed with nf-core RNA-seq v1.4.2 (Ewels et al., 2020) pipeline using STAR (Dobin et al., 2013) for alignment and featureCounts for gene quantification (Liao et al., 2014). Statistical analysis was performed in the R environment (R Core Team, 2019) with the Bioconductor R-package DESeq2 (Love et al., 2013). The Benjamini-Hochberg method was used to calculate multiple testing adjusted p-values. Only genes with at least 10 read counts in at least 2 samples and at least 20 read counts in total across all samples were considered for analysis. Data visualizations were generated using R-packages ggplot2 (v3. 3.3). GO term and pathway enrichment analysis for differently expressed genes (FDR < 0.05, Fisher test) was performed using the Bioconductor packages packages fgsea, goseq, and clusterProfiler.

2.19.2 Single-cell RNA-sequencing

Total SVF from murine iWAT was isolated as described above. Single-cell library preparation and sequencing was performed by Dr. Nelli Blank in the lab of Elvira Mass and was based on the Seq-Well S^3 protocol (Hughes et al., 2020), using two arrays per sample. Seq-Well arrays were prepared as described before (Gierahn et al., 2017). Each array was loaded with approximately 110,000 barcoded mRNA capture beads (ChemGenes, Cat: MACOSKO-2011-10) and with 30,000 cells. The procedure was done

as previously described (Hughes et al., 2020). After cell loading, cells were lysed, mRNA captured, and cDNA synthesis was performed. For whole transcriptome amplification, beads from each array were distributed in 18-24 PCR reactions containing approximately 3,000 beads per PCR reaction using KAPA HiFi Hotstart Readymix PCR Kit (Kapa Biosystems, Cat: KK2602) and SMART PCR Primer. 6-8 PCR reactions were pooled and purified with AMPure XP SPRI Reagent (Beckman Coulter). For the library tagmentation and indexing, 200 pg of DNA from the purified WTA from each pool were tagmented with the Nextera XT DNA Library Preparation Kit followed by a Tn5 transposase neutralization for 5 min at RT. Finally, Illumina indices were attached to the tagmented products. Library products were purified using AMPure XP SPRI Reagent. Final library quality was assessed using a High Sensitivity D5000 assay on a Tapestation 4200 (Agilent) and quantified using the Qubit high-sensitivity dsDNA assay (Invitrogen). Seq-Well libraries were equimolarly pooled and clustered at 1,25 nM concentration with 10 % PhiX on a NovaSeq6000 system using a S2 flow cell with 100 bp v.1.5 chemistry. Sequencing was performed paired-end using custom Drop-Seq Read 1 primer for 21 cycles, 8 cycles for the i7 index, and 61 cycles for Read 2. Single-cell data were demultiplexed using bcl2fastq2 (v2.20). Fastq files from Seq-Well were loaded into a snakemake-based data pre-processing pipeline (version 0.31, available at https://github.com/Hoohm/dropSeqPipe) that relies on the Drop-seq tools provided by the McCarroll lab (Macosko, Basu et al. 2015). STAR alignment within the pipeline was performed using the murine GENCODE reference genome and transcriptome mm10 release vM16 (Team 2014).

2.19.3 Single-cell RNA-sequencing analysis

The scRNA-seq data analysis was conducted using the Seurat analysis pipeline (version 4.1.1). Analysis was performed in collaboration with Dr. Lisa Steinheuer (AG Kevin Thurley) and Dr. Geza Schermann (AG Carmen Ruiz de Almodovar). To address differences in sequencing depth, the downsampleBatches function from the scuttle package (version 1.0.4) was employed using default parameter settings. Cells expressing fewer than 100 or more than 1,000 genes, as well as those with more than 20 percent mitochondrial genes, were removed. The individual sequencing samples were integrated using 2,000 variable features. Using the first 30 dimensions, the Louvain algorithm

detected 16 cell clusters which were annotated using known marker gene panels. Clusters with less than 60 cells (10 % percentile) were removed from the dataset.

To account for sample size differences due to varying sequencing depths, the *Bbs8*$^{-/-}$ dataset was down-sampled according to the *Bbs8*$^{+/+}$ reference by grouping cells into 10 bins based on their UMAP 1 coordinates. A differential abundance analysis of each APC and FPC subpopulation across genotypes was performed using a Fisher's exact test with p-values corrected using the FDR method. Developmental trajectories within the APC and FPC subpopulations were calculated using the monocle3 package (version 1.0.0). After re-clustering, the graph structure from the *Bbs8*$^{+/+}$ and down-sampled *Bbs8*$^{-/-}$ datasets was learned using default parameters while disabling graph pruning. Pseudotimes were computed using the APC P1 subpopulation as the root.

Further characterization of the FPC population involved an overrepresentation analysis (ORA) employing the C2 MsigDB data repository, using the top 50 up- and down-regulated genes between FPCs and all other cell populations, as described (Kwon et al., 2023). The 50 top and bottom genes were identified by ranking them according to Bonferroni corrected p-values calculated using Seurat's FindMarkers function. The C2 MsigDB data set was filtered for entries with less than 300 members to focus on gene-sets of comparable size to our input data. Finally, the pathway overrepresentation was calculated using the clusterprofiler package (version 3.18.1) with a q-value cutoff of 5 %.

CellChat (v 1.6.1) (S. Jin et al., 2021) was used to analyze possible cell-cell interactions in the data. To find all possible interactions, the 'computeCommunProb' command was used with 'type = "truncatedMean"' and 'trim = 0' arguments. The analysis was run separately on data from *Bbs8*$^{+/+}$ and *Bbs8*$^{-/-}$ mice and compared after merging with the 'mergeCellChat' command. Interaction difference heatmaps were created using the ComplexHeatmap package. In search for vessel-associated APC cells, the Seurat object was subset to contain only the three APC populations with the FPC cluster. The 'FindSubCluster' command was used with 'resolution = 0.3' argument to create 2 subclusters of the APC P2 cluster. The marker list was generated using the 'FindAllMarkers' command with 'logfc.threshold = 0.1' and 'only.pos = T' arguments, from the APC populations, fibroblasts, endothelial cells, and pericytes.

2.20 Software application

In addition to the device-specific software applications, Biorender.com, GraphPad Prism (Version 10), Affinity designer (version 1.10.8), ImageJ (version 2.14.0/1.54f), Microsoft Excel (version 16.94), Microsoft Word (version 16.94), R studio (version 2023.06.1+524), and FlowJo software (Tree Star) were used to analyze and visualize the experimental data and compile this thesis.

2.21 Statistics

Statistical analysis was performed using GraphPad Prism (Version 10). Data represent mean values with standard deviation (± S.D.) from independent experiments (n numbers are indicated), if not stated otherwise. Statistical significances and performed tests are depicted in the respective figures and legends.

3. Results

3.1 AdipoQ – Development of a tool to quantify APC function *in vitro*

3.1.1 The AdipoQ plugins

Quantifying the cell number and the lipid droplet accumulation are essential parameters to assess adipogenesis. The lipid droplet accumulation can be visualized by staining with lipophilic dyes, such as Oil-Red-O, Bodipy, or LD540 (Kraus et al., 2016; Spandl et al., 2009; Targett-Adams et al., 2003), while staining the nucleus with DAPI can be used as a read-out for the cell count. To this end, AdipoQ was developed to provide an automated image analysis tool that can be used within ImageJ. AdipoQ analyzes images acquired from immunofluorescence staining in a two-step process (Fig. 4). First, the AdipoQ Preparator preprocesses the images by minimizing unspecific background noise for optimized segmentation. Subsequently, it creates an object mask by segmenting the images into fore- and background. This is achieved either by selecting from different segmentation strategies based on an intensity threshold or by using machine-learning-based prediction with StarDist (Schmidt et al., 2018). In a second step, the AdipoQ Analyzer quantifies the mask and gives out various parameters, such as number of individual objects (i.e., nuclei or lipid droplets), size of the objects, or intensity of the objects in all image channels. The output files can be read into Excel or R for further downstream analysis. Of note, AdipoQ can also be applied to image analysis of histological sections to analyze adipocyte morphology in tissues (Sieckmann et al., 2022). AdipoQ is an open-source analysis method, providing transparency and accessibility to the user.

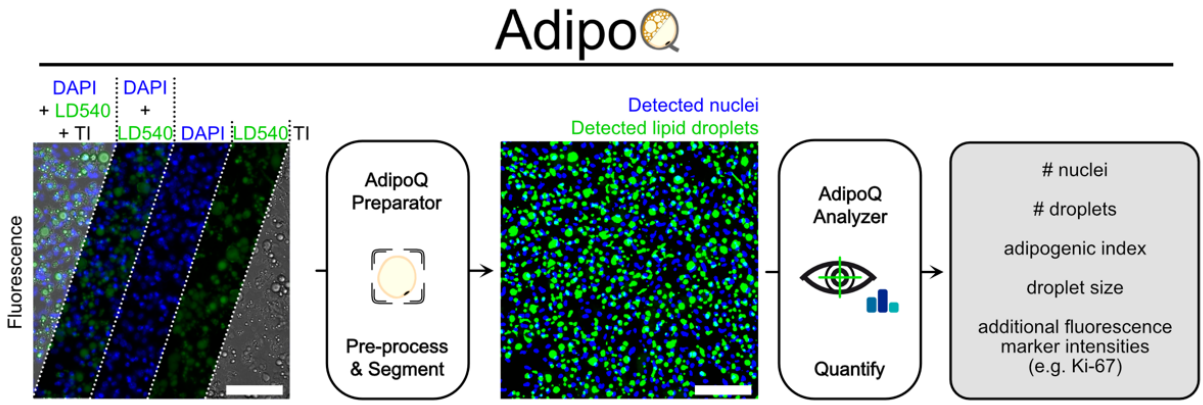

Fig. 4: Establishing an experimental and analysis pipeline to assess adipogenic differentiation *in vitro*. AdipoQ workflow to analyze fluorescence microscopy images of differentiated adipocytes. AdipoQ constitutes two custom-written ImageJ plugins, AdipoQ Preparator and AdipoQ Analyzer. The AdipoQ Preparator pre-processes the images for optimized segmentation and subsequently segments them into fore- and background, generating a mask that reveals the detected structures (i.e., nuclei, lipid droplets). The AdipoQ Analyzer quantifies this mask by counting the structures, determining their size, and their intensity levels within and adjacent to each structure, in all different channels in the image. This allows to measure also additional fluorescent markers. Scale bars = 100 µm. Adapted from Sieckmann *et al.,* 2022.

3.1.2 Analyzing adipogenesis of 3T3-L1 cells using AdipoQ plugins

To test if AdipoQ is a suitable tool to assess adipogenesis, I used the 3T3-L1 cell line, a 3T3 mouse fibroblast sub strain that is committed to the adipocyte lineage (Green & Meuth, 1974). I induced adipogenesis in 3T3-L1 cells using a cocktail containing insulin, dexamethasone, and isobutylmethylxantine (IBMX). Cells were imaged every other day over a period of 8 days to analyze adipogenic differentiation (Fig. 5 a-d).

I first wanted to assess the proliferation of 3T3-L1 cells over the time course of differentiation. AdipoQ uses a machine-learning based detection and therefore enables the quantification of single nuclei and, thereby, the cell numbers. Additionally, I labelled for Ki-67, a nuclear protein whose expression and localization in the nucleus is tightly associated to the cell cycle (D. C. Brown & Gatter, 2002). As AdipoQ allows to measure additional fluorescence markers, I quantified pixel intensities of Ki-67 within each nucleus using the median intensity parameter, which is less sensitive to noise. A fixed threshold was set based on the intensity histogram to distinguish Ki-67- from Ki-67+ nuclei (Fig. 5 b). While the number per nuclei steadily increased over time, both in the control and the differentiated condition, the number of Ki-67+ nuclei increased only in the differentiated

condition (Fig. 5 c). The highest proportion of Ki-67+ cells was observed after 2 days of differentiation, which is in line with the mitotic clonal expansion, which is a prerequisite for adipogenesis in 3T3-L1 cells (Q.-Q. Tang et al., 2002).

Next, I evaluated lipid droplet formation by staining with an antibody against perilipin (PLIN1), a protein that is localizes to the surface layer of lipid droplets (Joan Blanchette-Mackie et al., 1995). This allowed to calculate the adipogenic index, which is the ratio of the PLIN1+ area and the DAPI+ area. Lipid droplet accumulation was already visible two days after induction and increased during differentiation, in line with an increase in the adipogenic index (Fig. 5 d). Even without induction, 3T3-L1 cells can undergo spontaneous differentiation (Carnicero, 1984), which was reflected in an increased adipogenic index in the control condition, albeit to a lesser extend compared to the induced condition (Fig. 5 d). Thus, AdipoQ reliably quantifies different parameters of adipogenesis.

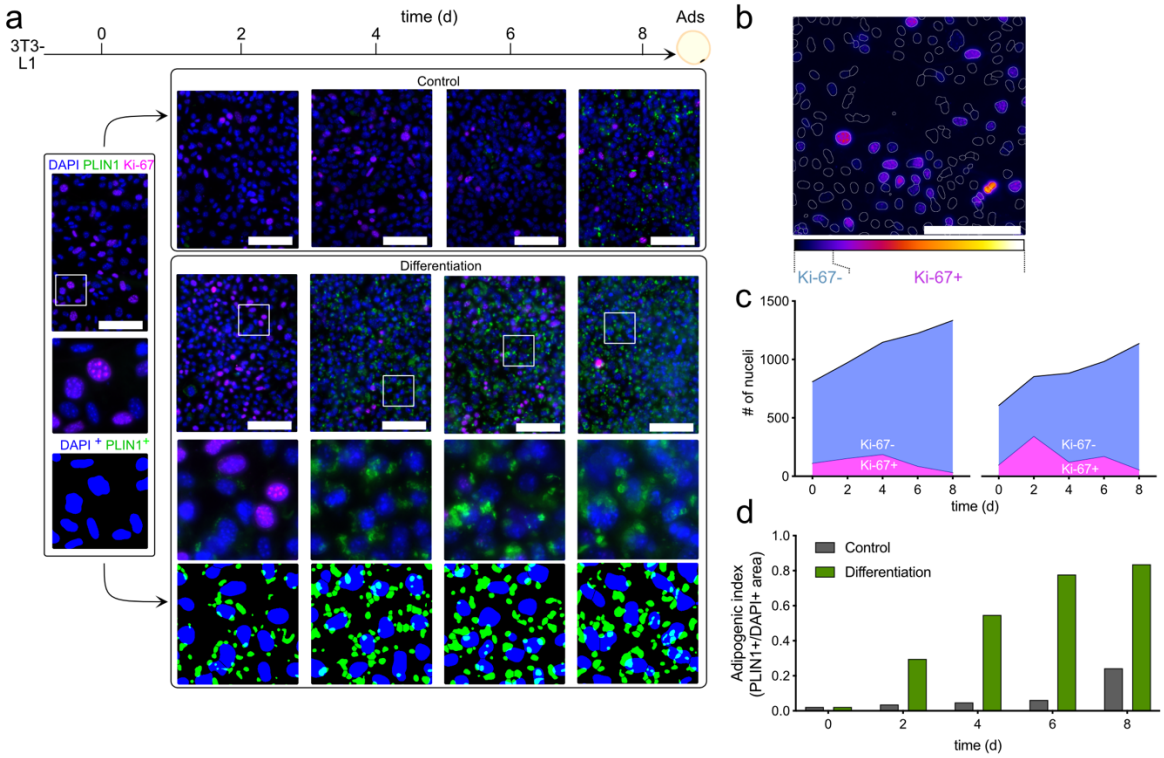

Fig 5: AdipoQ quantifies adipogenesis and proliferation of 3T3-L1 cells *in vitro*. a. Exemplary images of 3T3-L1 cells during adipogenic differentiation, which have been induced at day 0. Cells were fixed at indicated time points and have been labeled with DAPI (DNA, blue), an anti-Ki-67 antibody (magenta), and an anti-PLIN1 antibody (green). Rectangles indicate magnified views below, for which also the detected DAPI+ and

PLIN1+ areas are indicated. Scale bars = 100 µm. **b.** Quantifying adipocyte proliferation using Ki67 staining. Ki67 channel shown for an example image (colored by the look-up table indicated below). Masks for individual nuclei (overlayed with white lines in image) are determined from the DAPI channel. For each nucleus mask, the Ki67 signal is determined and if the median intensity within the mask exceeds a fixed threshold, the nucleus is considered Ki67+. **c.** Proliferation kinetics of 3T3-L1 cells as indicated by the total number of nuclei and the nuclei that showed a high Ki-67 intensity (Ki-67+). d. Adipogenic index, determined by calculating the total lipid droplet area (PLIN1+) and dividing it by the total nuclei area (DAPI+). Bars show mean (average of four images per experiment). experimental numbers equal n = 1. Adapted from Sieckmann *et al.,* 2022.

3.1.3 Analyzing adipogenesis of primary APCs *in vitro* using AdipoQ plugins

To test whether the AdipoQ pipeline can be applied to primary cells, I isolated APCs from murine inguinal (i) WAT and performed an adipogenesis assay. I induced the cells with the induction cocktail, which additionally contained rosiglitazone, among the previously mentioned components. Rosiglitazone, a PPARγ agonist, potently induces adipogenesis (Gurnell et al., 2003) and is necessary to evoke a maximum adipogenic response in primary APCs. I generated images of the differentiating cells every other day for a duration of 7 days (Fig. 6 a). First, I assessed the proliferation rate in the primary APCs by Ki-67 labeling. As in 3T3-L1 cells, the number of Ki-67+ cells increased after two days of differentiation. Thus, primary APCs also undergo mitotic clonal expansion as a critical first step during adipogenesis (Fig. 6 b) (M. L. Zhao et al., 2020).

To scrutinize the ability of AdipoQ in assessing lipid accumulation, I took an alternative approach to stain lipid droplets using the lipophilic dye LD540 (Spandl et al., 2009) (Fig. 6 a). Hence, the adipogenic index was calculated as the ratio of the LD540+ area to the DAPI+ area (Fig. 6 c). Lipid droplets accumulated 2 days after induction and the adipogenic index increased over the course of 7 days (Fig. 6 c). Some lipid droplets were also formed in the untreated control, indicating that also primary APCs can spontaneously differentiate. Thus, AdipoQ is also suitable to assess adipogenesis in primary APCs.

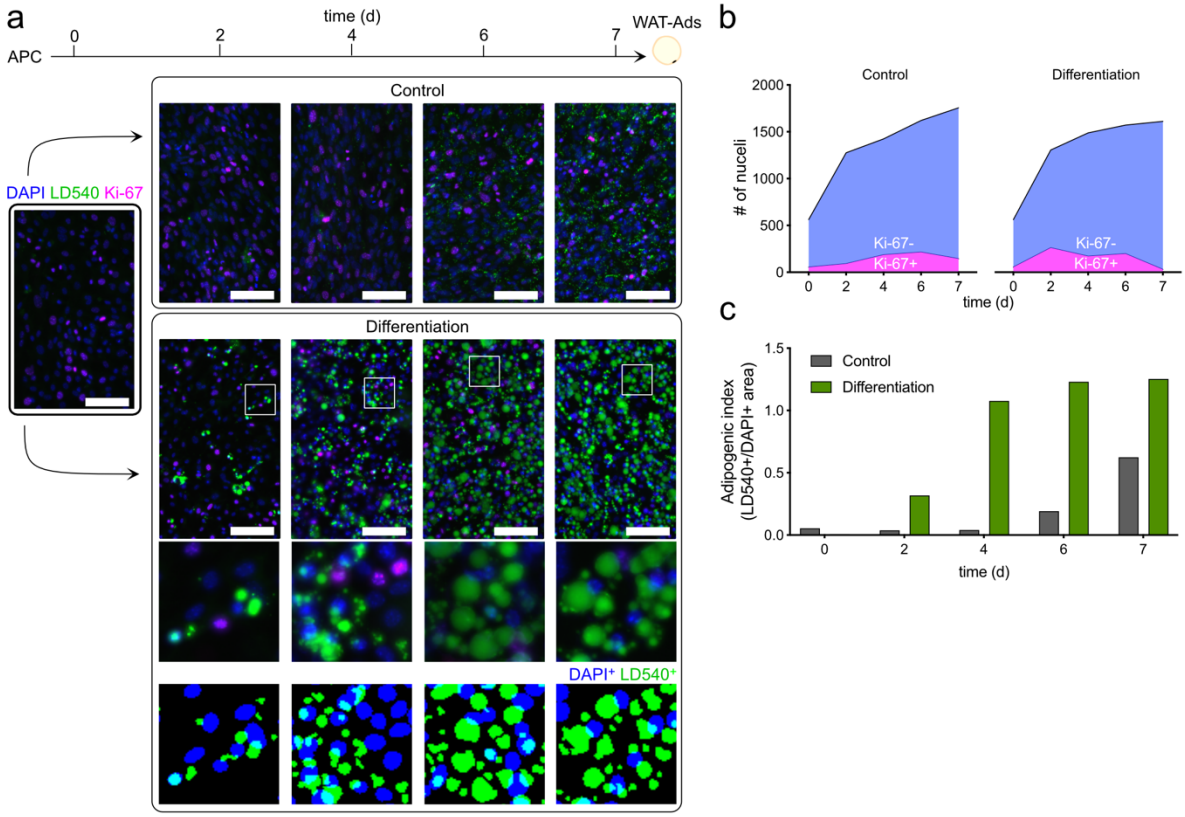

Fig. 6: AdipoQ quantifies adipogenesis and proliferation of APCs *in vitro*. a. Exemplary images of APCs during adipogenic differentiation, which have been induced at day 0. Cells were fixed at indicated time points and have been labeled with DAPI (DNA, blue), an anti-Ki-67 antibody (magenta), and LD540 (lipid droplets, green). Rectangles indicate magnified views below, for which also the detected DAPI+ and LD540+ areas are indicated. Scale bars = 100 µm. **b.** Proliferation kinetics of APCs as indicated by the total number of nuclei (Ki-67-, blue) and the nuclei that showed a high Ki-67 intensity (Ki-67+, magenta). **c.** Adipogenic index, determined by calculating the total lipid droplet area (LD540+) and dividing it by the total nuclei area (DAPI+). Bars show mean (average of four images per experiment). Experimental numbers equal n = 1. Adapted from Sieckmann *et al.,* 2022.

3.2 Characterizing APC subpopulations *in vitro*

3.2.1 Isolation of APC subpopulations

Recent single-cell transcriptomic analyses have provided detailed insight into the heterogenic nature of APCs (Burl et al., 2018; Cho et al., 2019; Merrick et al., 2019; Nahmgoong et al., 2022; Schwalie et al., 2018; Shao et al., 2021; Spallanzani et al., 2019; H. Wang et al., 2024). Although a consistent definition of the precursor subpopulations is lacking, there is a consensus that APCs exist along a differentiation spectrum, ranging from a more stem-cell-like state to a high commitment to the adipocyte lineage (Fig. 7 a)

(Ferrero et al., 2020). Additionally, a third APC population has been described as a regulator of adipogenesis (Schwalie et al., 2018). Our lab has previously established a strategy to identify the three subpopulations based on their surface marker expression (Fig. 7 b-d). All subpopulations are defined by their lack of Lin markers (Lin: TER119$^+$, CD45$^+$, and CD31$^+$), while being enriched for CD29$^+$ (Integrin b1) and SCA1$^+$ APCs. The multipotent P1 APCs are identified by CD55 and CD26 (DPP4) expression. The committed P2 APCs express CD54 (ICAM-1), while the P3 subpopulation is defined by the marker CD142 (tissue factor) (Fig. 7 b-d). In the iWAT of lean wild-type mice the P1 is the most abundant subpopulation, making up around 71.4 ± 6.2 % of all Lin-CD29+Sca+ APCs, while the P2 makes up only 17.6 ± 6.2 % of all APCs (Fig. 7 e). The regulatory P3 is the least abundant population, only consisting of 4.1 ± 2.7 % (Fig 7 e.). Of note, the subpopulations were investigated in young mice at the age of 6-9 weeks. Factors such as age, diet, or adipose tissue depot can affect their abundance: While the iWAT harbors the highest abundance of stem-cell like APCs, in gonadal (g) WAT depots, the committed CD54+ APCs and CD142+ APCs are the most abundant population (J. H. Lee et al., 2022; Merrick et al., 2019; Schwalie et al., 2018). In response to high-fat diet feeding of mice, a shift was observed towards an increased abundance of committed CD54+ cells, both in the iWAT and the gWAT (Merrick et al., 2019).

For further downstream analysis, I established a strategy to sort the subpopulations for *in vitro* characterization either by fluorescent-activated cell sorting (FACS) or magnetic-activated cell sorting (MACS) (Fig. 7 f) and tested whether the different subpopulations maintain their *in vivo* characteristics when cultured *in vitro* for 48 hours. A main characteristic that distinguishes the subpopulations is their degree of adipogenic commitment. This degree of differentiation can be analyzed via staining of FABP4, as it is only expressed in later stages of adipogenesis (Samulin et al., 2008; Shan et al., 2013). Since the P3 APCs only make up only a small fraction of all APCs and they are resistant to undergoing adipogenesis (Schwalie et al., 2018), I focused only on the P1 and P2 APCs. With both fluorescent- and magnetic-based sorting approaches, only a few P1 were FABP4$^+$ (16.4 ± 18.8 %) (Fig. 7 g), underlining that P1 cells are not yet committed and more stem-cell like. In contrast, 69.1 ± 13.4 % of FACS-sorted P2 cells were FABP4$^+$ (Fig. 7 g). As P2 cells are already committed to the adipogenic lineage, these results are consistent to what has been described *in vivo* (Merrick et al., 2019; Schwalie et al., 2018).

However, MACS sorting of P2 cells only yielded 9.7 ± 4.8 % of FABP4^{+} cells (Fig. 7 g). With this approach, the number of antibodies is limited: I first depleted the lineage-positive cells (TER119, CD45, CD31) and then enriched for expression of the P2 marker CD54. However, P3 APCs are also expressing CD54, along their specific marker CD142 (Fig. 7 c-d). Thus, the MACS sorting results in a rather pure P1 population and a mixed population of P2 and P3, which explains the lower proportion of FABP4+ cells in this fraction.

Concluding, both FACS and MACS allow successful sorting of P1 cells, while only FACS ensures pure enrichment of P2 cells.

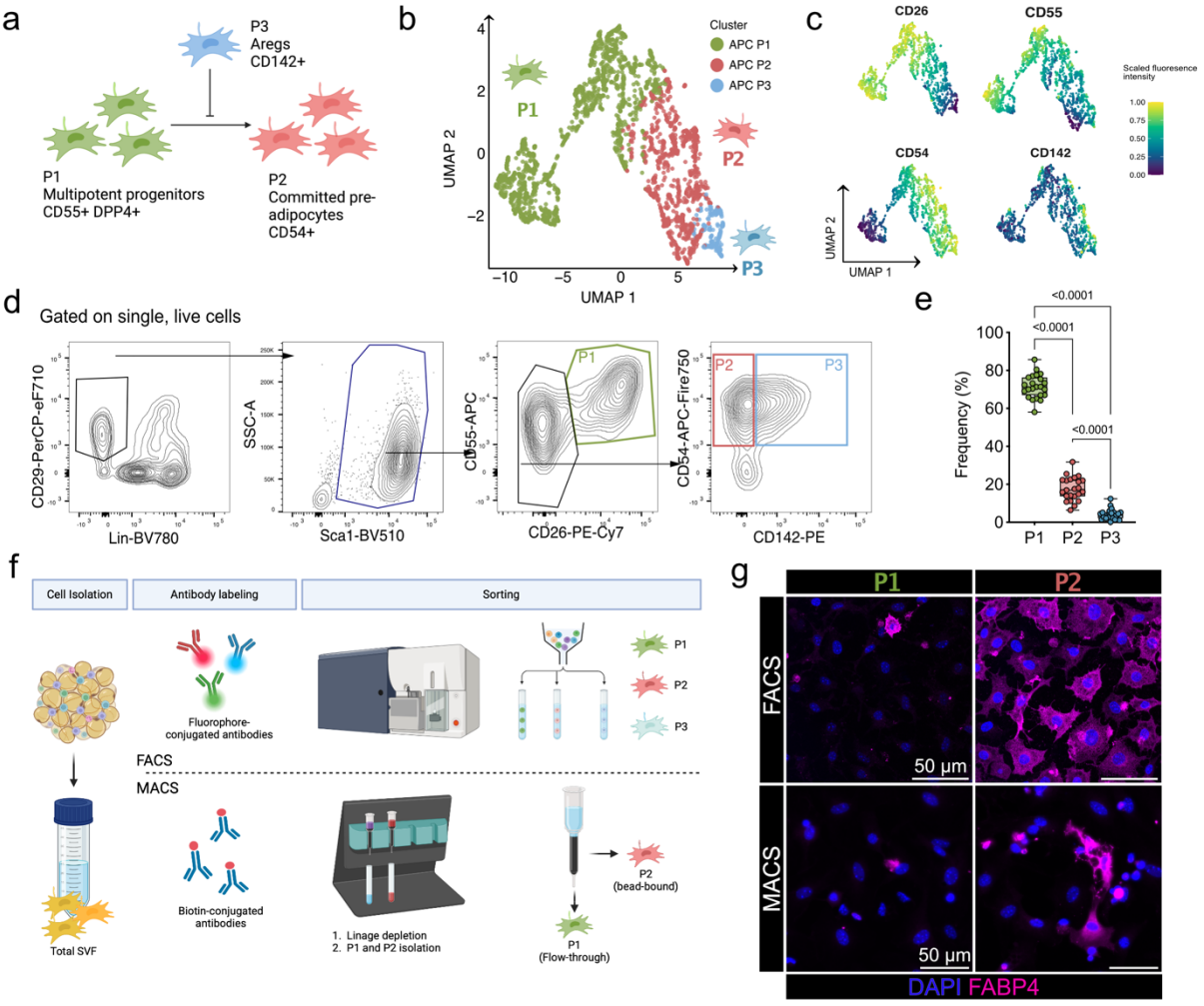

Fig. 7: Different subpopulations of adipocyte precursor cells (APC) can be identified via flow cytometry or magnetic-activated cell sorting. a. Schematic model of the three APC subpopulations (P1, P2, and P3) regarding their function and surface marker expression. **b.** Multi-dimensional reduction analysis from flow cytometry data from

iWAT of lean wild-type mice at 6-9 weeks based on the expression of the surface marker CD26, CD55, CD54, and CD142. The Uniform Manifold Approximation and Projection (UMAP) is subdivided into the three distinct APC clusters. **c.** Scaled fluorescence intensities of the markers is overlayed over the UMAP from b., highlighting the contribution of each marker to the respective clusters. **d.** Contour plot of the gating strategy to distinguish the APC subpopulations. **e.** Frequencies of APC P1-P3 gated from the total APC pool ($SCA1^+$) of lean wild-type mice. Data are shown as ± SD, with individual data points; p-values were determined using a one-way ANOVA. Post-hoc p-value correction for multiple testing was performed using Tukey adjustment, experimental numbers equal n = 24. **f.** Experimental set-up of isolating the APC subpopulations from murine iWAT either via fluorescence-activated cell sorting (FACS) or magnetic-activated cell sorting (MACS). **g.** Representative images of FACS- or MACS-sorted P1 and P2 APCs. Cells have been labeled with DAPI (DNA, blue) and an anti-FABP4 antibody (magenta). Scale bars are indicated. Adapted from Sieckmann *et al.,* 2024 (bioxRiv).

3.2.2 Primary cilia signaling in APC subpopulations

I hypothesize that the fate and function of APCs in WAT are governed by the primary cilium. Thus, I first verified that all subpopulations are ciliated. To this end, I sorted the subpopulations via FACS and analyzed ciliation after 48 h in culture. The APCs of all three subpopulations displayed a primary cilium (Fig. 8 a): P1 cells showed the highest proportion of ciliated cells (69.4 ± 14 %) followed by P2 (46 ± 10.6 %) and P3 (27.8 ± 3.9 %) (Fig. 8 b). During adipogenesis, the APCs lose their primary cilium, and mature adipocytes are not ciliated (Hilgendorf et al., 2019; Marion et al., 2008b). Thus, the lower percentage of ciliated cells in the P2 could reflect their differentiation status as these cells might be in the process of disassembling the primary cilium. In line with this, ciliary length was decreased in P2 cells compared to P1 and P3 APCs (Fig. 8 c). As the primary cilium is only present during G0 and G1 phase and is absent in cycling cells, the varying proportion of ciliated cells might also be attributed to different stages of cell cycle progression since cells were not starved. However, strategies to promote cell cycle arrest, such as prolonged culture or serum starvation, could distort the actual *in vivo* phenotype of the cells. Thus, a 48-h culture period after sorting was chosen to allow cell attachment to the plastic and clearance of apoptotic cells within a rather short timeframe.

To investigate primary cilia function in APCs, I performed an adipogenesis assay with the P1 and P2 enriched by MACS as this resulted in a higher yield and viability compared to FACS. However, as the P2 fraction enriched by MACS also contains P3 APCs, this could

negatively influence adipogenesis of other cells (Schwalie et al., 2018). However, the regulatory effect of the P3 has been under debate, as other studies were not able to reproduce the results of Schwalie et al. (Merrick et al., 2019). My results demonstrated that both P1 and P2/3 subpopulations readily differentiated into mature adipocytes upon treatment with the full induction cocktail (Fig. 8 d, e). To investigate the cilia-specific effects on adipogenesis, I used a minimal induction cocktail, which has previously been established in our lab in accordance with the “control cocktail” proposed by Hilgendorf et al (Hilgendorf et al., 2019). The minimal induction cocktail contains a lower amount of the adipogenic inducers insulin, IBMX, and dexamethasone, while the PPARγ-activator rosiglitazone is omitted to achieve a more sensitive system. Even under the minimal conditions, some P2 cells already differentiated into mature adipocytes, further underlining their high commitment to the linage (Fig. 8 e). In contrast, P1 cells had a significantly lower adipogenic index in accordance with their more stem cell-like characteristic (Fig. 8 e). Next, I investigated if the subpopulations respond to ciliary signaling cues. The FFAR4 resides in the ciliary membrane of APCs and induces ciliary signaling to promote adipogenesis when activated (Hilgendorf et al., 2019). I used the FFAR4 agonist TUG-891 to activate FFAR4 signaling in the APCs and in both subpopulations, a significant increase of the adipogenic index was observed (Fig. 8 e). In both P1 and P2, the addition of TUG-891 resulted in a similarly high adipogenic index as when using the full induction cocktail, showing that ciliary signaling evokes a maximum adipogenic response (Fig. 8 e). Thus, ciliary FFAR4-dependent signaling promotes adipogenesis of P1 and P2 APCs.

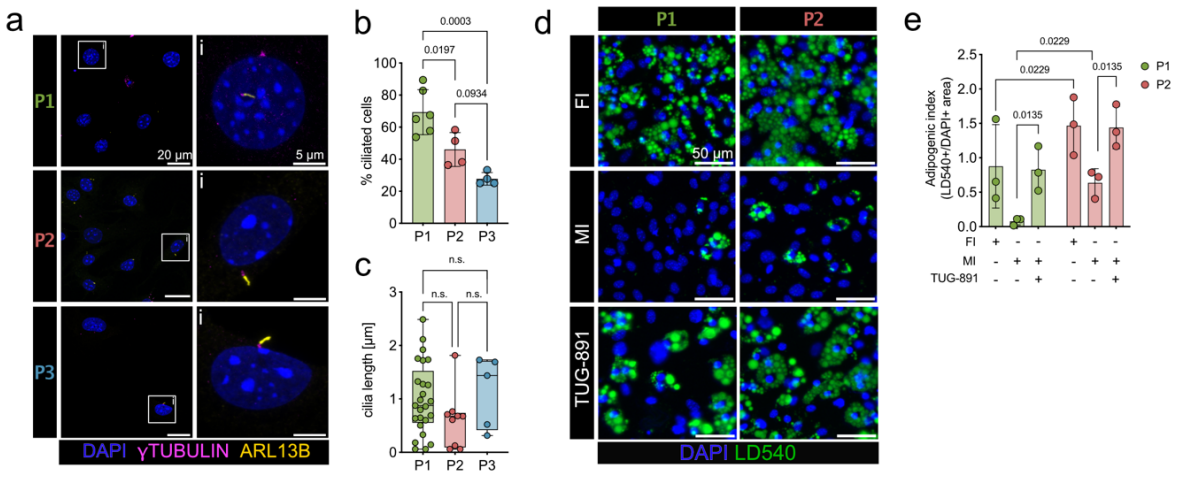

Fig. 8 (figure legend on next page)

Fig. 8: Identification of primary cilia and response to cilia specific cues of the three APC subpopulations. a. Representative images of FACS-sorted P1, P2, and P3 APCs. Cells have been labeled with DAPI (DNA, blue), an anti-γTUBULIN antibody (magenta), and an anti-ARL13b antibody (yellow). Squares indicate the magnified views on the right. Scale bars are indicated. **b.** Quantification of ciliated cells by dividing the number of primary cilia by the total number of nuclei per image. **c.** Quantification of ciliary length was performed using CiliaQ. Data are shown mean ± SD, with each data point representing (**b.**) one image or (**c.**) individual cilium; Data are shown as ± SD, with individual data points; p-values were determined using a one-way ANOVA. Post-hoc p-value correction for multiple testing was performed using Tukey adjustment, experimental numbers equal n = 3 mice. **d.** Exemplary images of *in-vitro* differentiated P1 and P2 APCs. Cells were differentiated under full induction (FI), or minimal induction (MI) with or without the addition if TUG-891 (100 µM). Cells have been labeled with DAPI (DNA, blue) and LD540 (lipid droplets, green). **e.** Adipogenic index, determined by calculating the total lipid droplet area (LD540+) and dividing it by the total nuclei area (DAPI+). Data are shown mean ± SD, with each data point representing the mean of four images from one well; p-values were determined using a two-way ANOVA. Post-hoc p-value correction for multiple testing was performed using Tukey adjustment, experimental numbers equal n = 3 mice. Adapted from Sieckmann *et al.,* 2024 (bioxRiv).

3.3 Ciliopathy mouse models

3.3.1 Obesity phenotype of the classical *Bbs8* line

I have demonstrated that ciliary signaling is important in APCs during adipogenesis. In turn, I hypothesize that ciliary dysfunction disturbs APC fate and function. To test this hypothesis, I used a transgenic mouse model that constitutively lacks BBS8 (*Bbs8*$^{-/-}$), a component of the BBSome (Tadenev et al., 2011). The knock out has been generated by integrating a tau:YFP cassette in the start codon and first two exons (Fig. 9 a) (Tadenev et al., 2011). The mouse line has previously been characterized in our lab and resembles the obesity phenotype of the BBS (Galindo, 2024; Klausen, 2020; Winnerling, 2022): To analyze obesity development, *Bbs8*$^{+/+}$ and *Bbs8*$^{-/-}$ mice were weighed every two weeks, and a relative weight gain was calculated by normalizing to the mean weight of each genotype of the lean timepoint (Fig. 9 b). Here, the lean timepoint was defined based on the mean body weight with the most similar value and the smallest standard deviation. Accordingly, *Bbs8*$^{-/-}$ mice are lean until 10 weeks and subsequently develop obesity (Fig. 9 b-c). This weight gain is accompanied by a significant increase of the gWAT and iWAT depot (Fig. 9 d-e). As studies have shown that a sex dimorphism exists in lipid storing organs (Palmer & Clegg, 2015; Varghese et al., 2019), I stratified the WAT weights accordingly. Regardless, a similar trend was observed across gender and adipose tissue

depots: at a young age (5-7 weeks), gWAT and iWAT weights show no difference between *Bbs8*$^{-/-}$ and *Bbs8*$^{+/+}$ mice (Fig. 9 d-e), whereas at an older age (15-20 weeks), both WAT depots were significantly increased in the *Bbs8*$^{-/-}$ mice. compared to *Bbs8*$^{+/+}$ mice (Fig. 9 d-e). In summary, the *Bbs8*$^{-/-}$ mice resemble BBS as they develop obesity over time, accompanied by an increase in WAT mass.

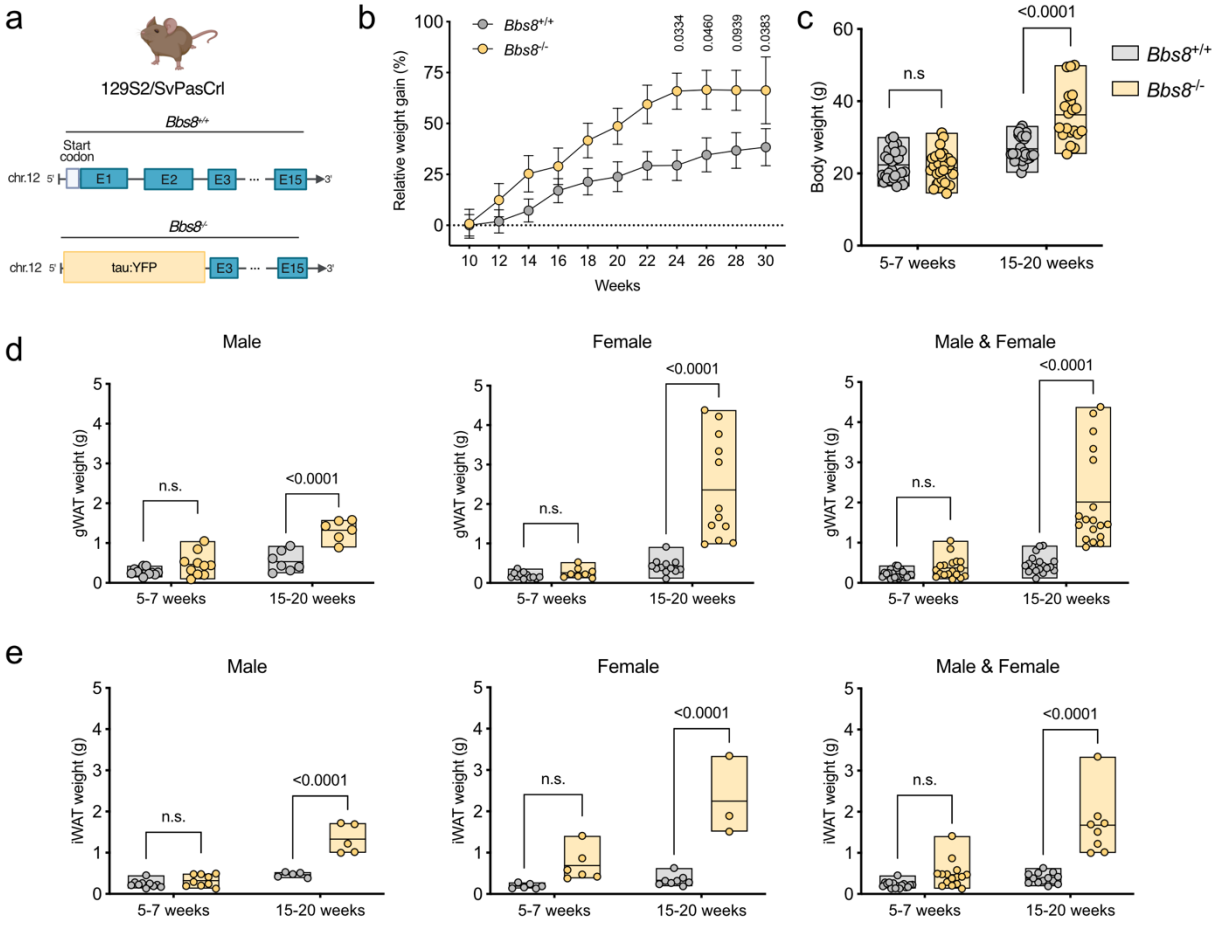

Fig. 9: Weight gain of the *Bbs8* mouse model. a. Schematic representation of the generation of the *Bbs8* knockout by integrating a tau:YFP cassette that deletes the *Bbs8* start codon. **b.** Relative body weight gain of *Bbs8*$^{+/+}$ and *Bbs8*$^{-/-}$ mice under standard chow diet. Weights were normalized to the mean body weight of their respective genotypes at a lean time point (10 weeks). Data are shown mean ± SEM, p-values were determined using a Two-way ANOVA with repeated measurements (mixed models). Post-hoc p-value correction for multiple testing was performed using Bonferroni adjustment, experimental numbers equal n ≥ 14. **c.** Body weight of *Bbs8*$^{+/+}$ and *Bbs8*$^{-/-}$ mice at a young (5-7 weeks) and older (15-20 weeks) timepoint. Data are shown mean ± SD, with individual data points; p-values were determined via an unpaired t-test, experimental numbers equal n ≥ 20. **d, e.** White adipose tissue (WAT) mass increase of **d.** gWAT and **e.** iWAT in *Bbs8*$^{+/+}$ and *Bbs8*$^{-/-}$ mice at a young (5-7 weeks) and older (15-20 weeks) timepoint. Data are

shown as ± SD, with individual data points; p-values were determined using a Two-way ANOVA with repeated measurements (mixed models). Post-hoc p-value correction for multiple testing was performed using Šidák adjustment, experimental numbers equal n ≥ 3. N.s. = non-significant.

3.3.2 Obesity phenotype of a *Bbs8* knockout line with conditional potential

To investigate the contribution of the mesenchymal lineage, specifically APCs, to WAT remodeling, I generated a BBS8 knockout model with conditional potential. To this end, I used embryonic stem cells with a "knockout-first" strategy to generate knockout mice (Coleman et al., 2015; Skarnes et al., 2011). Here, a gene-trap knockout targeting cassette, which contains a β-galactosidase (*lacZ*) cassette and a neomycin-resistance cassette (neo), flanked by two flippase recognition targets (*FRT*) and three *loxP* sites, is integrated into the locus, which disrupts splicing of the gene, thereby creating a global knockout (Fig. 10 a). Thus, my first aim was to characterize this *Bbs8* knockout model (*Bbs8*$^{-(KOMP)/-(KOMP)}$) regarding obesity development compared to the classical *Bbs8*$^{-/-}$ mouse model. Of note, the "knockout-first" strategy has been generated in the C57BL/6 strain background (Coleman et al., 2015), whereas the *Bbs8*$^{-/-}$ mouse model has been generated on a 129/Sv background (Tadenev et al., 2011). Both mouse strains are widely used, however, they have been described to differ in their body weight change and metabolic performance (Piirsalu et al., 2022). According to the relative weight gain, the lean timepoint of *Bbs8*$^{-(KOMP)/-(KOMP)}$ mice was defined at 6 weeks of age (Fig. 10 b). *Bbs8*$^{-(KOMP)/-(KOMP)}$ gained weight over time and were significantly heavier compared to their wild type littermates after 17 weeks (Fig. 10 c). This was also reflected in their WAT weights: at a younger age, no significant difference was observed between both genotypes, while gWAT and iWAT depots were significantly increased after 17 weeks in *Bbs8*$^{-(KOMP)/-(KOMP)}$ mice (Fig. 10 d-e). This showed that the alternative approach of creating a *Bbs8* knockout was leading to similar changes in weight gain as in the classical *Bbs8*$^{-/-}$ mice, demonstrating that both models are suitable to investigate effects of a dysfunctional primary cilium in WAT development.

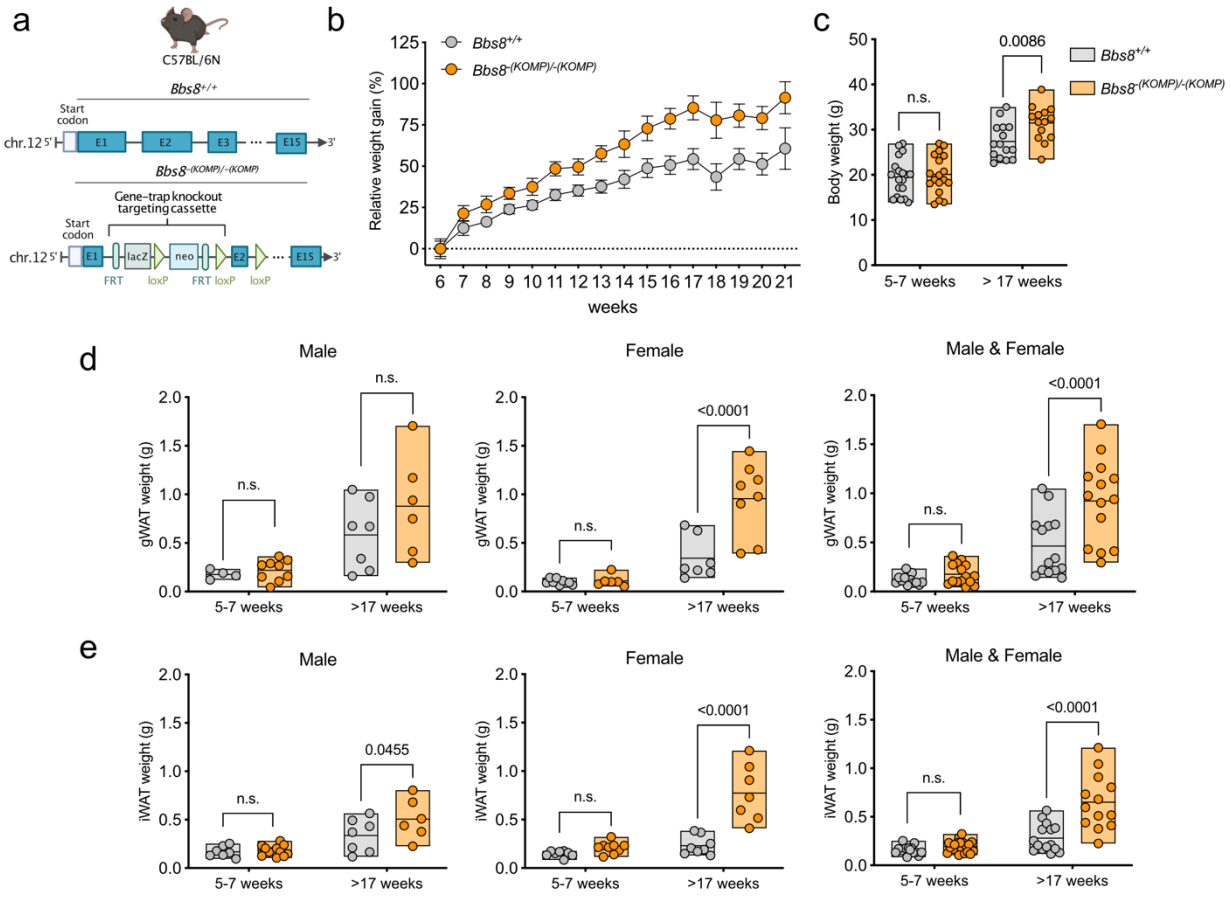

Fig. 10: Weight gain of the *Bbs8*-KOMP mouse model. a. Schematic representation of the generation of the *Bbs8*$^{-(KOMP)/-(KOMP)}$ mouse line via the knockout-first strategy. **b.** Relative body weight gain of *Bbs8*$^{+/+}$ and *Bbs8*$^{-(KOMP)/-(KOMP)}$ mice under standard chow diet. Weights were normalized to the mean body weight of their respective genotypes at the lean time point (6 weeks). Data are shown mean ± SEM, experimental numbers equal n ≥ 18. **c.** Body weight of *Bbs8*$^{+/+}$ and *Bbs8*$^{-(KOMP)/-(KOMP)}$ mice at a young (5-7 weeks) and older (>17 weeks) timepoint. Data are shown mean ± SD, with individual data pints, p-values were determined via an unpaired t-test, experimental numbers equal n ≥ 14. **d, e.** WAT mass increase of **d.** gWAT and **e.** iWAT in *Bbs8*$^{+/+}$ and *Bbs8*$^{-(KOMP)/-(KOMP)}$ mice at a young (5-7 weeks) and older (>17 weeks) timepoint. Data are shown as mean ± SD, with individual data points; p-values were determined using a Two-way ANOVA with repeated measurements (mixed models). Post-hoc p-value correction for multiple testing was performed using Šidák adjustment, experimental numbers equal n ≥ 4. FRT = flippase recognition target; lacZ = β-galactosidase, neo = neomycin-resistance cassette; N.s. = non-significant.

3.3.3 WAT histology of *Bbs8* knockout mouse models

The mechanism of WAT expansion is a critical determinant of metabolic homeostasis: WAT expansion via hyperplasia is associated with a metabolically healthy obese state,

while expansion via hypertrophy is strongly related to the development of metaflammation and other obesity-related (Ghaben & Scherer, 2019; Vegiopoulos et al., 2017). I aimed to investigate how the WAT expands in the two different *Bbs8* knockout mouse models using histological analyses. To this end, I only analyzed the gWAT, which is part of the visceral WAT, and has a greater impact on metabolism compared to iWAT (Imbeault et al., 1999). The adipocyte size distribution showed a strong shift toward larger cell sizes in the gWAT from obese *Bbs8*$^{-/-}$ and *Bbs8*$^{-(KOMP)/-(KOMP)}$ compared to their respective age-matched, lean wild-type littermates (Fig. 11 a-d). Thus, both models expanded by hypertrophy. Interestingly, previous data generated by Nora Winnerling demonstrated that obese *Bbs8*$^{-/-}$ mice showed a milder metabolic impairment compared to diet-induced obese wild-type mice (Winnerling, 2022). As WAT expansion via hyperplasia does not appear to underlie this healthier phenotype, I hypothesize that *Bbs8*-dependent changes in APCs might play an alternative role in WAT remodeling, thereby altering the systemic metabolism.

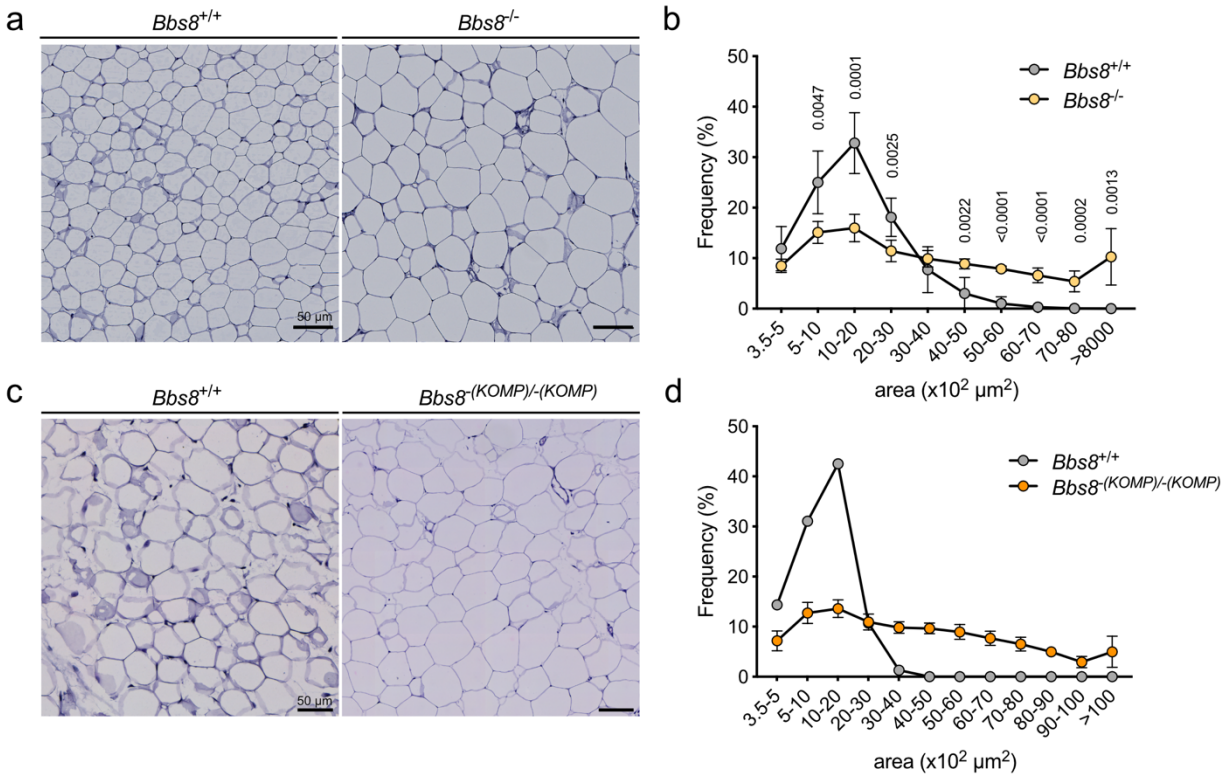

Fig. 11: Analysis of adipose tissue morphology in Bbs8 knockout mouse models. **a.** Representative images of gWAT section stained with hematoxylin and eosin (HE) form *Bbs8*$^{+/+}$ and *Bbs8*$^{-/-}$ aged 21 weeks. **b.** Frequency of adipocyte size distribution quantified by analyzing images as exemplified in **a**, acquired from female and male *Bbs8*$^{+/+}$ (n = 7) and *Bbs8*$^{-/-}$ (n = 8) mice. Per mouse, two to six sections were quantified; p-values were determined by an unpaired, two-sided t-test with Welch correction. **c.** Representative

images of gWAT section stained with hematoxylin and eosin (H&E) form *Bbs8*$^{+/+}$ and *Bbs8*$^{-/-}$ aged 21-31 weeks. **d.** Frequency of adipocyte size distribution quantified by analyzing images as exemplified in **c**, acquired from female and male *Bbs8*$^{+/+}$ (n = 1) and *Bbs8*$^{-(KOMP)/-(KOMP)}$ (n = 3) mice. Per mouse, two to three sections were quantified. Data are shown as mean ± SD. Scale bars are indicated.

3.3.4 Obesity phenotype of a conditional knockout of *Bbs8* in *Pdgfra*-expressing cells

Since the *Bbs8*$^{-(KOMP)/-(KOMP)}$ mice resembled the classical knockout, I generated conditional *Bbs8* knockout mice. To this end, the *Bbs8*$^{-(KOMP)/-(KOMP)}$ mice are first crossed with transgenic C57BL/6J mice expressing an enhanced variant of FLP1 recombinase (FlpE) (Fig. 12 a). This restores *Bbs8* expression, thereby producing a pseudo wild-type offspring, as both the *lacZ* and the *neo* cassette are removed, leaving only two flanking *loxP* sites. The offspring can then be crossed to different mouse lines, expressing the Cre recombinase in a cell-type specific manner to delete *Bbs8* (Fig. 12 a). To target APCs, no suitable marker has been defined that reliably targets these cells (Berry et al., 2015; Krueger et al., 2014). A commonly used Cre-recombinase for targeting APCs is the *Fabp4*-Cre line. However, this Cre is only active in a small subset of committed APCs (Krueger et al., 2014) and would not target APC P1 cells, as demonstrated above (Fig. 12 g). Thus, I used a mouse line that expresses the Cre-recombinase under the control of the platelet-derived growth factor receptor α (*Pdgfra*) promotor, as this has been shown to broadly target mesenchymal stem cells, including APCs (Berry & Rodeheffer, 2013). Consequently, I generated a conditional knockout mouse line, lacking *Bbs8* in *Pdgfra*-expressing cells (*Pdgfra*$^{cre/+}$ *Bbs8*$^{fl/fl}$). Like the global *Bbs8* knockout models, these mice also gained weight at an older age (Fig. 12 b-c). The weight gain was reflected in the WAT depots, which showed a significant increase at 17-21 weeks of age (Fig. 12 d-e). This demonstrates the significant contribution of *Pdgfra*-expressing cells to obesity development and WAT enlargement upon loss of *Bbs8*. For this thesis, all three mouse models were used at a lean state (5-9 weeks) to analyze the effect of Bbs8 deficiency on APCs without the effect of obesity as a confounding variable.

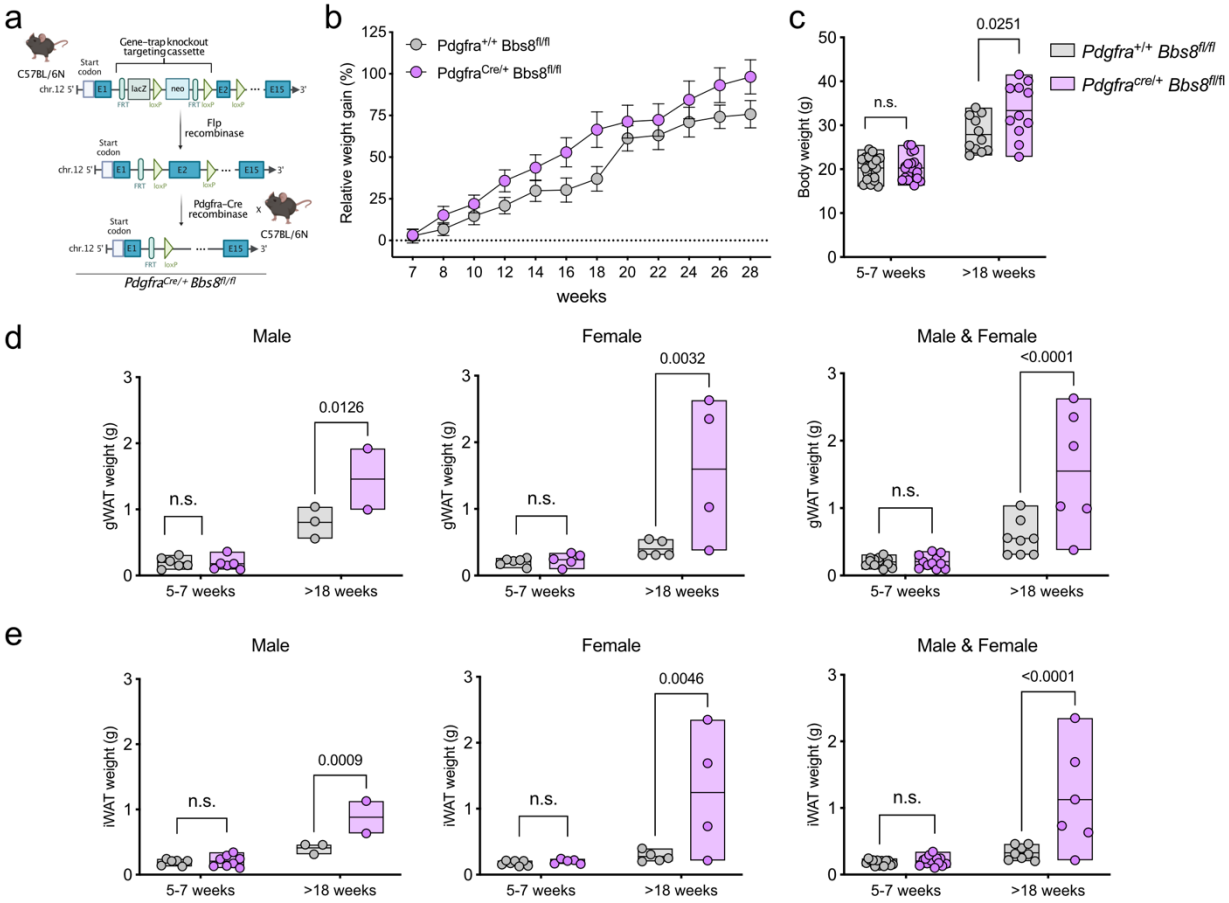

Fig. 12: Weight gain of the *Pdgfra*$^{Cre/+}$ *Bbs8*$^{fl/fl}$ mouse model. a. Schematic representation of the generation of the *Pdgfra*$^{Cre/+}$ *Bbs8*$^{fl/fl}$ mouse line via the knockout-first strategy for creating conditional alleles. **b.** Relative body weight gain of *Pdgfra*$^{+/+}$ *Bbs8*$^{fl/fl}$ and *Pdgfra*$^{Cre/+}$ *Bbs8*$^{fl/fl}$ mice under standard chow diet. Weights were normalized to the mean body weight of their respective genotypes at the lean time point (7 weeks). Data are shown mean ± SEM, experimental numbers equal n ≥ 8. **c.** Body weight of *Pdgfra*$^{+/+}$ *Bbs8*$^{fl/fl}$ and *Pdgfra*$^{Cre/+}$ *Bbs8*$^{fl/fl}$ mice at a young (5-7 weeks) and older (>18 weeks) timepoint. Data are shown mean ± SD, with individual data points, p-values were determined via an unpaired t-test, experimental numbers equal n ≥ 11. **d, e.** WAT mass increase of **d.** gWAT and **e.** iWAT in *Pdgfra*$^{+/+}$ *Bbs8*$^{fl/fl}$ and *Pdgfra*$^{Cre/+}$ *Bbs8*$^{fl/fl}$ mice at a young (5-7 weeks) and older (>18 weeks) timepoint. Data are shown as ± SD, with individual data points; p-values were determined using a Two-way ANOVA with repeated measurements (mixed models). Post-hoc p-value correction for multiple testing was performed using Šidák adjustment, experimental numbers equal n ≥ 2. N.s. = non-significant.

3.4 Characterizing BBS8-dependent changes in APC subpopulations

3.4.1 Frequency of APC subpopulations

To understand how the loss of BBS8 affects the APC subpopulations, I performed high-dimensional flow cytometry experiments on cells isolated from the iWAT of lean *Bbs8*$^{+/+}$

and *Bbs8*$^{-/-}$ mice (6-9 weeks). I applied the gating strategy described above and compared the relative frequencies of the three subpopulations. The P1 subpopulation was significantly reduced in *Bbs8*$^{-/-}$ mice compared to *Bbs8*$^{+/+}$ mice (Fig. 13 a). In contrast, the P2 subpopulation was significantly increased, and the P3 subpopulation was slightly increased in the *Bbs8*$^{-/-}$ mice (Fig. 13 a). To evaluate if this change in subpopulation frequency could be attributed to the loss of BBS8 specifically in APCs, I used the conditional knockout line. Consistently, I observed a similar pattern of the distribution of the subpopulations. The P1 APCs were significantly downregulated in *Pdgfra*$^{cre/+}$ *Bbs8*$^{fl/fl}$ mice, whereas the P2 and P3 subpopulations showed a tendency to increase (Fig. 13 b). Thus, loss of BBS8 alters the balance of the APC subpopulations: the stem cell-like P1 population is diminished, while the committed P2 population expands, and the regulatory P3 subset exhibits a slight increase, indicating a shift in the cellular trajectory.

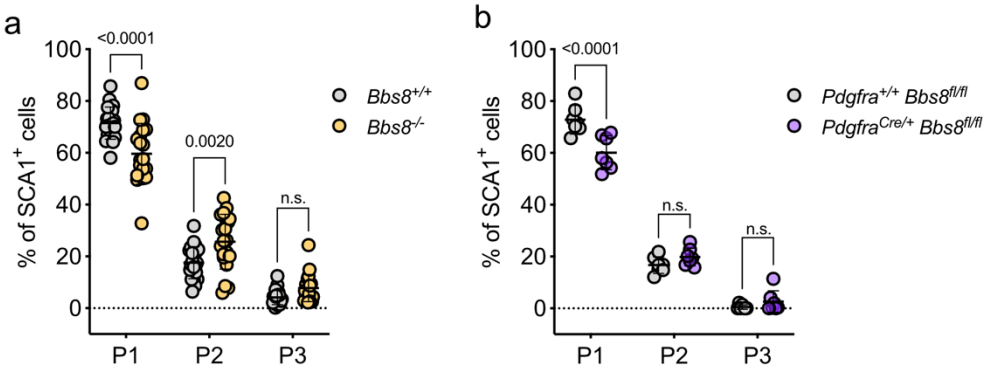

Fig. 13: Ciliary dysfunction results in changes in APC subpopulations. a. Frequencies of APC P1-P3 gated from the total APC pool (SCA1^{+}), isolated from *Bbs8*$^{+/+}$ (n = 23) and *Bbs8*$^{-/-}$ mice (n = 20) at 6-9 weeks (lean state). **b.** Frequencies of APC P1-P3 gated from the total APC pool (SCA1^{+}), isolated from *Pdgfra*$^{+/+}$ *Bbs8*$^{fl/fl}$ (n = 7) and *Pdgfra*$^{cre/+}$ *Bbs8*$^{fl/fl}$ mice (n = 7) at 6-7 weeks (lean state).

3.4.2 Transcriptomic analysis of APC progenitor populations in *Bbs8*$^{-/-}$ mice

To investigate the underlying molecular mechanism driving the shift in the frequency distribution of APC subpopulations in *Bbs8*$^{-/-}$ mice, I isolated P1-P3 subpopulations from lean *Bbs8*$^{-/-}$ and *Bbs8*$^{+/+}$ mice (7-8 weeks) using FACS and performed bulk RNA sequencing (RNA-seq). I applied principal component analysis (PCA) to the data set to visualize underlying patterns in the data (Fig. 14 a). The PCA revealed distinct clustering

between the subpopulations, as the first component (PC1) clustered P1 samples away from P2 and P3 (Fig. 14 a). Next, I confirmed the identity of the sorted subpopulations by analyzing marker gene expression. Regardless of the genotype, P1 cells highly expressed genes specific to the stem cell-like population, such as *Creb5* (*cAMP-responsive element binding-protein 5*), *Pi16* (*peptidase inhibitor 16*), and *Dpp4* (*dipeptidyl peptidase*) (Ferrero et al., 2020; Merrick et al., 2019; Schwalie et al., 2018) (Fig. 14 b). The committed P2 cells expressed genes related to adipogenic differentiation, such as *Pparg*, *Fasn* (*fatty-acid synthase*), and *Fabp4* (Fig. 14 b). However, these markers were also highly expressed in the P3, further supporting the similarity of P2 and P3 observed in the PCA. Nonetheless, P3 exhibited elevated expression of genes uniquely associated with this subpopulation, including *F3* (*coagulation factor* III), *Fmo2* (*flavin-containing dimethylaniline monooxygenase* 2), and *Rbp1* (*retinol-binding protein* 1)(Dong et al., 2022; Schwalie et al., 2018) (Fig. 14 b). All markers showed similar expression levels in *Bbs8*$^{-/-}$ and *Bbs8*$^{+/+}$ mice. Next, I analyzed the transcriptomic differences between *Bbs8*$^{-/-}$ and *Bbs8*$^{+/+}$ cells. When comparing the differently expressed genes (DEGs), the P1 populations showed the highest number of DEGs, while in P2 and P3 fewer genes were differently expressed between genotypes (Fig. 14 c). Of note, *Bbs8* (*Ttc8*) expression levels were comparable between the P1 and P2 subpopulations in wild-type mice, whereas P3 exhibited a lower *Bbs8* expression (Fig. S2). Thus, the loss of BBS8 may have a greater impact on the P1 and P2 subpopulations compared to P3 subpopulation, which is also reflected in the reduced number of DEGs between *Bbs8*$^{-/-}$ and *Bbs8*$^{+/+}$ P3 cells. Although DEG analysis revealed differences between *Bbs8*$^{-/-}$ and *Bbs8*$^{+/+}$ cells, this did not seem to be the driving force in segregating the PCs 1 and 2 as they segregated according to differences between subpopulations (Fig. 14 a). Thus, the impact of loss of BBS8 rather leads to subtle changes, which are lower in rank in segregating PCs. This may be because the changes upon loss of BBS8 are highly specific to each subpopulation rather than affecting all subpopulations in the same way, thereby not strongly influencing the principal component loadings. To test this hypothesis, I further analyzed the DEGs for each subpopulation individually.

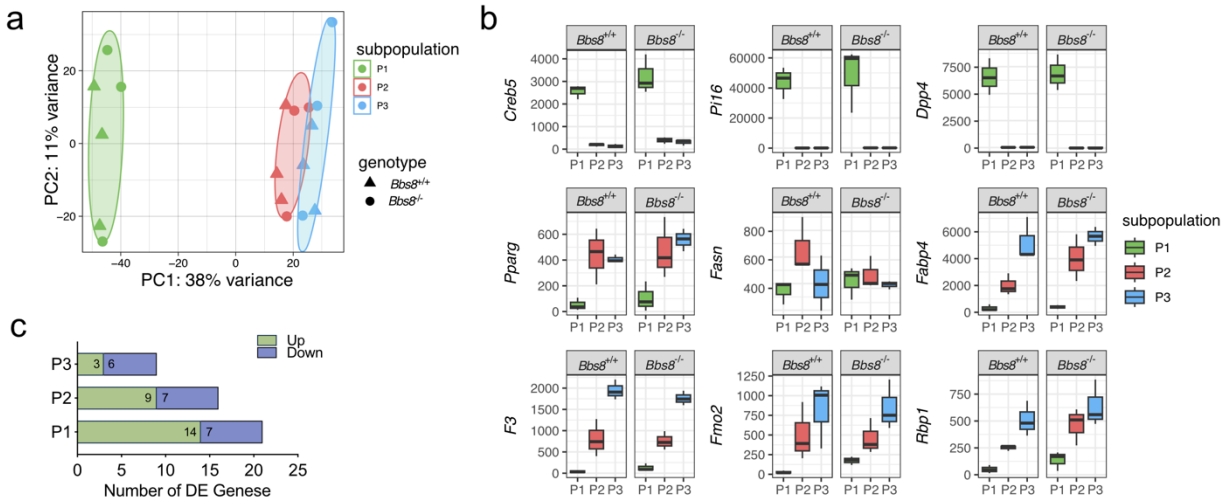

Fig. 14: Bulk Transcriptomic analysis of APC P1-P3 in *Bbs8*$^{-/-}$ mice. a. Principal Component Analysis (PCA) of the bulk RNA-seq data of FACS-sorted P1, P2, and P3 APCs isolated from *Bbs8*$^{+/+}$ and *Bbs8*$^{-/-}$ mice at 7-8 weeks (lean state) based on the 500 most variable genes. **b.** Expression level of published P1, P2, and P3 markers split per genotype. Data are shown as mean ± SD. **c.** Number of up (green) or down regulated (blue) differentially expressed (DE) genes of APC P1-P3 subpopulations in *Bbs8*$^{-/-}$ compared to *Bbs8*$^{+/+}$. The Benjamini-Hochberg method was used to calculate multiple testing adjusted p-values. Adapted from Sieckmann *et al.,* 2024 (bioxRiv).

First, I visualized DEGs for each subpopulation using volcano plots and then performed Gene ontology (GO) enrichment analysis of the DEGs for all three subpopulations. This revealed an upregulation of genes associated with extracellular matrix (ECM) remodeling in P1 cells from *Bbs8*$^{-/-}$ mice (Fig. 15 a-b). Several genes of the collagen family were upregulated (*Col1a1, Col3a1, Col4a1, Col4a2, Col5a3, Col6a3*), as well as fibroblasts-associated genes, such as *Bgn* (*biglycan*) and *Fosb* (*FBJ osteosarcoma oncogene*) (Fig. 15 a) (Dobrzanski et al., 1991; S. Hu et al., 2024). Accordingly, GO term analysis identified the enrichment of pathways involved in ECM structure organization and collagen-activated signaling (Fig. 15 b). In *Bbs8*$^{-/-}$ P2 cells, GO term enrichment analysis revealed an upregulation of processes related to nucleoside bisphosphate metabolism as well as acetyl-CoA metabolic processes (Fig. 15 d). These pathways have been previously reported to be essential during adipogenesis and to regulate adipose tissue expansion (Felix et al., 2021; Pinette et al., 2024). In line with the high adipogenic commitment of P2 cells, this suggests that loss of BBS8 further enhances their propensity towards adipogenic differentiation. Interestingly, the *Bbs8*$^{-/-}$ P2 cells were also enriched for pathways involved in tight junction assembly, suggesting a potential interaction with

epithelial cell within the WAT (Fig. 14 d). The P3 population had the lowest number of DEGs, however *TnC* (*Tenascin* C), which is expressed in the ECM of various tissues, was upregulated and pathways involving vascular associated smooth muscle cell proliferation were activated (Fig. 15 e-f). Similarly to the *Bbs8*$^{-/-}$ P1 cells, this suggests a shift towards a fibrogenic fate of these cells upon loss of BBS8. Still, DEGs proved to be quite different between the different subpopulations, suggesting that loss of BBS8 affects each subpopulation in a context-specific manner.

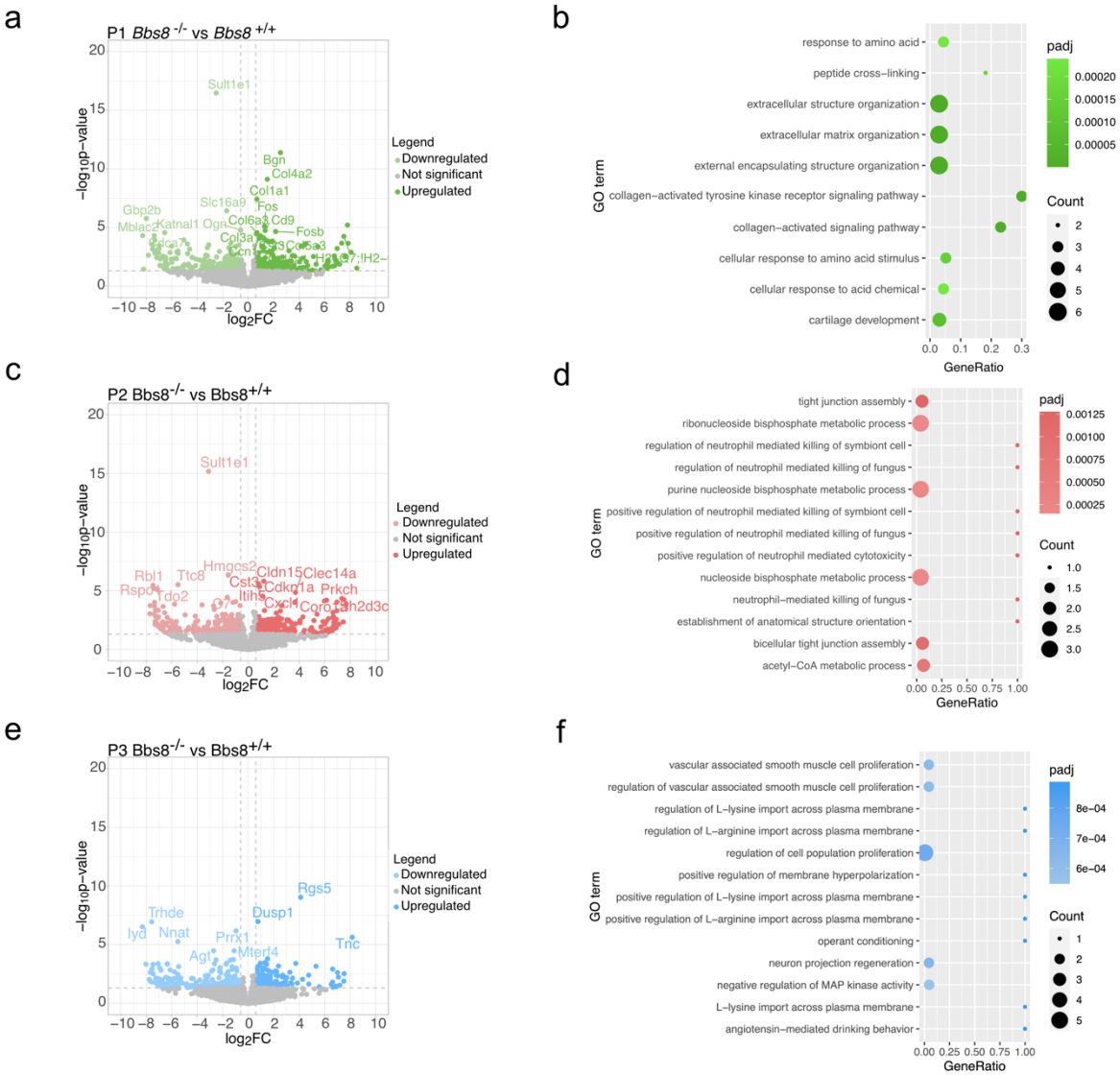

Fig. 15: Analysis of differentially regulated genes in *Bbs8*$^{-/-}$ APC subpopulations. a, c, f. Volcano plots depicting the up- and downregulated DEGs for **a.** P1, **c.** P2, and **e.** P3 APCs from *Bbs8*$^{-/-}$ and *Bbs8*$^{+/+}$ mice, isolated at 7-8 weeks (lean state). Genes names are written that have an adjusted p-value < 0.05. **b, d, f.** Over-representation analysis (ORA) of upregulated DEGs, highlighting the top biological processes from gene ontology (GO)

analysis in **b.** P1, **d.** P2, and **f.** P3 *Bbs8*$^{-/-}$ APCs compared to *Bbs8*$^{+/+}$ APCs. The color of the data points represents the adjusted p-values (color-scheme indicated) and the size of the data points represents the count of genes included for the indicated terms. Adapted from Sieckmann *et al.,* 2024 (bioxRiv).

I focused my analysis on the stem cell-like P1 APCs, as they (1) had the highest number of DEGs, suggesting a stronger influence of loss of BBS8, and (2) represent the starting pool from which the other APC populations arise (Merrick et al., 2019; Schwalie et al., 2018). First, I verified the increased expression of genes associated with ECM remodeling by qPCR (Fig. 16 a). I included collagens (*Col1a1*, *Col5a1*), the ECM glycoprotein *Fbn* (*fibronectin*), the cross-linking enzyme *Loxl2* (lysyl oxidase-like 2), and *Sparc* (*osteonectin*), as it modulates expression of several ECM genes (Bradshaw & Sage, 2001; López-Jiménez et al., 2017; To & Midwood, 2011). All genes were upregulated in *Bbs8*$^{-/-}$ P1 cells, although only *Fbn* and *Loxl2* were significantly upregulated (Fig. 16 a). To distinguish between cell-autonomous and systemic effects of loss of BBS8, I analyzed the fibrogenic gene expression in P1 cells sorted from *Pdgfra*$^{Cre/+}$ *Bbs8*$^{fl/fl}$ mice (Fig. 16 a). Here I also observed an increase in gene expression of genes related to ECM remodeling, demonstrating that the fibrogenic shift in *Pdgfra*-expressing cells is regulated in a cell-autonomous manner.

Next, I performed whole-mount labeling to further analyze ECM remodeling at protein level and to assess the consequence of the fibrogenic shift of P1 cells in a tissue context. I labelled against FBN, as this protein forms fibrillar architectures together with collagens during ECM formation (Paten et al., 2019). Whole-mount labeling demonstrated a substantial increase of FBN in iWAT of lean *Bbs8*$^{-/-}$ mice compared to *Bbs8*$^{+/+}$ mice (Fig. 16 c). FBN was observed in the extracellular environment but co-labeling against PDGFRα revealed that these cells were also expressing FBN. This further underlines the role of *Pdgfra*-expressing cells in mediating the fibrogenic shift upon loss of BBS8.

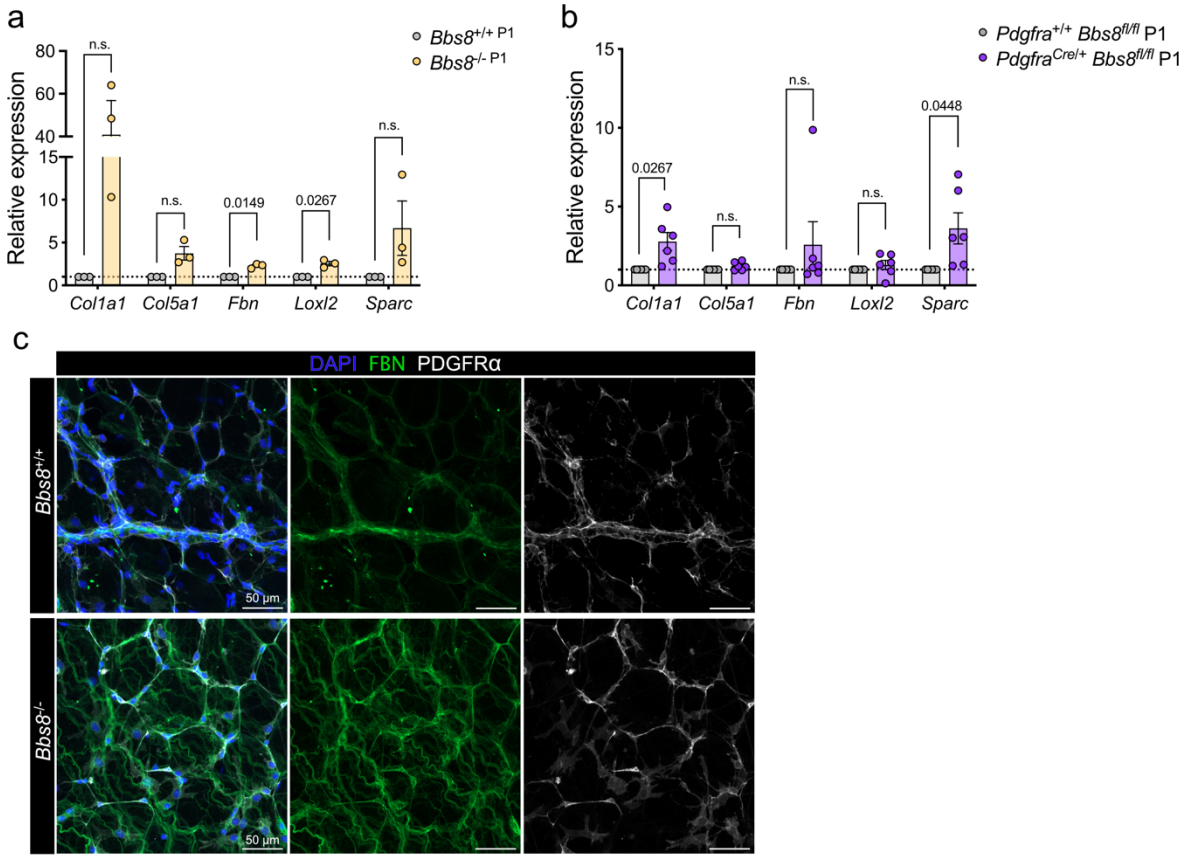

Fig. 16: Loss of BBS8 leads to remodeling of gene and protein expression in P1 APCs. a. Relative mRNA expression of fibrosis marker of sorted P1 APCs isolated from *Bbs8*$^{+/+}$ and *Bbs8*$^{-/-}$ mice (n = 3) at 7 weeks (lean state) assessed by qRT-PCR. mRNA expression was normalized to *Bbs8*$^{+/+}$. **b.** Relative mRNA expression of fibrosis marker of sorted P1 APCs isolated from *Pdgfra*$^{+/+}$ *Bbs8*$^{fl/fl}$ and *Pdgfra*$^{cre/+}$ *Bbs8*$^{fl/fl}$ mice mice (n = 6) at 5-6 weeks (lean state) assessed by qRT-PCR. mRNA expression was normalized to *Pdgfra*$^{+/+}$ *Bbs8*$^{fl/fl}$. Data are shown as ± SD, with individual data points; p-values were determined using a one-sample t-test against a theoretical mean of one. **c.** Whole mount staining of iWAT of 7-week-old *Bbs8*$^{+/+}$ and *Bbs8*$^{-/-}$ mice. Stained with DAPI (nuclei, blue), FBN (Fibronectin; extra-cellular matrix, green), and PDGFRα (APC marker, white). Scale bar is indicated. n.s. = non-significant. Adapted from Sieckmann *et al.,* 2024 (bioxRiv).

To conclude, loss of BBS8 leads to a remodeling of the APC compartment, reducing the pool of stem cell-like P1 cells as these cells shift towards a fibrogenic phenotype, while P2 and P3 cells increase. Similar findings in the conditional *Bbs8* knockout model and whole-mount labeling underline the contribution of *Pdgfra*-expressing progenitor cells in fibrotic remodeling of lean WAT in *Bbs8*$^{-/-}$ mice.

3.4.3 Characterization of the profibrogenic CD9^{high} populations in *Bbs8*$^{-/-}$ mice

Fibrotic remodeling of WAT has already been described as a consequence of obesity (Divoux et al., 2010; K. Sun et al., 2023). Recently, a distinct population of *Pdgfra*-expressing cells was identified to drive adipose tissue fibrosis in obesity (Marcelin et al., 2017). These profibrogenic cells were identified based on high expression of CD9 (Tetraspanin-29) (Marcelin et al., 2017). The CD9^{high} expressing cells exist in iWAT and gWAT, however, the profibrogenic capacity of these cells was significantly higher in cells originating from the gWAT (J. H. Lee et al., 2022). Since the *Bbs8*$^{-/-}$ mice are lean but still exhibit fibrogenic remodeling of the WAT, I aimed to determine whether this is also due to a shift to CD9^{high} cells. To this end, I analyzed APCs isolated from the gWAT of lean *Bbs8*$^{-/-}$ mice and compared them to wild-type littermates using flow cytometry. I gated for CD9 expression on Lin^{-}PDGFRα^{+} cells (Fig. 17 a) and analyzed frequency and median fluorescence intensity (MFI) (Fig. 17 b). A significant increase in the frequency of the CD9^{high} population was observed in *Bbs8*$^{-/-}$ mice compared to *Bbs8*$^{+/+}$ mice (Fig. 17 c) that was also represented in an increase of the MFI of CD9 in PDGFRα^{+} cells in the *Bbs8*$^{-/-}$ mice (Fig. 17 d), demonstrating that loss of BBS8 induces a fibrogenic fate change in APCs already in the lean state. The CD9^{high} cell population seems to be distinct from the stem cell-like P1 population (J. H. Lee et al., 2022; Marcelin et al., 2017), but shares the surface marker CD54 with P2 cells (J. H. Lee et al., 2022). Thus, the shift in frequency of subpopulations in the *Bbs8*$^{-/-}$ mice could be explained by P1 cells undergoing a fate change and becoming CD9^{high} cells, which might have been masked as an increase in P2 cells in my previous flow cytometry panel.

I performed whole mount labeling next to analyze the CD9 expression in a spatial context. I co-labeled against PDGFRα to distinguish APCs as macrophages also express CD9 in the adipose tissue (Hill et al., 2018). I observed a distinct increase in CD9 expression in PDGFRα^{+} cells in the WAT of *Bbs8*$^{-/-}$ mice compared to *Bbs8*$^{+/+}$ mice (Fig. 17 e), further underlining their increased presence upon loss of BBS8. The CD9^{+} cells were intercalated between mature adipocytes (Fig. 17 e), where also committed P2 cells were found (Merrick et al., 2019).

It has already been shown that the fibrogenic switch to CD9^{high} cells during obesity diminishes their adipogenic potential and that this cell population has a lower expression of adipogenic genes (J. H. Lee et al., 2022; Marcelin et al., 2017). To further characterize the CD9^{high} cells of *Bbs8*$^{-/-}$ mice and to analyze if the fate shift affects their function, I sorted the cells and performed an *in vitro* adipogenesis assay using the minimal induction cocktail either in the presence or absence of TUG-891 to analyze if the cells respond to cilia-specific adipogenic cues (Fig. 17 f). However, the CD9^{high} cells of *Bbs8*$^{-/-}$ showed a low adipogenic potential and did not respond to TUG-891 stimulation (Fig. 17 g). Thus, loss of BBS8 leads to an expansion of the anti-adipogenic and profibrogenic CD9^{high} population, independent of obesity as a driving factor.

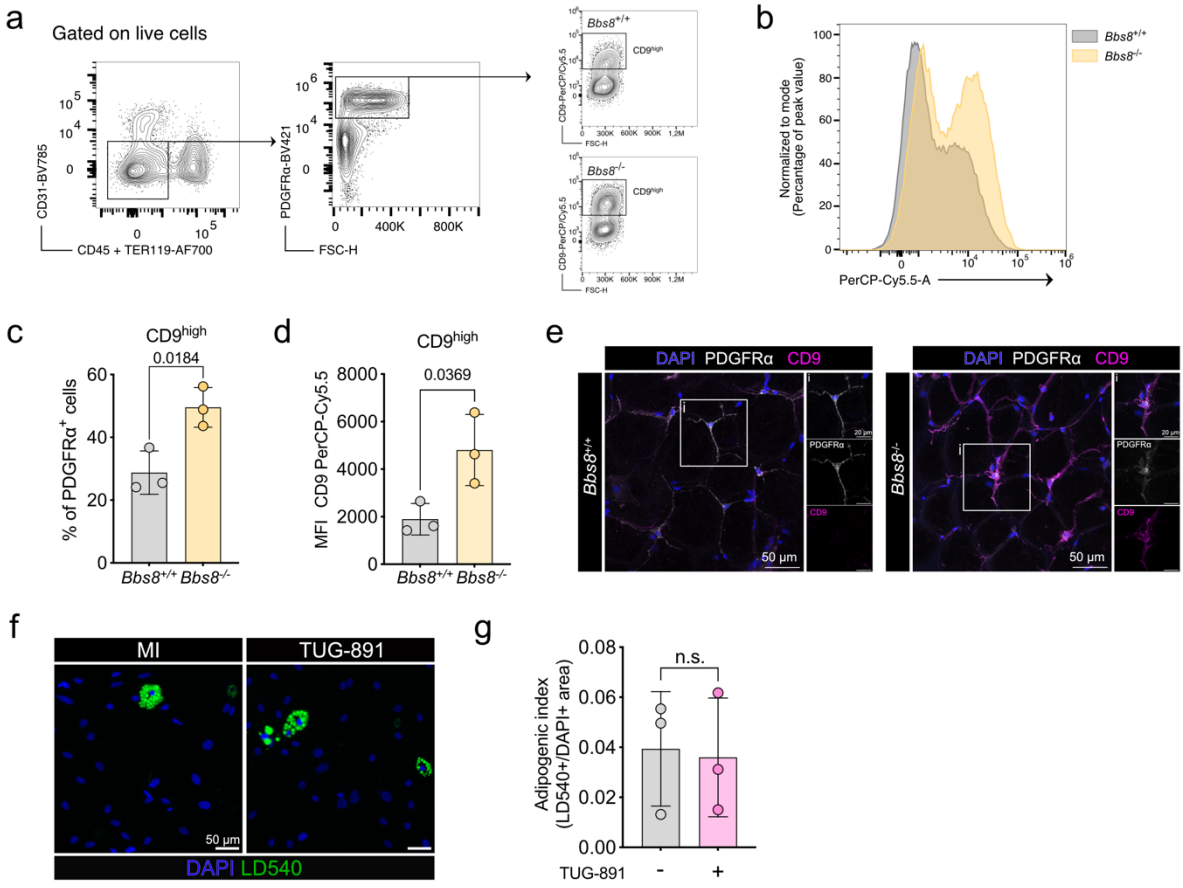

Fig. 17: Characterizing the CD9^{hi} APC subpopulation in gWAT of lean *Bbs8*$^{-/-}$ mice. **a.** Gating strategy for CD9^{hi} APCs in the gWAT stromal vascular fraction. **b.** Histogram showing CD9-PerCP-Cy5.5 signal from concatenated *Bbs8*$^{+/+}$and *Bbs8*$^{-/-}$ files **c.** Quantification of CD9^{high} cell surface expression on PDGFRa^{+} cells from *Bbs8*$^{+/+}$ and *Bbs8*$^{-/-}$ mice at 5 weeks (lean state). **d.** Median Fluorescent Intensity (MFI) of CD9-PerCP-Cy5.5 signal of PDGFRa^{+} cells from *Bbs8*$^{+/+}$ and *Bbs8*$^{-/-}$ mice. **e.** Whole mount staining of iWAT from *Bbs8*$^{+/+}$ and *Bbs8*$^{-/-}$ mice at 7 weeks (lean state). Stained with DAPI (nuclei,

blue), PDGFRα (APC marker, white), and CD9 (magenta). Scale bars are indicated. **f.** Exemplary fluorescence images of FACS-sorted, *in-vitro* differentiated gWAT PDGFRa^{+}CD9^{hi} *Bbs8*$^{-/-}$ cells from mice at 7 weeks (lean state). Cells were differentiated for 8 days using the minimal induction (MI) with and without TUG-891 (100 µM). Cells were stained with DAPI (nuclei, blue) and LD540 (lipid droplets, green). Scale bar is indicated. **g.** Quantification of the adipogenic index from CD9^{hi} *Bbs8*$^{-/-}$ cells depicted in **f.** Each data point represents the mean of all images from n = 3 mice in total. All data are represented as mean ± SD, p-values were determined using an unpaired Student's t-test.

3.4.4 Lipid metabolism of P1 APCs

My results showed that the P1 population is diminished, while the anti-adipogenic CD9^{high} cell pool is increased in *Bbs8*$^{-/-}$ mice. However, *Bbs8*$^{-/-}$ mice develop obesity over time, accompanied by an increase in adipose tissue weight. Therefore, I investigated whether lipid synthesis capacity is intrinsically altered in *Bbs8*$^{-/-}$ APCs. To this end, I isolated P1 APCs from lean *Bbs8*$^{-/-}$ and *Bbs8*$^{+/+}$ mice using MACS, followed by *in vitro* culture and differentiation. To assess lipid uptake rather than intrinsic differentiation capability, I used the full induction cocktail containing rosiglitazone for three days. To enable lipid tracing, I fed the cells alkyne-labeled fatty acids at four different time points (24 h, 8 h, 4 h, 0 h) over the course of one day (Fig. 18 a). Cells metabolize the alkyne-labeled fatty acids and incorporate the label into newly synthesized lipids (Kuerschner & Thiele, 2022). With a click reaction using azido reporter, the alkyne-labeled lipids can be analyzed via mass spectrometry to trace fatty acid incorporation in different lipid classes (Fig. 18 a).

First, I analyzed the total lipidome of the cells at the first tracing time point (24 h) and at the last tracing time point (0 h) (Fig. 18 d). The dominant lipid species at all time points were triacyl glycerides (TAG) as this is the major energy storage form of adipocytes (Ahmadian et al., 2007). This was similar between *Bbs8*$^{-/-}$ and *Bbs8*$^{+/+}$ cells, although *Bbs8*$^{-/-}$ cells showed a slight increase in TAGs (80.45 ± 4.58 %) at the early time point (24 h) compared to *Bbs8*$^{+/+}$ cells (70 ± 12.37 %) (Fig. 18 d).

Phosphatidylcholine (PC) is present in all mammalian cells and is a major constituent of cell membranes, thus, I analyzed PC content at all tracing time points as a proxy for assessing cell growth (Fig. 18 d). The PC content *Bbs8*$^{-/-}$ cells and *Bbs8*$^{+/+}$ cells slightly increased over time, indicating steady cell growth or an increase in cell size due to uptake of lipids (Fig. 18 e). No difference between genotypes was observed.

The total TAG content also increased over time, indicating an increase in lipid uptake and or synthesis as the cells matured into adipocytes (Fig. 18 f). Here, *Bbs8*$^{-/-}$ cells showed a higher total TAG content at all time points, however there was a high spread in the data, indicated by a high standard deviation (Fig. 18 f). To account for differences in cell growth, I calculated the ratio of TAG to PC content at the last chase point (0 h). To compare between genotypes, I normalized the ratio of TAG to PC from *Bbs8*$^{-/-}$ cells to *Bbs8*$^{+/+}$ cells. My results revealed that the synthesis of TAGs is increased in *Bbs8*$^{-/-}$ cells (Fig. 18 f). Although cells were taken from mice at a lean time point, the progenitor cells might be primed to meet the demand of an increased energy uptake in *Bbs8*$^{-/-}$ mice.

In parallel to the lipid tracing experiment, I also analyzed the cells in an *in vitro* adipogenesis assay (Fig. 18 b-c). For both genotypes, a strong increase of the adipogenic index was observed (Fig. 18 c).

Taken together, the enhanced lipid uptake and TAG synthesis capacity of *Bbs8*$^{-/-}$ cells may underlie the hypertrophy phenotype observed in the WAT of obese *Bbs8*$^{-/-}$ animals.

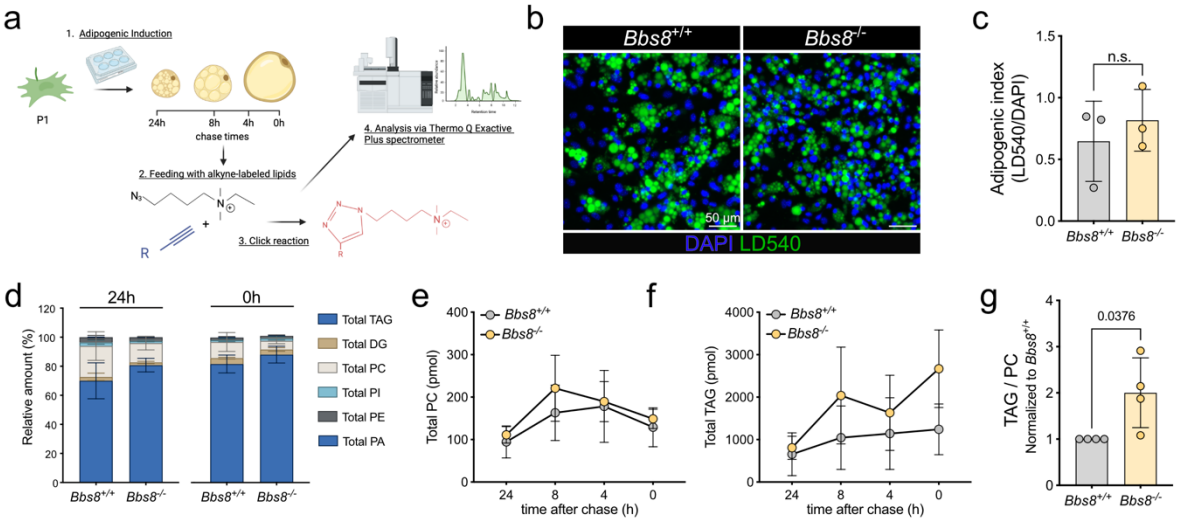

Fig. 18: Analysis of lipid uptake in differentiated P1 APCs form *Bbs8*$^{-/-}$ mice. a. Schematic of the experimental set-up to measure lipid uptake in a pulse-chase experiment. **b.** Exemplary fluorescence images of MACS-sorted, *in-vitro* differentiated P1 APCs isolated from *Bbs8*$^{+/+}$ and *Bbs8*$^{-/-}$ cells mice at 7 weeks (lean state). Cells were stained with DAPI (nuclei, blue) and LD540 (lipid droplets, green). Scale bars are indicated. **c.** Quantification of the adipogenic index from *Bbs8*$^{+/-}$ and *Bbs8b*$^{-/-}$ P1 cells depicted in **b.** Each data point represents the mean of all images from n = 3 mice in total. **d-g.** Lipidomics data of P1 cells from *Bbs8*$^{+/+}$ and *Bbs8*$^{-/-}$ mice, isolated at 6 – 7 weeks (lean state) after 4 days of *in-vitro* differentiation. **d.** Relative amount of the different lipid

classes of the total lipid content measured at the earliest (24h) and latest (0h) chase timepoint. **e-f.** Total amount of **e.** phosphatidylcholine (PC) and **f.** triacyl glycerides (TAG) measured over the course of the four different chase times. Data are shown as mean ± SD. **g.** Uptake of TAG with respect to PC at timepoint 0 h. Data is normalized to *Bbs8*$^{+/+}$. Each data point represents one mouse from n = 4 mice in total. All data are represented as mean ± SD, with individual data point; p-values were determined using an unpaired Student's t-test. PI = Phosphatidylinositol; PE = phosphatidylethanolamine; PA = phosphatidate.

3.5 Single-cell analysis of lean iWAT of *Bbs8*$^{-/-}$ mice

3.5.1. Annotation and trajectory analysis of cell clusters identified by single-cell analysis

To analyze the change towards a fibrogenic cell fate in more detail, I performed single-cell RNA-sequencing (scRNA-seq) on the stromal vascular fraction (SVF) of iWAT from lean *Bbs8*$^{+/+}$ and *Bbs8*$^{-/-}$ mice (Fig. 19 a). No prior sorting of cells was performed to (1) avoid introducing bias through a pre-enrichment strategy and (2) minimize information loss of potential cellular crosstalk. The SVF comprised various cell types, including APCs, immune cells, and vascular cells. Therefore, my first aim was to generate a comprehensive atlas of all cell types present in my data set. The analysis of the scRNA-seq data set was performed in cooperation with Dr. Lisa Steinheuer from the group of Kevin Thurley. For an unbiased initial visualization of the data, we performed Uniform Manifold Approximation and Projection (UMAP) for dimensionality reduction on the integrated scRNA-seq data set from *Bbs8*$^{+/+}$ and *Bbs8*$^{-/-}$ SVF (Fig. 19 b). Unsupervised clustering of the gene expression profiles identified 13 cell types (Fig. 19 a). To identify cell types, I examined the top five marker genes for each cell cluster and analyzed the expression of known marker genes (Fig. S2 a-b). I identified innate immune cells, including monocytes, macrophages, and dendritic cells, as well as immune cells of the adaptive immune system, including T-cells and B-cells (Fig. S2 a). Within the vascular niche, I identified endothelial cells and pericytes (Fig. S2 b). A smaller cluster exhibited high expression of cell cycle-related genes and was therefore annotated as mitotic-cell cycle (Fig. S2 b). All three APC subpopulations were present in my dataset, characterized by the expression of specific marker genes: *Dpp4* and Pi16 (for P1), *Col15a1* (*collagen* 15a1) (for P2), and *Mmp3* (*matrix metalloprotease 3*) and *Bgn* (for P3) (Fig. 19 e-f) (Merrick et al., 2019; Schwalie et al., 2018). Furthermore, I observed another cell

population which clustered close to the APC subpopulations, indicating a mesenchymal origin (Fig. 19 b, e). Based on marker gene expression and Reactome analysis of upregulated genes, I annotated this cluster as fibrogenic precursor cells (FPCs) (Fig. 19 c; Fig. S2 c). The FPCs shared some defining markers with the other APC clusters, pointing to the high plasticity of mesenchymal cells and a heterogenous nature of fibrogenic cells (C. Li & Wang, 2022). However, they lacked expression of defining markers for progenitor cells or adipogenic markers, suggesting that they might represent a population like $CD9^{high}$ cells described by flow cytometry (Fig. 19 g). To analyze genotype-specific differences, we down-sampled the APC P1-P3 and FPC cell populations and compared their abundance (Fig. 19 h). This revealed an increase in the FPCs in *Bbs8*$^{-/-}$ mice (Fig. 19 h), supporting the notion that the FPC cluster represents a fibrogenic population similar to $CD9^{high}$ APCs.

APCs constantly undergo dynamic changes in response to various environmental stimuli and during differentiation. These responses are reflected in the cell's molecular profile and can be inferred from its transcriptomic data to reconstruct a dynamic cellular trajectory with respect to differentiation or cell cycle progression (Hwang et al., 2018). Thus, to investigate the cell-fate changes at the single-cell level, we performed trajectory inference on the P1-P3 APC subpopulations and the FPCs using Monocle3 (Fig. 19 h). In line with previous data from Merrick et al., the pseudo-temporal analysis predicted that the P1 progenitor cells develop into either P2 or P3 APCs in wild-type mice, while FPCs developed from P2 cells (Fig. 19 h) (Merrick et al., 2019). In contrast, for *Bbs8*$^{-/-}$ P1 cells, a different trajectory was observed: the cells predominantly developed into FPCs and only subsequently into P2 cells (Fig. 19 h). In conclusion, the scRNAseq data further supports the notion that loss of BBS8 alters the balance of the subpopulations in WAT by demonstrating that APC P1 cells give rise to a fibrogenic cell population in lean *Bbs8*$^{-/-}$ mice.

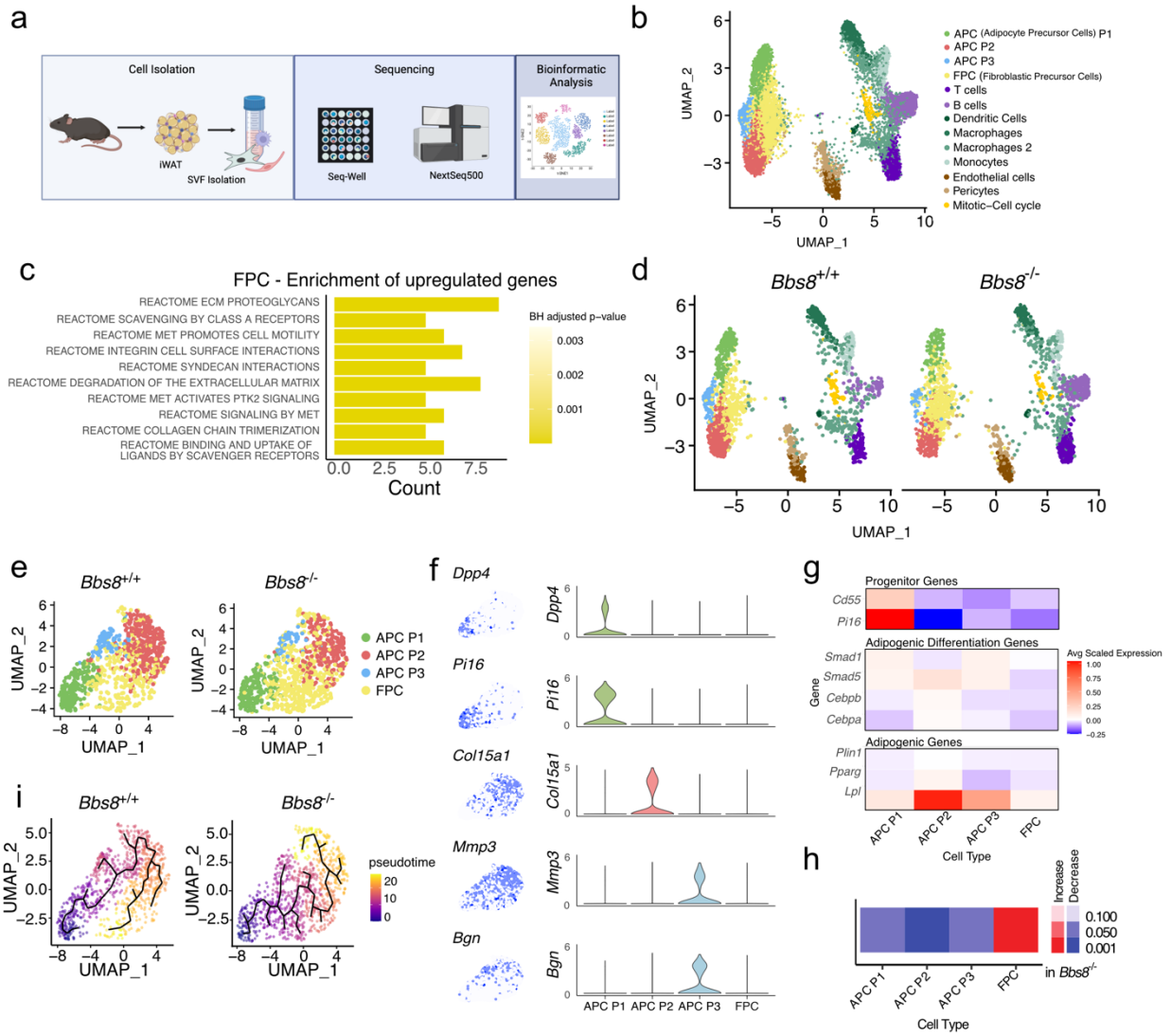

Fig. 19: Single-cell analysis of iWAT from lean *Bbs8*$^{-/-}$ mice. a. Scheme of sample processing for single-cell RNA sequencing (scRNA-seq). **b.** Annotation and UMAP plot analysis from scRNA-seq data on iWAT SVF from lean *Bbs8*$^{+/+}$ (7 weeks) and *Bbs8*$^{-/-}$ (8 weeks) mice describing several distinct cell clusters of the iWAT. **c.** Relative cell numbers in each cluster per genotype. Cell numbers have been normalized to total cell number per cluster. **d.** UMAP plot of iWAT SVF from *Bbs8*$^{+/+}$ and *Bbs8*$^{-/-}$ mice split per genotype. **e.** Subsetted UMAP plot of the P1-P3 APCs and FPC cluster in *Bbs8*$^{+/+}$ and *Bbs8*$^{-/-}$ mice. **f.** P1, P2, and P3 marker expression overlayed over the subsetted UMAP displayed in **e**. (left). Violin plots of published P1, P2, and P3 markers in APCs and FPCs (right). **g.** Heat-map depicting gene expression of APCs and FPC for different progenitor and adipogenic genes across all samples. **h.** Differential abundance analysis of down-sampled clusters in *Bbs8*$^{-/-}$ compared to *Bbs8*$^{+/+}$ mice, the color-code shows FDR-corrected p-values. **i.** *In-silico* pseudo-time analysis of the P1-P3 APCs and FPCs along differentiation trajectories using Monocle3 overlayed over the subsetted UMAP displayed in **a**. Adapted from Sieckmann *et al.,* 2024 (bioxRiv).

3.5.2 Interaction analysis of mesenchymal cells and the vascular niche

A shift in cellular trajectory can influence the local environment and alter cell communication within the tissue niche. Conversely, changes in cell communication within the niche may affect the local environment, and, in turn, the cellular trajectory. APCs interact with different cell types in the WAT (Cardoso et al., 2021; Hildreth et al., 2021; H. Wang et al., 2024), which is controlled by the distinct localization of APCs. Here, the perivascular niche where committed APCs reside along the blood vessels is of particular interest as it promotes adipogenesis (Gupta et al., 2012; Hilgendorf et al., 2019; W. Tang et al., 2008; Tran et al., 2012). To investigate whether loss of BBS8 and the resulting change in cell fate also alters cellular communication within the tissue, I joined forces with Dr. Geza Schermann from the group of Carmen Ruiz de Almódovar. We performed CellChat analysis to the different APC populations, the FPCs, pericytes, and endothelial cells from *Bbs8*$^{+/+}$ and *Bbs8*$^{-/-}$ mice (Fig. 20 a). CellChat predicts potential cell-cell interactions based on its curated database of ligand-receptor interactions (Jin et al., 2021). This revealed a complex interaction network between the different cell types, with the three APC populations showing the strongest interaction with endothelial cells (Fig. 20 a). Since committed P2 cells are known to be in close contact with endothelial cells, we focused on this population and identified a specialized subcluster with the strongest interaction potential towards endothelial cells (Fig. 20 b-c). This cluster, termed APC P2_1, was characterized by high expression of collagen- and laminin-associated ligands compared to other APC subpopulations (Fig. 20 d). These molecules have been shown to promote angiogenesis and, thereby, vascular remodeling (McCoy et al., 2018; Senk & Djonov, 2021; Stamati et al., 2014). Strikingly, the collagen- and laminin-mediated interaction pathways were significantly upregulated in cells from *Bbs8*$^{-/-}$ mice (Fig. 20 e). Thus, the increase of fibrogenic gene expression upon loss of BBS8 might also influence other APC populations, namely the newly identified APC P2_1 cells, altering their interaction with endothelial cells. In this case, increased expression of fibrogenic genes could promote vascularization, potentially preparing the tissue for expansion. In context of the previous data, loss of BBS8 alters the cellular trajectory by shifting P1 cells towards a fibrogenic phenotype, which impacts the entire WAT, as indicated by an increased fibronectin and altered cell communication with endothelial cells.

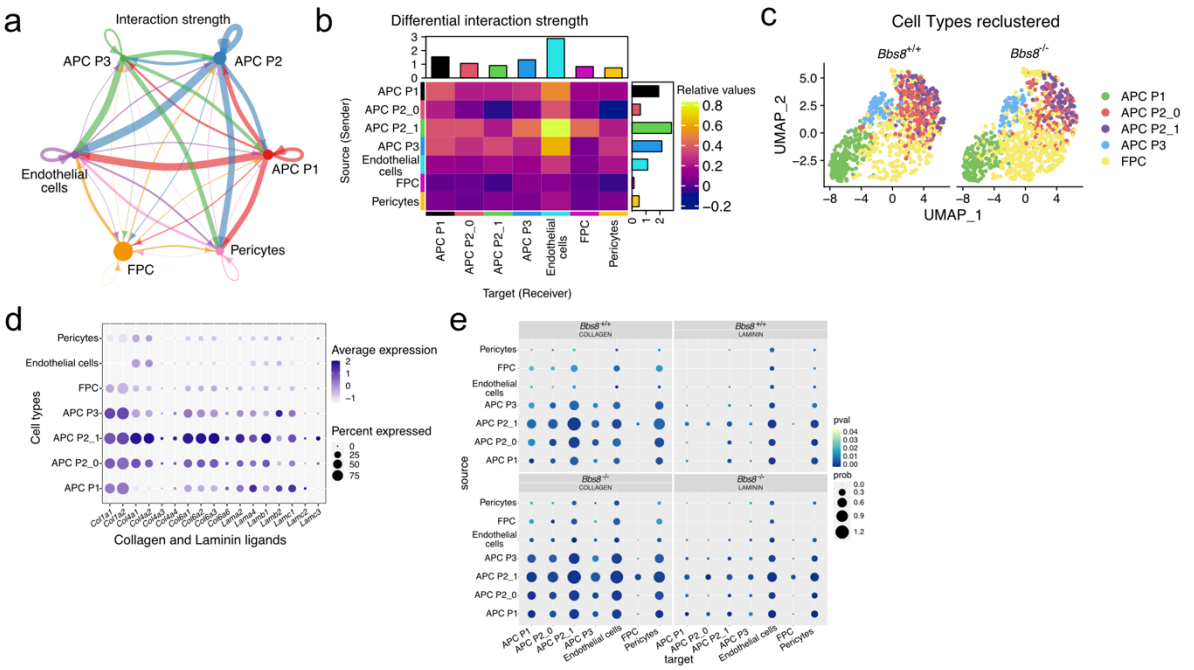

Fig. 20: Analysis of interaction between APCs, FPC and endothelial cells. a. Circos plots depicting the interaction strength between endothelial cells, pericytes, APC P1-P3, and FPCs as determined via the CellChat pipeline. **b.** Heat map depicting the differential interaction strength of the endothelial cells, pericytes, APC P1-P3, and FPCs. The color scheme represents the strength of the interaction. c. UMAP plot of the APCs, including the new defined APC P2_0 and P2_1, and FPC cluster in *Bbs8*$^{+/+}$ and *Bbs8*$^{-/-}$ mice. **d.** Dot plot showing the expression of collagen and laminin genes in the endothelial cells, pericytes, APC P1-P3, and FPCs. The average gene expression is color-coded, the percentage of expression is expressed by the size of the dot. **e.** Dot plot of the collagen and laminin pathways in *Bbs8*$^{+/+}$ and *Bbs8*$^{-/-}$ cells. The p-value is color-coded, the probability of expression is expressed by the size of the dot. Adapted from Sieckmann *et al.,* 2024 (bioxRiv).

3.6 Analyzing Hedgehog signaling in APCs

The Hh pathway is one of the most well characterized signaling pathways in primary cilia. It is evolutionarily conserved and controls tissue development and homeostasis. In mesenchymal cells, Hh signaling controls proliferation, differentiation, and stem cell maintenance (Kopinke et al., 2017; Takebe et al., 2015; Wu et al., 2024). Thus, I hypothesized that changes in Hh signaling may underlie the fate change in *Bbs8*$^{-/-}$ APCs. To test this, I first established read-outs to analyze Hh signaling in APCs.

3.6.1 Analyzing ciliary localization of Hh components

To investigate Hh signaling in APCs, I employed the immortalized 3T3-L1 cell line, as well as primary APCs (SVF Lin-) isolated from iWAT of lean wild-type mice. The cells were treated with SMO agonist N-Methyl-N′-(3-pyridinylbenzyl)-N′-(3-chlorobenzo[b]thiophene-2-carbonyl)-1,4-diaminocyclohexane (SAG, 1 µM) for 24 h after serum starvation. Subsequently, the localization of SMO and GPR161 was analyzed by immunocytochemistry. Upon SAG stimulation, the GPCR SMO translocated into the cilium (Fig. 21 a-b). In contrast, GPR161, an orphan GPCR that is present in the cilium in a ligand-free state, exited the cilium upon Hh activation (Fig. 21 a, c). To quantify these changes, I used CiliaQ (Hansen et al., 2021) and analyzed the parameters average immunofluorescence intensity and average immunofluorescent intensity of the 10 % highest voxels of SMO or GPR161 in the cilium (Fig. 21 d-e). Each parameter is susceptible to different detection biases: the average ciliary intensity reflects all voxels in the ciliary mask is, therefore, sensitive to variation and less reliable. The intensity of the 10 % highest voxels depends on a uniform ciliary intensity distribution and takes only the brightest voxels into account. This parameter is, therefore, less error-prone due to a low signal-to-noise ratio (Hansen et al., 2021).

Both parameters reliably quantified SMO localization upon SAG stimulation in 3T3-L1 and SVF Lin- cells (Fig. 21 d). SMO intensity significantly increased upon SAG treatment in both cell types. However, 3T3-L1 cells exhibited higher basal SMO levels (10142 ± 8268 10 % highest voxel; 5329 ± 3843 average intensity) compared to SVF Lin- cells (1217 ± 535.4 10 % highest voxel; 466.7 ± 217.9 average intensity) (Fig. 21 d). Immortalization of a cell line typically involves alteration in pathways that control cell proliferation and survival (Liu et al., 2021). Therefore, cell lines may differ from the *in vivo* situation (Pan et al., 2009). Quantifying GPR161 localization showed that in both cell models, GPR161 localization to the cilium was reduced upon SAG treatment (Fig. 21 e). However, in SVF Lin- cells, SAG treatment decreased GPR161 localization more strongly (53.2 % decrease in 10 % highest voxel; 60.5 % decrease in average intensity) compared to 3T3-L1 cells (16.6 % decrease in 10 % highest voxel; 20.8 % decrease in average intensity) (Fig. 21 e). Nevertheless, both cell lines exhibited consistent response to SAG

treatment, shown by increased SMO localization and decreased GPR161 localization in the primary cilium.

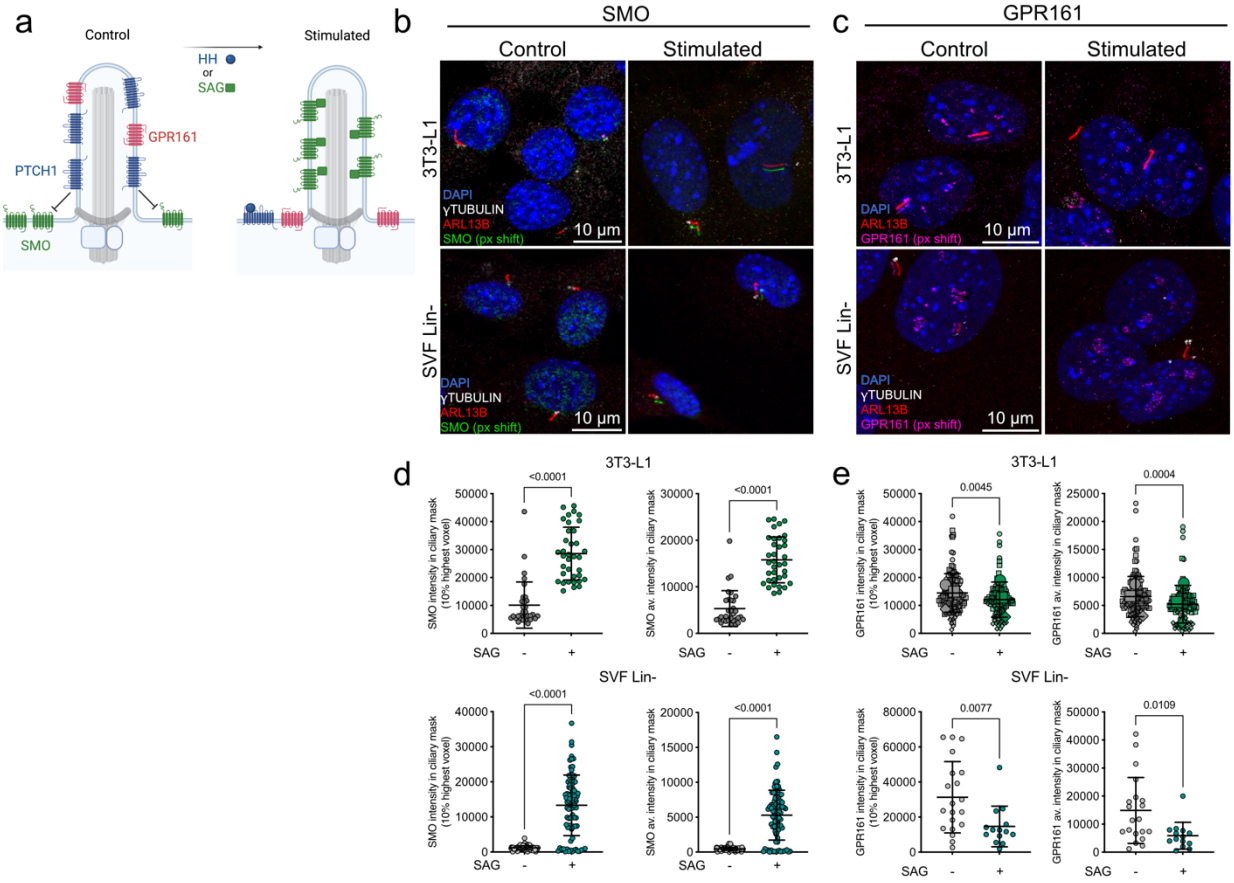

Fig. 21: Analyzing ciliary Hedgehog signaling using the subcellular localization of Smoothened (SMO) and GPR161. a. Scheme depicting the receptor distribution of Patched1 (PTCH1), Smoothened (SMO), and GPR161 at the ciliary membrane in control and stimulated conditions. **b,c.** Representative images of ciliated 3T3-L1 and SVF Lin- cells under Hedgehog control and stimulated (+ 1 µM SAG) conditions. Cells have been labeled with DAPI (DNA, blue), an anti-γTUBULIN antibody (white), an anti-ARL13B antibody (red), and either with a **b.** anti-SMO antibody (green) or **c.** with an anti-GPR161 antibody (magenta). The green (**b.**) or magenta (**c.**) channel have been shifted by 5 pixels in each image, respectively. Scale bars are indicated. **d.** Quantification of SMO intensity parameters in 3T3-L1 and SVF Lin- cells after 24 h stimulation with 1 µM SAG. **e.** Quantification of GPR161 intensity parameters in 3T3-L1 and SVF Lin- cells after 24 h stimulation with 1 µM SAG. In 3T3-L1 cell three different secondary antibodies have been used for GPR161 detection, the three different n are indicated by different shapes and the mean of each data set is indicated by the larger data points. As datasets were not normally distributed, statistical differences were calculated using a Mann-Whitney test, p-values are indicated. As the datasets were not normality distributed, statistical differences were calculated using a Kruskal-Wallis test and Dunn´s multiple comparison posthoc test, p-values are indicated. Each data point represents a single primary cilium.

3.6.2 Analyzing proteolytic processing of GLI1 and GLI3 upon Hedgehog activation

The Hh pathway regulates downstream signaling through transcriptional mediation and proteolytic processing of GLI transcription factors. In the absence of Hh ligands, the transcription factor GLI3 is proteolytically cleaved from its full-length form (GLI3FL) to a smaller repressor form (GLI3R), which re-locates to the nucleus, repressing Hh-dependent gene expression (Fig. 22 a) (Chaudhry et al., 2017; B. Wang et al., 2000). Activation of Hh signaling inhibits GLI3 processing and instead favors the activator state of other GLI proteins. GLI1 induces Hh-dependent gene expression and serves as a reliable biomarker of pathway activation (Doheny et al., 2020). To study Hh activation, I analyzed the proteolytic processing of GLI transcription factor as another read-out. 3T3-L1 cells were treated with SAG (100 nM) for 24 h after starvation and processed for Western Blot analysis (Fig. 22 b, d). SAG stimulation induced GLI1 protein expression (Fig. 22 d, e) and diminished GLI3 processing into its repressor form (GLI3R) (Fig. 22 b, c). Of note, I was not able to detect the full-length version of GLI3 with Western Blot. This may be due to low protein levels of the activator form in the protein lysate. A critical balance between GLI3R and GLI3FL determines the appropriate transcriptional response to Hh (Chaudhry et al., 2017). However, studies have shown that GLI3FL is dispensable in certain tissues, whereas the repressor form is essential (Brun et al., 2022; Wiegering et al., 2019). Thus, GLI3FL may play a lesser role in Hh activation in 3T3-L1 cells compared to other GLI activators, such as GLI1.

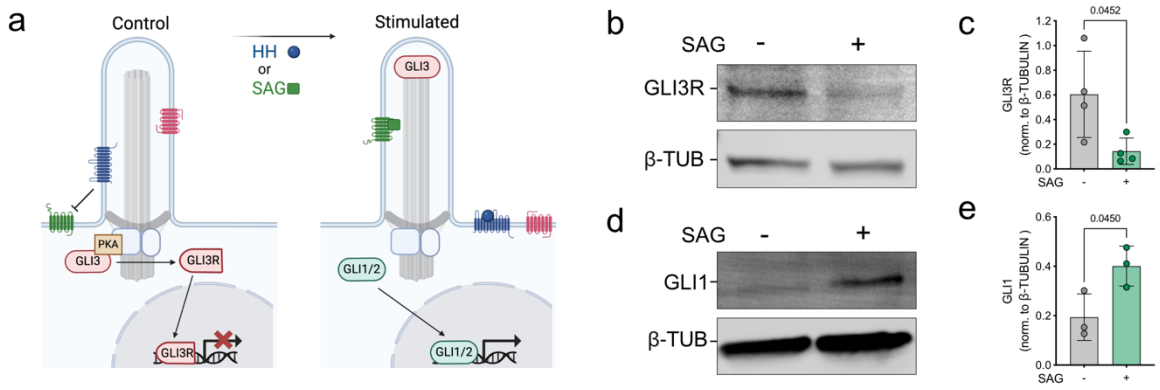

Fig. 22: Analyzing Hedgehog signaling using GLI1 and GLI3 proteolytic processing. **a.** Scheme depicting regulation of GLI3 by phosphorylation leading to its patrial degradation into GLI3 Repressor (GLI3R) in the control condition. After stimulation GLI3 is sequestered at the ciliary tip and not cleaved into its repressor form. Other GLI transcription factors can activate Hh-dependent gene transcription. **b.** Western Blot of

3T3-L1 cell lysates stimulated with or without 100 nM SAG for 24 h, stained with anti-GLI3R antibody and β-TUBULIN (β-TUB) as a loading control. **c.** Quantification of GLI3R protein normalized to β-TUB. Experimental numbers equal n = 4. **d.** Western Blot of 3T3-L1 cell lysates stimulated with or without 100 nM SAG for 24 h, stained with anti-GLI1 antibody and β-TUB as a loading control. **e.** Quantification of GLI1 protein normalized to β-TUB. Experimental numbers equal n = 3. **c, e.** Data are shown as individual values (dots) and mean (bars) ± SD.; p-values were calculated by an unpaired t-test.

3.6.3 Analyzing Hedgehog downstream signaling via *Gli1* and *Ptch1* expression

To analyze whether Hh activation also engaged downstream signaling, I analyzed Hh gene expression using reverse-transcription quantitative PCR (RT-qPCR). Among other targets, Hh signaling induces the expression of *Gli1* and *Ptch1* (Fig. 23 a). Indeed, in both 3T3-L1 and SVF Lin- cells, 24 h of SAG stimulation increased *Gli1* and *Ptch1* expression (Fig. 23 b-c), but the extent of target gene induction varied between the two cell models: whereas in 3T3-L1 cells, Gli1 expression increased by 2.1 ± 0.8-fold and *Ptch1* expression increased 2.8 ± 0.9-fold, in SVF Lin- cells, expression increased 22.1 ± 18-fold and 27.6 ± 23-fold, respectively. While both cell models readily respond to SAG stimulation, it is important to acknowledge the inherent differences between immortalized 3T3-L1 cells and primary cells.

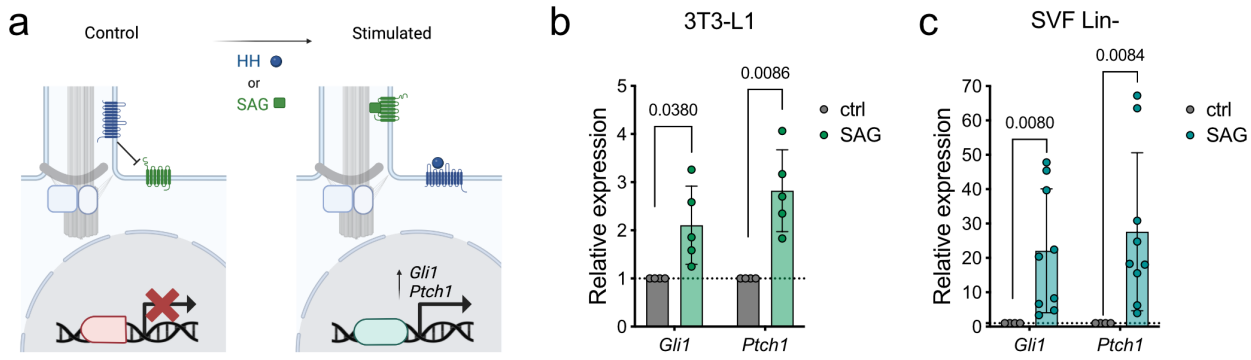

Fig. 23: Analyzing Hedgehog signaling using *Gli1* and *Ptch1* expression. a. Scheme depicting regulation of *Gli1* and *Ptch1* gene expression in ciliated cells under control and stimulated conditions. **b,c.** Hh target gene expression in 3T3-L1 and SVF Lin- cells after stimulation with 1 µM SAG for 24 h. Gene expression is normalized to the unstimulated conditions. Data are shown as individual values (dots) and mean (bars) ± SD. Different n are indicated by dots; p-values were calculated by a one sample t-test.

3.6.4 Stimulation of Hh signaling using the PTCH1 ligand Sonic hedgehog (SHH)

SAG induces Hh signaling by binding to SMO and promoting its localization to the cilium (Chen et al., 2002). Endogenously, the pathway is activated by ligand binding to the receptor PTCH1, causing its removal from the cilium and, thereby, allowing SMO to enter (Huang et al., 2022). Thus, SMO localization in the cilium and downstream signaling induced by SAG may not fully recapitulate the physiological activation of the Hh pathway. Therefore, I compared SAG to SHH stimulation. To achieve biological activity, the 45 kDa precursor protein undergoes autoproteolysis, generating two distinct products: the 27 kDa C-terminal part and the 19 kDa N-terminal signaling domain. The C-terminal domain catalyzes cholesterylation of the N-terminus, thereby, anchoring it to the cell membrane (J. Lee et al., 1994; Porter et al., 1996). Extracellular release of the cholesterol-modified ligand is mediated by other proteins and is necessary for long-range signaling activity (Creanga et al., 2012; Zeng et al., 2001). To facilitate immediate secretion of the ligand by circumventing membrane tethering of the N-terminal moiety, the Beachy lab cloned a cDNA construct (*ShhN*, addgene ID: 37680, unpublished). *ShhN* lacks the C-terminal domain of the SHH precursor protein but retains the biological activity (Lewis et al., 2001). Transfection of HEK293T cells with *ShhN* generates biologically active SHH (referred to as ShhN in the following), which is secreted instead of being anchored to the membrane (Peters et al., 2004). I transfected HEK293T cells with *ShhN*, harvested the supernatant after 24 h, and confirmed its expression by dot blot analysis, comparing it to the supernatant of mock-transfected cells (Fig. 24 a-b). Subsequently, I used the ShhN supernatant to stimulate Hh signaling in 3T3-L1 and SVF Lin- cells. ShhN supernatant was freshly prepared for each experiment, with expression confirmed by dot blot analysis each time.

ShhN stimulation significantly increased ciliary SMO localization in both cell models, as measured by both intensity parameters (Fig. 24 c, e), and also increased the expression of both Hh target genes after 24 h stimulation (Fig. 24 d, f). However, the concentration of ShhN in the supernatant can vary between experiments and the experimental setup is rather intense, especially when simultaneously handling primary cells. In addition, the medium used for HEK293T transfection differs from the medium used for primary SVF

culture, which might also affect gene expression. Since ShhN stimulation did not differ from SAG in Hh activation, I decided to use SAG for downstream experiments.

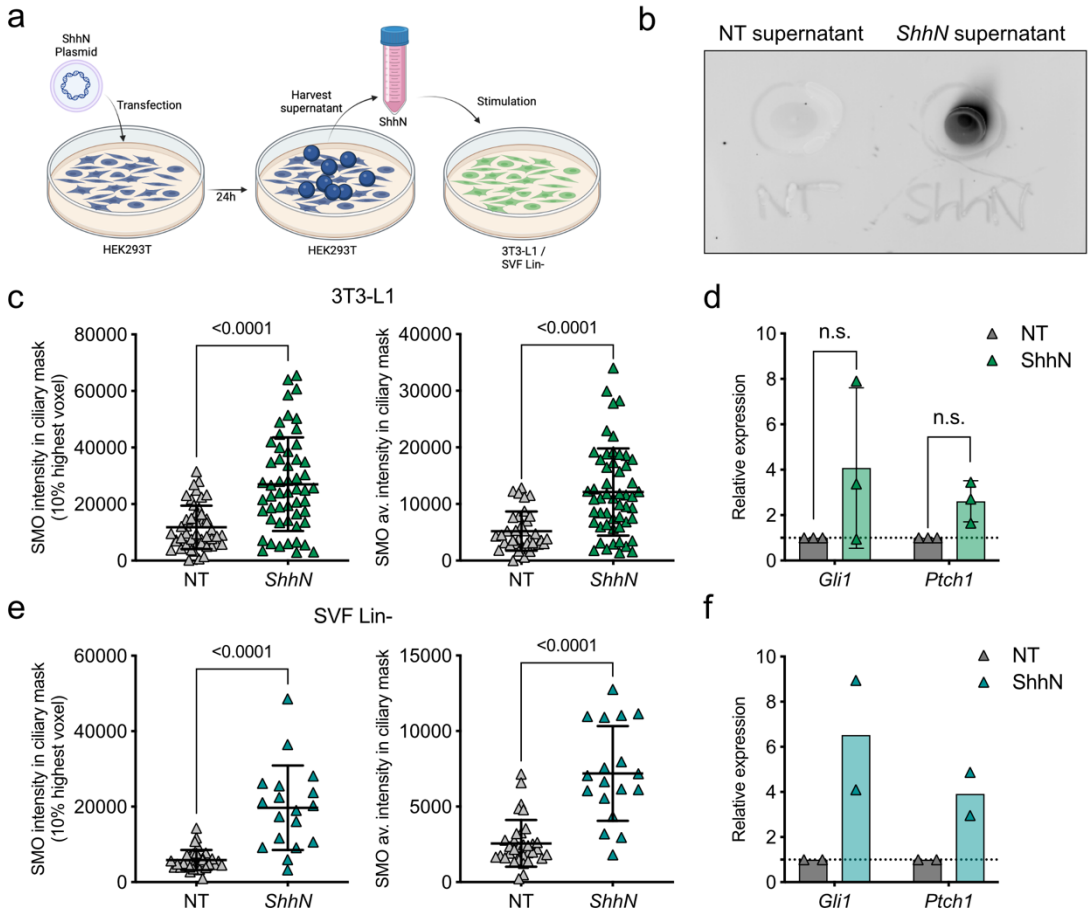

Fig. 24: Analysis of ciliary Hh signaling using SMO labeling and *Gli1* and *Ptch1* expression after stimulation with ShhN. a. Schematic of the experimental set-up. Transfection of HEK293T cells with *ShhN* leads to the production of the N-terminal SHH ligand (ShhN), but without cholesterol modification. That leads to the secretion of the protein in the supernatant which is used to stimulate either 3T3-L1 or SVF Lin- cells. **c.** Dot blot of ShhN and non-transfected (NT) supernatant to verify SHH expression. **c.** Quantification of SMO intensity parameters **c.** 3T3-L1 and **e.** SVF Lin- cells after 24 h stimulation with ShhN supernatant (ShhN) or control supernatant (NT). Datasets were tested for normality distribution, and statistical differences were calculated using either an unpaired t-test or a Mann-Whitney test. Each datapoint represents a single primary cilium. **d, f.** Hh target gene expression in 3T3-L1 and SVF Lin- cells after stimulation with ShhN or NT supernatant for 24 h. Gene expression is normalized to the unstimulated conditions. Data are shown as individual values (dots) and mean (bars) ± SD. Different n are indicated by dots; p-values were calculated by a one sample t-test. Non-significant (n.s.).

3.7 Analyzing Hh signaling in *Bbs8*$^{-/-}$ APCs

3.7.1 Hh signaling in primary *Bbs8*$^{-/-}$ APCs

The BBSome controls the ciliary export of receptors, including receptors of the Hh pathway (Nager et al., 2017; Zhang et al., 2012; Ye et al., 2018). To investigate whether Hh signaling is affected in *Bbs8*$^{-/-}$ APCs, I employed the previously established readouts for Hh activation in cells isolated from lean *Bbs8*$^{+/+}$ and *Bbs8*$^{-/-}$ mice.

First, I analyzed ciliary SMO localization by performing immunocytochemistry on SVF Lin- cells isolated from lean *Bbs8*$^{+/+}$ and *Bbs8*$^{-/-}$ mice (5-9 weeks) (Fig. 25 a). Notably, SMO localization was already different under basal conditions: in comparison to *Bbs8*$^{+/+}$ cells, SMO intensity parameters were significantly increased in *Bbs8*$^{-/-}$ APCs (Fig. 25 a-b). Following SAG stimulation, ciliary SMO localization increased in both *Bbs8*$^{+/+}$ and *Bbs8*$^{-/-}$ cells (Fig. 25 a-b). However, the intensity of ciliary SMO remained significantly higher in *Bbs8*$^{-/-}$ cells compared to their wild-type counterparts. Given that SMO accumulates in the cilium of *Bbs8*$^{-/-}$ cells even in the absence of stimulation, and that SAG further promotes ciliary SMO localization, this causes further accumulation of SMO in the cilium, most likely due to impaired retrograde transport caused by loss of BBS8. Prior studies have demonstrated that ciliary SMO localization is regulated by BBSome components, particularly BBS7 (Zhang et al., 2012). Additionally, increased SMO localization has been reported in other BBS models (*Bbs1 M390R/M390R* knockin, *Bbs2*, *Bbs3, Bbs4*) (Zhang et al., 2011; Zhang, et al., 2012a). Collectively, my findings further highlight the critical role of the BBSome/BBS chaperonin complex in the retrograde transport of SMO.

The BBSome has also been implicated in regulating the ciliary localization of GPR161 (Mukhopadhyay et al., 2013; Nozaki et al., 2018). To test whether loss of BBS8 also affects GPR161 localization, I performed immunocytochemistry. In *Bbs8*$^{+/+}$ APCs, GPR161 localization decreased upon SAG stimulation (Fig. 25 c-d). However, in *Bbs8*$^{-/-}$ APCs, GPR161 remained in the cilium (Fig. 25 c-d), demonstrating that the loss of BBS8 also affects the retrograde transport of GPR161. A similar phenotype has been described for *Bbs1* mutants (Stubbs et al., 2023) further supporting the role of the BBSome in GPR161 localization.

To analyze whether these alterations in receptor localization impact downstream Hh signaling, I analyzed the expression of Hh target genes. Under basal conditions expression of *Gli1* and *Ptch1* was increased in *Bbs8*$^{-/-}$ APCs compared to *Bbs8*$^{+/+}$ APCs (Fig. 25 d). In line with the increased SMO localization, this suggests an ectopic activation of the Hh signaling pathway upon loss of BBS8. However, upon SAG stimulation, gene expression of *Gli1* and *Ptch1* was significantly reduced in *Bbs8*$^{-/-}$ APCs relative to *Bbs8*$^{+/+}$ APC, despite elevated ciliary SMO levels (Fig. 25 e). This suggests that the response to SAG is either attenuated due to pathway pre-activation or impaired due to GPR161 retention in the cilium, which may disrupt proper Hh signaling.

To further investigate the mechanism underlying increased Hh target gene expression, I analyzed GLI3 processing. In *Bbs8*$^{-/-}$ APCs, the GLI3FL/GLI3R ratio was slightly increased due to higher levels of GLI3FL (Fig. 25 f-g). GLI3 processing is regulated via ciliary cAMP-PKA signaling (J. Li et al., 2017; Tschaikner et al., 2021; B. Wang et al., 2000). Thus, elevated levels of GLI3FL may be the result of increased SMO accumulation, shifting the balance towards the activator form of GLI3. Consequently, the increase of the transcriptional activator form of GLI3 may underlie the increased expression of Hh target genes.

These results demonstrate that loss of BBS8 disrupts Hh signaling in APCs through two mechanisms: (1) constitutive Hh activation, leading to increased basal expression of Hh target genes, and (2) an attenuated response to Hh pathway stimulation.

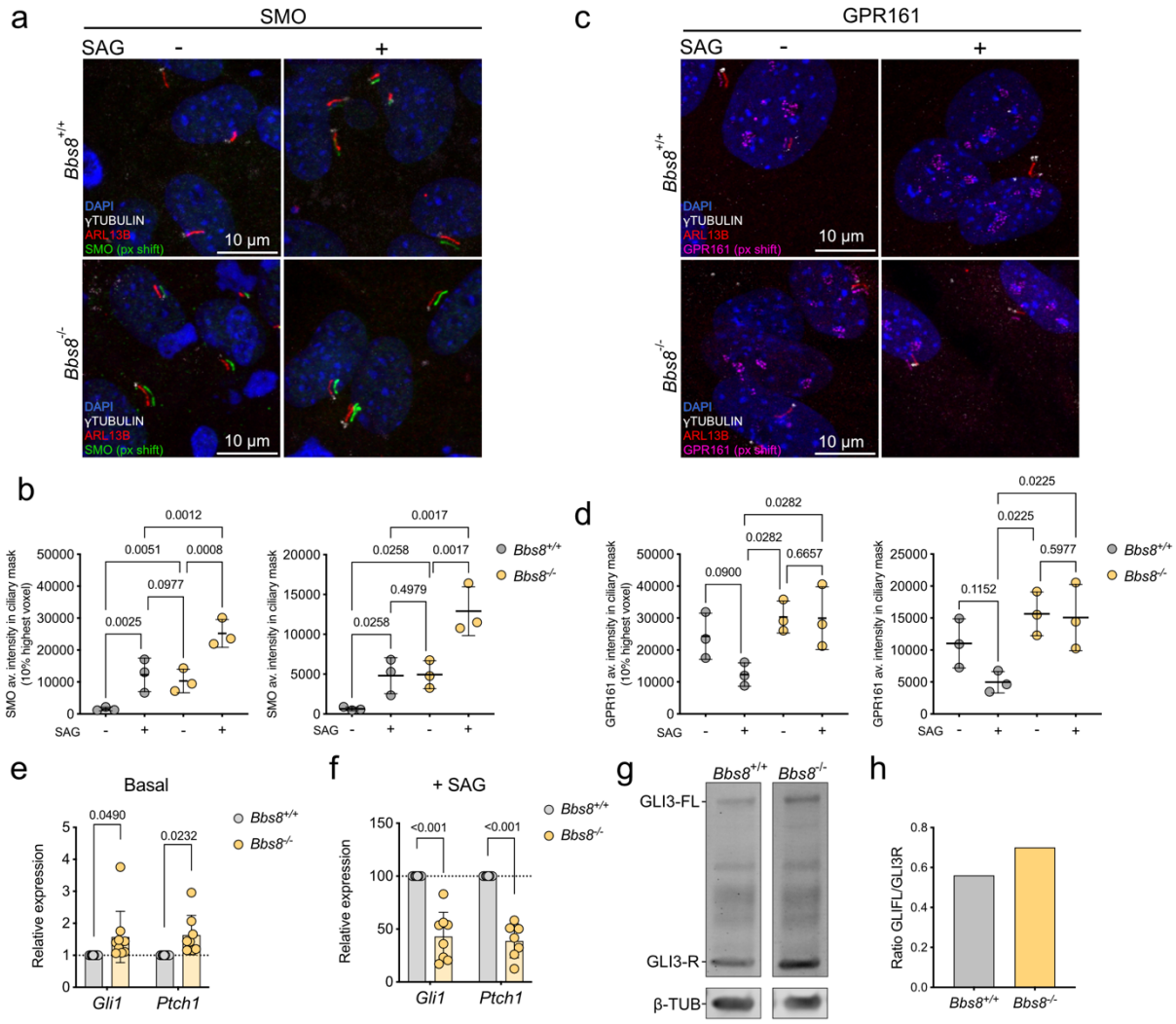

Fig. 25: Analyzing Hh signaling in *Bbs8*$^{-/-}$ SVF Lin- cells. a, b. Representative images of ciliated *Bbs8*$^{+/+}$ and *Bbs8*$^{-/-}$ SVF Lin- cells after stimulation with 1 µM SAG for 24 h. Cells have been labeled with DAPI (DNA, blue), an anti-γTUBULIN (white), an anti-ARL13B antibody (red), and either with **a.** anti-SMO antibody (green) or **c.** with an anti-GPR161 antibody (magenta). The green or magenta channel has been shifted by 5 pixel in each image. Scale bars are indicated. **b, d.** Quantification of **b.** SMO or **d.** GPR161 localization of ciliated *Bbs8*$^{+/+}$ and *Bbs8*$^{-/-}$ SVF Lin- cells. Data are shown as mean ± S.D. Experimental numbers equal n = 3; p-values were calculated using a one-way ANOVA. **d.** Basal Hh target gene expression in *Bbs8*$^{+/+}$ and *Bbs8*$^{-/-}$ SVF Lin- cells. **e.** Hh target gene expression in *Bbs8*$^{+/+}$ and *Bbs8*$^{-/-}$ SVF Lin- cells after stimulation with 1 µM SAG for 24 h. Gene expression is normalized to the *Bbs8*$^{+/+}$ expression values of the basal or treated (+ SAG) condition, respectively. Data are shown as individual values (dots) and mean (bars) ± S.D. Experimental numbers equal n = 9; p-values were calculated by a one sample t-test. **f.** Western Blot of *Bbs8*$^{+/+}$ and *Bbs8*$^{-/-}$ SVF Lin- cell lysates, stained with anti-GLI3R antibody and β-TUBULIN (β-TUB) as a loading control. **g.** Quantification of the ratio of GLI3 full length (GLI3FL) and GLI3R protein normalized to β-TUB. Experimental numbers equal n = 1.

3.7.2 Hh signaling in *Bbs8*$^{-/-}$ P1 APCs

Because the SVF Lin- cells isolated from *Bbs8*$^{+/+}$ and *Bbs8*$^{-/-}$ mice encompass all three APC subpopulations, I wanted to verify that the observed differences in Hh signaling occur in the P1 APCs. To this end, I isolated P1 cells from lean *Bbs8*$^{+/+}$ and *Bbs8*$^{-/-}$ mice (5-8 weeks) and stimulated them with SAG for 24 h. The results were similar to those obtained in SVF Lin- cells: basal ciliary SMO localization was increased in *Bbs8*$^{-/-}$ P1 cells and in both genotypes, SMO accumulation in the cilium was promoted upon SAG stimulation (Fig. 26 a-b). The gene expression of *Gli1* was significantly increased in *Bbs8*$^{-/-}$ P1 cells under basal conditions, while *Ptch1* expression exhibited a tendency for increased expression under basal conditions (Fig. 26 c). Expression of both Hh target genes was significantly reduced upon SAG stimulation compared to *Bbs8*$^{+/+}$ P1 cells.

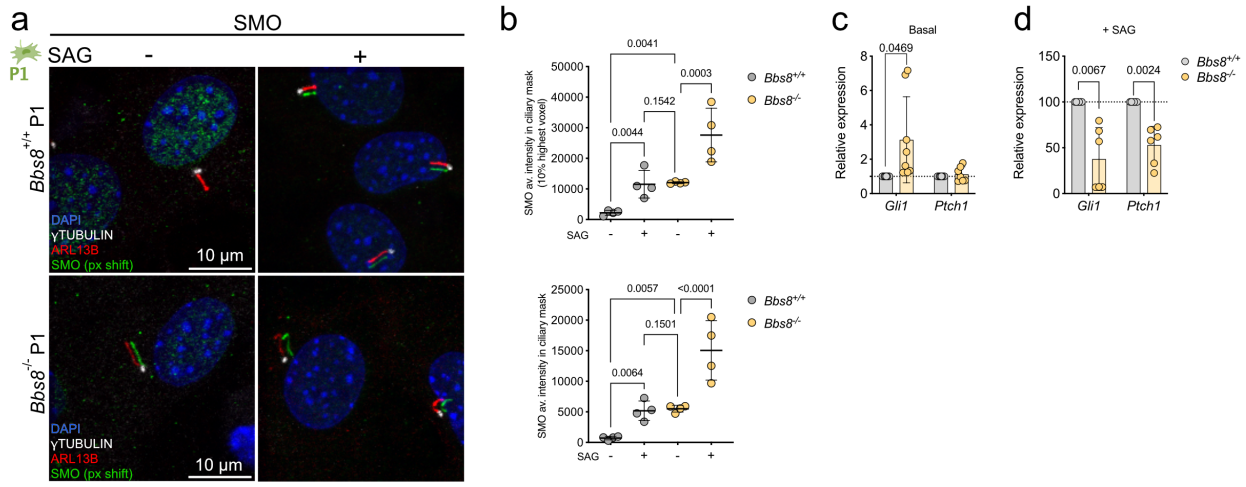

Fig. 26: Analyzing Hh signaling in *Bbs8*$^{-/-}$ P1 cells. a. Representative images of ciliated *Bbs8*$^{+/+}$ and *Bbs8*$^{-/-}$ P1 cells after stimulation with 1 µM SAG for 24 h. Cells have been labeled with DAPI (DNA, blue), an anti γTUBULIN (white), an anti-ARL13B antibody (red), and an anti-SMO antibody (green). The green channel has been shifted by 5 pixel in each image. Scale bars are indicated. **b,** Quantification of SMO localization of ciliated *Bbs8*$^{+/+}$ and *Bbs8*$^{-/-}$ P1cells. Data are shown as individual values (dots) and mean (rectangle) ± S.D. Different n are indicated by different colors. As datasets were not normality distributed, statistical differences were calculated using a Kruskal- Wallis test and Dunn´s multiple comparison posthoc test, p-values are indicated. **c.** Basal Hh target gene expression in *Bbs8*$^{+/+}$ and *Bbs8*$^{-/-}$ P1 cells. **b.** Hh target gene expression in *Bbs8*$^{+/+}$ and *Bbs8*$^{-/-}$ P1 cells after stimulation with 1 µM SAG for 24 h. Gene expression is normalized to the *Bbs8*$^{+/+}$ expression values of the basal or treated (+ SAG) condition, respectively. Data are shown as individual values (dots) and mean (bars) ± S.D. Different n are indicated by dots; p-values were calculated by a one sample t-test.

Together, these findings further underline that loss of BBS8 results in aberrant pathway activation under basal conditions while simultaneously impairing the ability of cells to appropriately respond to Hh pathway stimulation.

3.8 Manipulating Hh signaling in *Bbs8*$^{-/-}$ MEFs

Previous work by Dr. Christina Klausen from our group identified a similar Hh phenotype in MEF cells derived from *Bbs8*$^{-/-}$ mice. Using MEFs is advantageous as these cells can be kept in culture for several passages, thus, allowing the further molecular characterization. Dr. Christina Klausen also demonstrated an increase in ciliary localization of SMO in *Bbs8*$^{-/-}$ MEFs compared to *Bbs8*$^{+/+}$ MEFs under basal conditions (Fig. 27 a) (Klausen, 2020). Of note, ciliary SMO localization was assessed by the parameter of colocalized volume, which quantifies the percentage of voxels in the cilium with a higher intensity than the threshold level of the general background expression in the image (Hansen et al., 2021). Upon SAG stimulation, ciliary SMO localization was increased in both *Bbs8*$^{+/+}$ and *Bbs8*$^{-/-}$ MEFs (Fig. 27 a). Since the maximum value of this parameter is 100 % of colocalization (due to saturation), an even greater increase of SMO localization upon SAG stimulation in *Bbs8*$^{-/-}$ MEFs was not quantified (Fig. 27 a).

Downstream, also the expression of Hh target genes was increased in *Bbs8*$^{-/-}$ MEFs compared to *Bbs8*$^{+/+}$ MEFs under basal conditions (Fig. 27 b). However, only *Ptch1* was significantly increased, while for *Gli1* expression only a tendency was observed. In line with previous findings, the response to SAG stimulation was dampened in *Bbs8*$^{-/-}$ MEFs compared to their wild-type counterparts (Fig. 27 b).

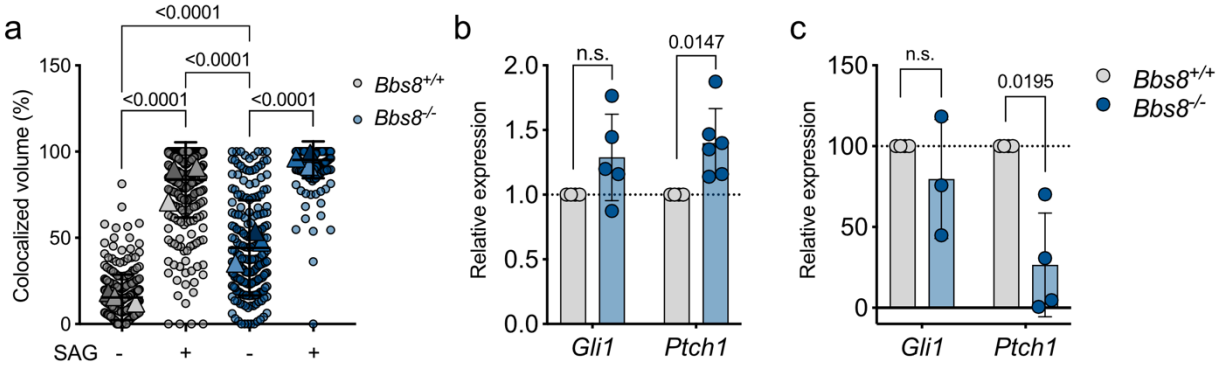

Fig. 27: Analyzing ciliary signaling phenotype in *Bbs8*$^{-/-}$ MEF cells. a. Quantification of SMO localization of ciliated *Bbs8*$^{+/+}$ and *Bbs8*$^{-/-}$ MEF cells. Data are shown as individual

values (dots) and mean (rectangle) ± S.D. Different n are indicated by different colors; As datasets were not normality distributed, statistical differences were calculated using a Kruskal-Wallis test and Dunn´s multiple comparison posthoc test, p-values are indicated. **b.** Basal Hh target gene expression in *Bbs8*$^{+/+}$ and *Bbs8*$^{-/-}$ MEF cells. **c.** Hh target gene expression in *Bbs8*$^{+/+}$ and *Bbs8*$^{-/-}$ MEF cells after stimulation with 1 µM SAG for 24 h. Gene expression is normalized to the *Bbs8*$^{+/+}$ expression values of the basal or treated (+ SAG) condition, respectively. Data are shown as individual values (dots) and mean (bars) ± S.D. Different n are indicated by dots; p-values were calculated by a one sample t-test. Some of the experiments were performed by Dr. Christina Klausen.

To further investigate the role of BBS8 in Hh signaling, I aimed to rescue the Hh signaling phenotype in *Bbs8*$^{-/-}$ MEFs by overexpressing *Bbs8*. To this end, a cDNA construct was cloned encoding *Bbs8* tagged with an HA-tag (pBbs8-HA). I performed nucleofection of *Bbs8*$^{-/-}$ MEFs and analyzed the localization of the construct using immunocytochemistry (Fig. 28 a) and verified the expression using an antibody against the HA-tag. The pBbs8-HA construct successfully localized to the cilium, as confirmed by quantification of HA-intensity in the ciliary mask (Fig. 28 a-b).

Transfection of *Bbs8*$^{-/-}$ MEFs significantly reduced the ciliary localization of SMO compared to non-transfected *Bbs8*$^{-/-}$ MEFs (Fig. 28 c). Of note, among the three parameters assessed for SMO localization in MEFs, only the 10 % highest intensity voxels and the colocalized volume parameters reflected the increased SMO localization *Bbs8*$^{-/-}$ MEFs and the subsequent rescue in transfected *Bbs8*$^{-/-}$ MEFs (Fig. 28 c). This highlights the importance in choosing the appropriate parameter when analyzing ciliary signaling.

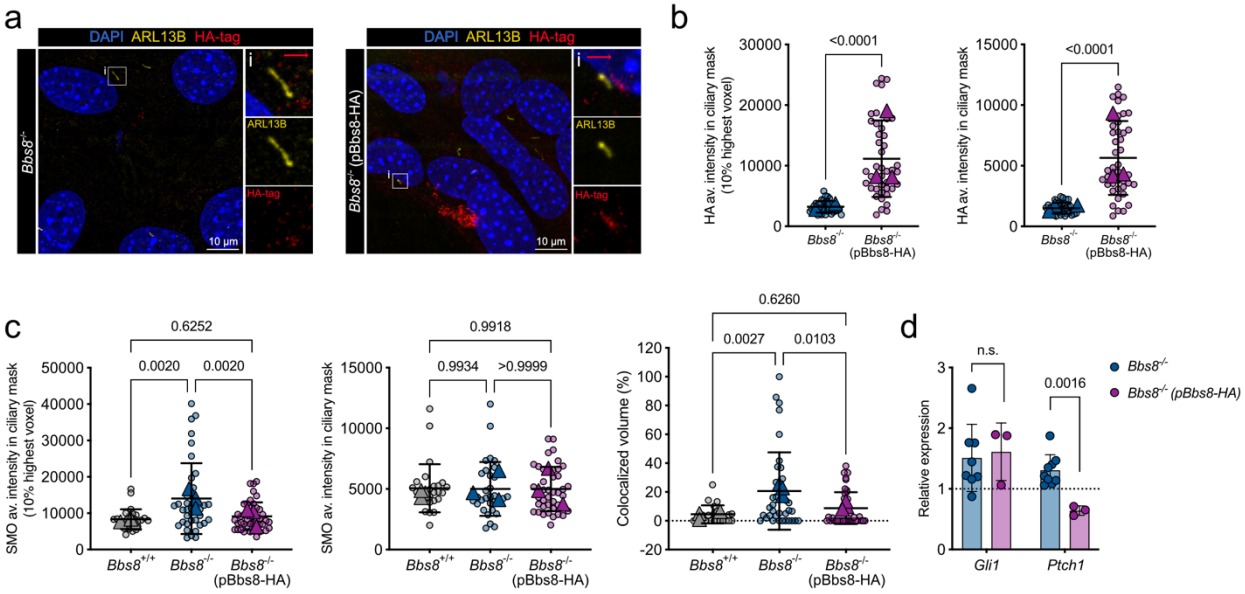

Fig. 28: Analyzing overexpression of *Bbs8* in *Bbs8*$^{-/-}$ MEF cells. a. Representative images of ciliated *Bbs8*$^{-/-}$ MEF cells that have been transfected with an pBbs8-HA construct (right) or non-transfected *Bbs8*$^{-/-}$ MEF cells (left). Cells have been labeled with DAPI (DNA, blue), an anti-ARL13B antibody (yellow), and an anti-HA-tag antibody (red). White boxes are shown as magnified view. The red channel has been shifted by 5 pixels in each image. Scale bars = 10 µm. **b,** Quantification of HA localization to the primary cilium in non-transfected and transfected *Bbs8*$^{-/-}$ MEF cells. Data are shown as individual values (dots) and mean (rectangle) ± S.D. Different n are indicated by different colors; p-values were calculated by an unpaired t-test. **c.** Quantification of SMO localization of ciliated *Bbs8*$^{+/+}$, *Bbs8*$^{-/-}$ MEF cells and *Bbs8*$^{-/-}$ MEF cells that were transfected with an pBbs8-HA construct. Data are shown as individual values (dots) and mean (rectangle) ± S.D. Different n are indicated by different colors; p-values were calculated by a one-way ANOVA. **d.** Basal Hh target gene expression in *Bbs8*$^{+/+}$, non-transfected *Bbs8*$^{-/-}$, and transfected *Bbs8*$^{-/-}$ MEF cells. Gene expression is normalized to the *Bbs8*$^{+/+}$ expression values (shown as the dotted line). Data are shown as individual values (dots) and mean (bars) ± S.D. Different n are indicated by dots; p-values were calculated by an unpaired t-test. Non-significant (n.s.).

To investigate whether reduced SMO localization also affected downstream Hh signaling, I analyzed target gene expression. Indeed, overexpression of pBbs8-HA significantly decreased *Ptch1* expression in *Bbs8*$^{-/-}$ MEFs (Fig. 28 d). Expression of *Gli1* was not significantly affected by overexpression of *Bbs8* (Fig. 28 d). The transcription of *Gli1* is regulated by multiple processes, including epigenetic modifications (Taylor et al., 2019). Thus, *Gli1* expression in MEFs might be controlled by a distinct mechanism and that canonical Hh activation may play a secondary role in activating gene transcription. Overall, my results give further insight in the mechanistical role of BBS8 in facilitating proper SMO localization under basal conditions.

3.9 Does Hh signaling induce a phenotypic switch in APCs?

I have shown that the dysregulation of Hh signaling in *Bbs8*$^{-/-}$ cells leads to ectopic pathway activation. Moreover, I have observed a fate change in *Bbs8*$^{-/-}$ APCs towards a fibrogenic phenotype. Since activation of the Hh pathway is implicated in promoting fibrogenesis across various tissues (Fabian et al., 2012; Y. Hu et al., 2024; Shen et al., 2017), I hypothesized that aberrant Hh activation in *Bbs8*$^{-/-}$ APCs drives the observed fate change.

Ectopic Hh activation in *Bbs8*$^{-/-}$ cells resulted in a 1.5 ± 0.8-fold increase in *Gli1* expression and 1.6 ± 0.6-fold increase in *Ptch1* expression (Fig. 25 e). In comparison, treatment of wild-type SVF Lin- cells with 1 µM SAG led to a much stronger induction, with increased *Gli1* expression by 22.1 ± 18-fold and increased *Ptch1* expression by 27.6 ± 23-fold, respectively (Fig. 23 c). Thus, I decided to stimulate the SVF Lin- cells with a lower concentration of SAG (100 nM) and for two days to approximate the pre-activated Hh state observed in the *Bbs8*$^{-/-}$ cells (Fig. 29 a).

First, I analyzed whether SAG stimulation would result in an increase of the fibrogenic CD9^{high} population observed in the gWAT of lean *Bbs8*$^{-/-}$ mice. However, stimulation with SAG did not significantly alter the frequency of the CD9^{high} population in gWAT APCs from wild-type mice (Fig. 29 b). Previous work by Marcelin *et al.* demonstrated that activation of the PDGFRα signaling pathway induces the transition towards CD9^{high} cells *in vivo* (Marcelin et al., 2017), which could be affected after *in-vitro* culture, whereby the cells potential to dynamically respond to external stimuli might be hampered.

Next, I investigated if Hh activation would increase fibrogenic gene expression. To this end, I quantified the relative gene expression of different collagens, *Loxl2*, and *Fbn* in wild-type SVF Lin- cells isolated from murine iWAT. Although there was a trend towards increased *Fbn* expression, I was not able to observe significant changes in other fibrogenic genes (Fig. 29 c). *In-vitro* cell culture has been reported to alter the transcriptional program of human adipose-derived stem cells, particularly in genes associated with cell signaling and adhesion (Januszyk et al., 2015). The central genes that were affected by *in-vitro* culture were extracellular-related kinase (ERK)1/2 and focal

adhesion kinase, both closely associated with the development of fibrosis (Foglia et al., 2019; Seong et al., 2013; X. K. Zhao et al., 2016). Thus, I hypothesized that *in vitro* culture may obscure the effects of SAG stimulation on fibrogenic gene expression.

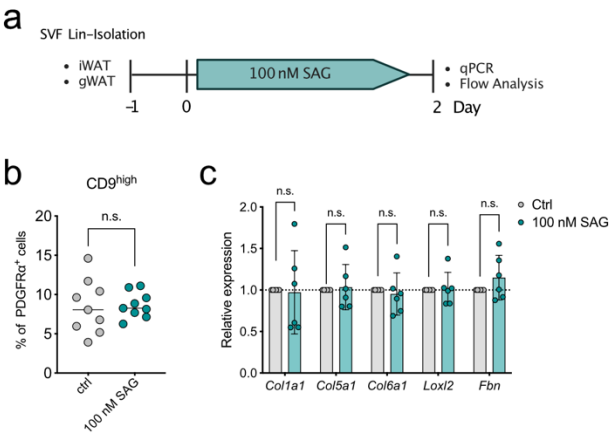

Fig. 29: Analyzing the effect of SAG stimulation on fibrogenic gene expression in SVF Lin- cells. a. Scheme of experimental set-up. **b.** Quantification of CD9^{high} cell surface expression on PDGFRα+ cells isolated from the murine gWAT following 100 nM SAG stimulation for 2 days. Data are shown as individual values (dots) of an experimental number equal n = 9. **c.** Relative gene expression of *Col1a1*, *Col5a1*, Col6a1, *Loxl2,* and *Fbn* in SVF Lin- cells isolated from murine iWAT treated with 100 nM SAG for 2 days. Gene expression is normalized to the control samples. Data are shown as individual values (dots) and mean (bars) ± S.D. Different n are indicated by dots; p-values were calculated by a one sample t-test. Non-significant (n.s.).

To circumvent this limitation, I employed the 3T3-L1 cell line, which is (1) well-adapted to *in vitro* conditions and (2) responsive to Hh signaling. To establish the appropriate conditions to mimic the ectopic Hh activation, I stimulated 3T3-L1 for 24, 48, and 72 h with two different SAG concentrations (Fig. 30 a). I analyzed Hh activation by quantifying gene expression of *Gli1* and *Ptch1* (Fig. 30 b). Both SAG concentrations induced a time-dependent increase in Hh target gene expression, with the strongest activation occurring after 72 h stimulation of 1 µM SAG (Fig. 30 b). Additionally, I measured relative expression of *Col1a1* as a proxy for fibrogenic gene expression at different time points. Interestingly, *Col1a1* expression peaked after 24 h of 100 nM SAG treatment, showing a 2.5-fold increase (Fig. 30 c). Expression decreased after 48 h and rose again after 72 h, suggesting a potential feedback mechanism. It has been shown that increased production of ECM components, such as collagen type 1, and a resulting remodeling of the extracellular environment greatly impact in transcriptional regulation of many genes, including genes involved in ECM remodeling (Garamszegi et al., 2010; Spencer et al., 2007).

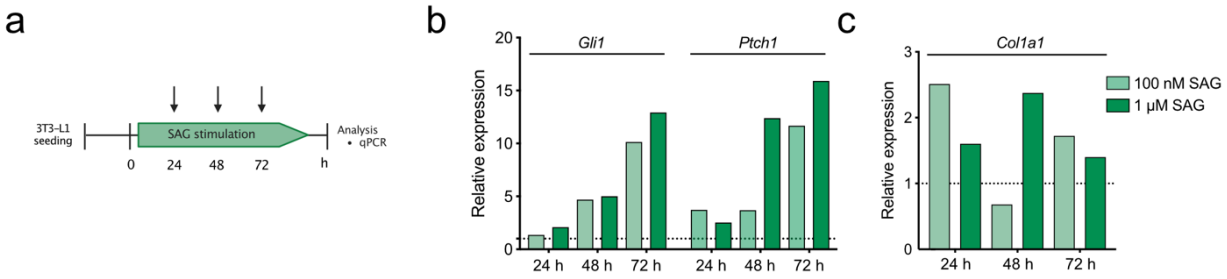

Fig. 30: Analyzing the effect of SAG stimulation on fibrogenic gene expression in 3T3-L1 cells. a. Scheme of experimental set-up. **b, c.** Gene expression of **b.** Hh target genes *Gli1* and *Ptch1* and **c.** *Col1a1* in 3T3-L1 cells treated with 100 nM or 1 µM SAG for 24, 48 or 72 h. Gene expression is normalized to the vehicle control treated samples. Data are shown as mean of an experimental number equal n = 2.

Based on these findings, I selected the 24 h time point and 100 nM SAG concentration for further analysis of fibrogenic gene expression. Indeed, low-grade activation of Hh signaling was sufficient to induce a fibrogenic gene expression signature in 3T3-L1 cells, as indicated by an increase in expression of the collagens *Col1a1* and *Col5a1*, and other ECM components such as *Sparc* and *TnC* (*Tenascin C*) (Fig. 31 a).

In turn, I hypothesize that the ectopic activation of Hh signaling in *Bbs8*$^{-/-}$ APCs drives the fibrogenic switch *in vivo*.

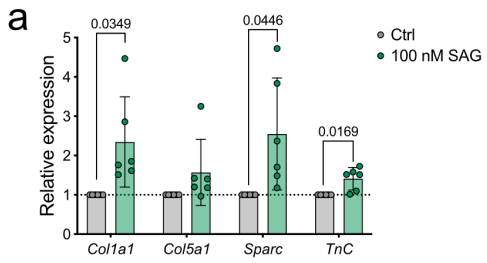

Fig. 31: Analyzing the effect of low-grade SAG stimulation on fibrogenic gene expression in 3T3-L1 cells. a. Gene expression of *Col1a1*, *Col5a1*, *Sparc* and *TnC* in 3T3-L1 cells treated with 100 nM SAG for 24 h. Gene expression is normalized to the vehicle control treated samples. Data are shown as individual values (dots) and mean (bars) ± S.D. Different n are indicated by dots; p-values were calculated by a one sample t-test.

3.10 Analyzing Vismodegib treatment to ameliorate Hh signaling in *Bbs8*$^{-/-}$ APCs

To assess whether inhibiting Hh signaling in *Bbs8*$^{-/-}$ APCs is sufficient to revert the observed phenotype, I treated cell with Vismodegib. Aberrant Hh signaling is implicated in different types of cancers (Sari et al., 2018). Vismodegib (Erivedge®, Genentech-Curis) has been approved by the US Food and Drug Administration for treatment of adults with advanced basal cell carcinoma (Proctor et al., 2014; Sekulic et al., 2012). Since uncontrolled SMO signaling is the primary driver for development of BCC, Vismodegib

acts by directly binding and inhibiting SMO, thereby, blocking downstream pathway activation (Fig. 32 a) (Robarge et al., 2009).

Since loss of BBS8 increased ciliary SMO localization and Hh target gene expression, I tested whether blocking SMO activity could reduce Hh activation in *Bbs8*$^{-/-}$ APCs. To this end, I treated SVF Lin- cells isolated from *Bbs8*$^{-/-}$ mice with Vismodegib for 48 h and, subsequently, analyzed gene expression (Fig. 32 b). Indeed, *Gli1* expression was significantly downregulated compared to untreated *Bbs8*$^{-/-}$ cells, while *Ptch1* expression exhibited a trend towards decreased expression upon Vismodegib treatment (Fig. 32 b). Next, I investigated whether the reduction in Hh signaling also affected fibrogenic gene expression. Indeed, expression of *Col1a1*, which was elevated in *Bbs8*$^{-/-}$ APCs compared to *Bbs8*$^{+/+}$ APCs, was significantly reduced following Vismodegib treatment (Fig. 32 c). Similar trends were observed for other fiborgenic genes, such as *Col5a1* and *Loxl2* (Fig. 32 c).

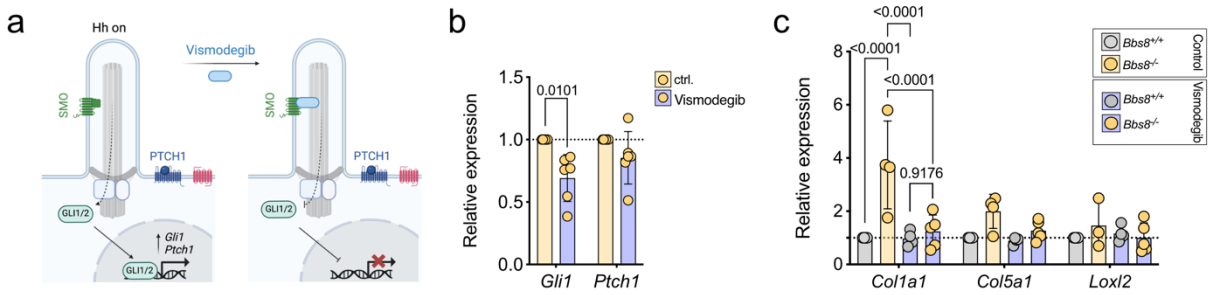

Fig. 32: Analyzing Vismodegib treatment in *Bbs8*$^{-/-}$ SVF Lin- cells. a. Scheme depicting the mechanism of action of Vismodegib in regulating Hh signaling by binding to SMO. **b.** Hh target gene expression in *Bbs8*$^{-/-}$ SVF Lin- cells after stimulation with 2 µM Vismodegib for 48 h. Gene expression is normalized to vehicle control. **c.** Gene expression of the fibrogenic genes *Col1a1*, *Col5a1*, and *Loxl2* in *Bbs8*$^{+/+}$ and *Bbs8*$^{-/-}$ SVF Lin- cells after stimulation with 2 µM Vismodegib for 48 h. Gene expression is normalized to the vehicle control treated samples of the *Bbs8*$^{+/+}$ cells. Data are shown as individual values (dots) and mean (bars) ± S.D. Different n are indicated by dots; p-values were calculated by a one sample t-test.

Overall, these results underline the direct correlation of Hh signaling and the increase in fibrogenic gene expression. Furthermore, pharmacological inhibition of the Hh signaling pathway effectively reduces fibrogenic gene expression.

3.11 Establishing *in vitro* culture of the Thymus as an alternative model to investigate disturbed Hh signaling

Hh signaling plays an essential role in development across all tissues and organs and has also been implicated in regulating T-cell development (Crompton et al., 2007). Recently, Ernesto Picon-Galindo demonstrated in his doctoral thesis an increase in regulatory T cells (Tregs) in the visceral adipose tissue of *Bbs8*$^{-/-}$ mice, and he proposed that this is caused by cilia-dependent control of Treg differentiation in the thymus (Galindo, 2024). While immune cells lack primary cilia, thymic epithelial cells (TECs) are ciliated. Moreover, TECs are known to regulate T-cell development in the thymus. To examine whether loss of BBS8 affects TECs and contributes to the observed Treg phenotype in the WAT, I established two *in vitro* models to analyze TEC function.

3.11.1 Analyzing ciliation of thymic epithelial cells

To confirm that TECs are indeed ciliated and, thus, susceptible to dysregulated ciliary signaling, I established a strategy to culture these cells in vitro (Fig. 33 a).
The thymus as a primary lymphoid organ, generates and matures T cells. In the thymus, the most abundant cell population are CD45+ thymocytes, surrounded by the stromal compartment, which make up a significantly smaller compartment (Chakrabarti et al., 2022; Yayon et al., 2024). Within the stromal fraction, TECs represent the major population and can be identified by EpCAM expression (F. Klein et al., 2023; Ucar et al., 2014). To enrich TECs, I used magnetic separation to remove CD45+ cells (Fig. 33 a). Subsequent flow analysis, however, showed that even though I was able to identify EpCAM+ cells, CD45+ remained the prominent population (Fig. 33 b-c).
I proceeded with culturing the magnetically separated cells, reasoning that TECs, but not lymphocytes, would adhere to plastic. Using two different EpCAM antibodies, originally designed for flow cytometry, I identified EpCAM+ cells by immunocytochemistry after several days in culture (Fig. 33 d). Further analysis showed 16.4 ± 11.1 % of these cells were ciliated (Fig. 33 e). While this protocol allowed TEC isolation, the results are preliminary, and further validation using a TEC-specific reporter mouse is necessary.

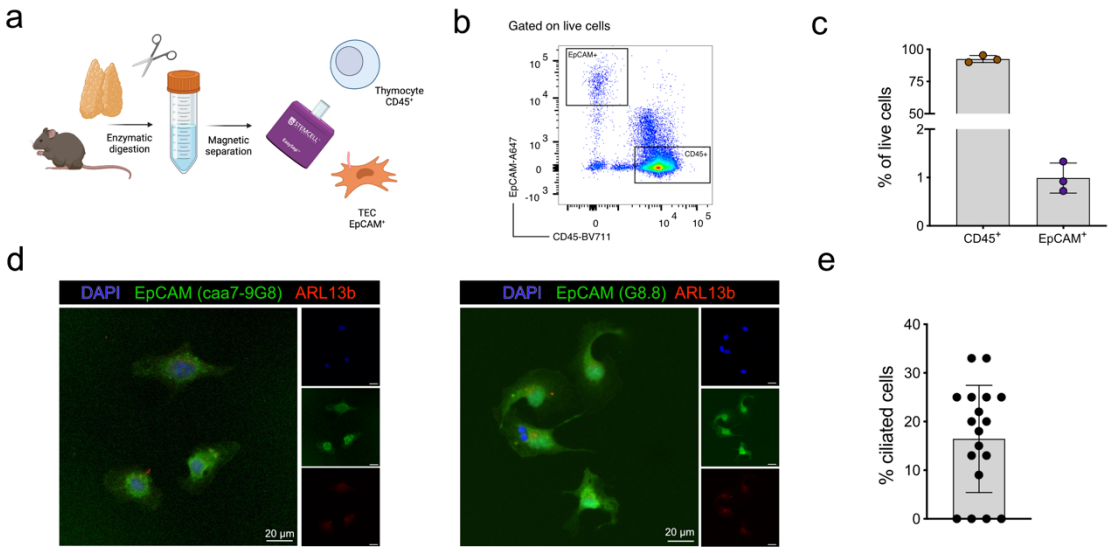

Fig. 33: Analyzing primary cilia in thymic epithelial cells (TEC). a. Experimental set-up to isolate cells of the thymus for analysis by flow cytometry or to bring into culture. **b.** Strategy to gate thymic epithelial cells (EpCAM$^+$) and CD45$^+$ cells. **c.** Quantification of the EpCAM$^+$ and CD45$^+$ fractions depicted in **b.** Data is shown as mean ± SD. Each data point represents one mouse from n = 3 mice in total. **d.** Exemplary fluorescence images of TECs that were isolated and kept in culture. Cells were stained with DAPI (nuclei, blue), an anti-ARL13b antibody (primary cilia, red), and two different EpCAM antibodies (green). Scale bar is indicated. **e.** Quantification of ciliated cells from **d.** by dividing the number of primary cilia by the total number of nuclei per image. Data is shown as mean ± SD. Each data point represents one image from n = 18 technical replicates.

3.11.2 Thymic organ culture

The major role of TECs is to provide a functional niche for T-cell development and establishing central tolerance. Thymic organ culture is a well-established system, supporting *in vitro* T-cell development (Jenkinson & Anderson, 1994). Moreover, this system can also be used to pharmacologically manipulate Hh signaling (Saldaña et al., 2016; Solanki et al., 2018). To this end, I employed this system by culturing freshly isolated thymi from P0 pups (Fig. 34 a). Subsequently, I analyzed T-cell populations in the thymus of P0 pups (0 d) and compared them to those cultured for three days (3 d) (Fig. 34 b, d-e).

First, I verified that *in vitro* culture did not significantly affect cell survival (Fig. 34 c). Developing thymocytes progress through distinct maturation stages, characterized by expression of CD4 and CD8: double-negative (DN; CD4$^-$CD8$^-$), double-positive (DP; CD4$^+$CD8$^+$), CD8 single-positive (CD8SP; CD4$^-$CD8$^+$), and CD4 single-positive (CD4SP; CD4$^+$CD8$^-$) (Fig. 34 b). During negative selection, CD4SP thymocytes interact with TECs,

which present tissue-restricted antigens (TRA). Cells with high reactivity for TRA undergo apoptosis (negative selection), and the rest exits the thymus as naïve T cells. Additionally, self-reactive CD4SP thymocytes can also differentiate into Treg cells by expressing FOXP3 and high levels of CD25. For Treg differentiation a two-step model has been proposed, in which Treg progenitor cells initially express either CD25 ($CD25^+$ TregP) or FOXP3 ($Foxp3^+$ TregP) (Owen et al., 2019).

I was able to identify all T-cell population after three days of culture and only observed minor differences compared to freshly isolated P0 thymi (Fig. 34 d-e). Notably, the DP population and the proportion of mature Tregs was slightly increased (Fig. 34 d-e). Other labs commonly use fetal thymic organ culture to investigate T-cell development. Here, I preliminary established a system that allows to analyze T-cell development postnatally *in vitro*.

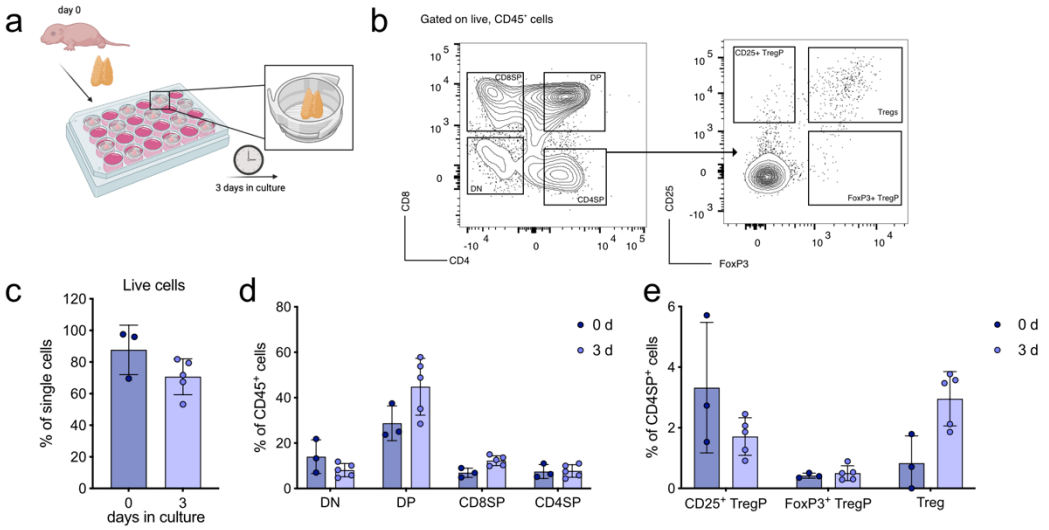

Fig. 34: Analysis of T-cell population in thymic organ culture. a. Overview of the set-up for the thymic organ culture. **b.** Strategy to gate the T-cell subsets in mice. **c.** Percentage of live cells before and after 3 days of culture. **d.** Quantification of the frequency of double-negative (DN, $CD4^-CD8^-$), double-positive (DP, $CD4^+CD8^+$), CD8 single-positive (CD8SP, $CD4^-CD8^+$), and CD4 single-positive (CD4SP, $CD4^+CD8^-$) thymocytes in $CD45^+$ cells before (0 d) and after 3 days of culture (3 d). **e.** Quantification of the frequency of regulatory T progenitor cells (TregP) expressing CD25 ($CD25^+$ TregP, $CD25^+FoxP3^-$) or FoxP3 ($FoxP3^+$TregP, $CD25^-FoxP3^+$) and mature Treg cells ($CD25^+FoxP3^+$) in CD4SP cells before (0 d) and after 3 days of culture (3 d). Data is shown as mean ± SD. Each data point represents one thymus from n = 3 (d 0) and n = 5 (d 3) mice.

4. Discussion

In my doctoral thesis, I demonstrated that BBS8-dependent ciliary signaling maintains the fate and function of APCs in WAT. I could show that all APC subpopulations in the WAT are ciliated and responsive to ciliary cues. Loss of BBS8 affected the balance of the APC subpopulations, reducing the stem cell-like P1 population, while a pro-fibrogenic subpopulation of $CD9^{high}$ cells emerged. In turn, fibrogenic remodeling was observed in the whole adipose tissue and was promoted by *Pdgfra*-expressing cells. A similar phenotype of PDGFRα-dependent, fibrotic WAT remodeling has previously been described as a consequence of obesity (Marcelin et al., 2017). However, I observed the remodeling due to the loss of BBS8 in the lean state before the onset of obesity. Molecularly, the loss of BBS8 disrupted the ciliary localization of SMO and GPR161, leading to an ectopic activation of the Hh pathway in APCs. In turn, low-grade Hh signaling induced a fibrogenic gene signature in APCs, thereby linking cell fate regulation with Hh signaling. Furthermore, ectopic Hh pathway activation in *Bbs8*$^{-/-}$ APCs was reduced by the SMO inhibitor vismodegib *in vivo*, which also ameliorated the fibrogenic gene signature, providing a potential therapeutic target to treat fibrotic remodeling.

4.1 The role of BBS proteins in regulating ciliary (GPCR) signaling

Dynamic changes in membrane protein composition of the primary cilium are central to ciliary signaling, yet the mechanisms that regulate membrane protein flux remain poorly understood. The BBSome controls the ciliary trafficking of GPCRs, as evidenced by various *Bbs* mutants that exhibit accumulation of ciliary receptors, such as the leptin receptor, SMO, GPR161, or the Dopamine receptor 1 (Domire et al., 2011; Guo et al., 2016; Zhang, Seo, et al., 2012).

The Hh pathway requires the coordinated import and export of receptors in the ligand-free “OFF” state and when transitioning to the “ON” state upon ligand binding. I demonstrated that the loss of the BBSome core component BBS8 disrupted ciliary receptor localization both at baseline and upon Hh pathway activation. In *Bbs8*$^{-/-}$ cells, SMO accumulated in the cilium even in the absence of stimulation, and SAG stimulation further enhanced localization of the receptor. Moreover, upon Hh stimulation, GPR161 remained in the

cilium of *Bbs8*$^{-/-}$ cells, suggesting a direct role for BBS8 in facilitating the retrograde transport of ciliary receptors. This phenotype is in line with that reported of other BBSome mutants: in BBS1, BBS2, BBS4, BBS7, and ARL6/BBS3 mutants, SMO significantly accumulates within cilia under basal conditions and in BBS1, BBS4, and ARL6/BBS3 mutants GPR161 is retained in the cilium even after treatment with SAG (Nozaki et al., 2018; Prasai et al., 2020; Zhang et al., 2011; Zhang et al., 2012a).

The different BBS proteins have distinct locations and functions within the BBSome complex. Therefore, on a molecular level, the phenotype I observed in *Bbs8*$^{-/-}$ cells could result from (1) an altered structure of the BBSome affecting the assembly or stability of the complex or (2) the direct binding of cargo by BBS8.

To determine whether the loss of BBS8 affects BBSome structure, both the overall architecture of the protein complex and the specific role of BBS8 within the complex needs to be further analyzed. Recent studies have resolved the BBSome structure at a resolution of 3.1 - 3.4 Å using cryo-electron microscopy (Chou et al., 2019; Klink et al., 2017; Singh et al., 2020; Klink et al., 2020; Yang et al., 2020). The BBSome can adopt both an open and a closed conformation, reflecting its activation status. Only in the open confirmation can the complex bind the small GTPase ARL6/BBS3, which is essential for activation. ARL6/BBS3 facilitates BBSome targeting to the ciliary membrane, and the open conformation also exposes binding sites for the cargo proteins transported by the complex (Chou et al., 2019; Fan et al., 2004; H. Jin et al., 2010; Mouraõ et al., 2014; Singh et al., 2020). BBS8 occupies a central position within the BBSome and contains tetratricopeptide repeats (TPRs) that form α-solenoids (Ansley et al., 2003). It binds to BBS18, the smallest BBSome subunit, and together they serve as a structural linker for BBS4 and BBS9, stabilizing the core of the complex (Chou et al., 2019; Klink et al., 2017; Klink et al., 2020). Given its central position, absence of BBS8 may disrupt complex assembly or integrity. However, in cells depleted of BBS8, only minor changes in complex assembly are observed (Seo et al., 2011). In contrast, the loss of BBS1 completely disrupts BBSome formation, likely leading to the mislocalization of ciliary GPCRs (Seo et al., 2011; Zhang, Yu, et al., 2012b). In *BBS1* knockout cells, the impaired trafficking of SMO and GPR161 is rescued by the exogenous expression of *BBS1* (Nozaki et al., 2018). However, expression of a truncated BBS1 variant (BBS1$^{1–575}$), capable of interacting with BBS7 and ARL6/BBS3 but not with BBS9, is not able to rescue the phenotype, demonstrating that

the integrity of the whole BBSome complex is crucial for its role in retrograde trafficking of ciliary GPCRs (Nozaki et al., 2018).

Notably, a positively charged patch of BBS8 interacts with the β-propeller domain of BBS9, stabilizing their interface (Klink et al., 2020). Mutations at this interface, such as Q325R in the β-propeller domain of BBS9, have been reported in BBS patients (Chou et al., 2019; Klink et al., 2020; Ullah et al., 2017). Similarly, the L58* mutation in BBS18 disrupts interaction with BBS8 and is classified as a disease-causing variant (Klink et al., 2020; Scheidecker et al., 2014). Thus, while the loss of BBS8 has only minor effects on BBSome assembly *per se*, it may significantly impact complex integrity in a BBS9- and BBS18-dependent manner.

Upon Hh pathway activation, a signal-dependent redistribution of the BBSome at the ciliary tip is required for GPR161 retrieval (Ye et al., 2018). Recruitment to the tip is mediated by KIF7, which co-immunoprecipitates with several BBSome subunits, including BBS8 (Ye et al., 2018). However, it remains unclear whether the loss of BBS8 affects KIF7 binding and, consequently, tip recruitment.

Upon pathway activation, activated GPCRs accumulate at the ciliary tip, where they are recognized by the GPCR activation sensor β-arrestin (Pal et al., 2016; Ye et al., 2018). β-arrestin directs the ubiquitination of GPCRs, after which TOM1-like protein 2 (TOM1L2) bridges the ubiquitinated cargo and the BBSome (Shinde et al., 2020; Shinde et al., 2023). TOM1L2 directly associates with the BBSome via its C-terminal domain, and several BBSome components are implicated in mediating this process (Shinde et al., 2023). Previous studies identified a consensus BBSome-binding motif, defined as a conserved lysine or arginine residue preceded by an aromatic residue ([W/F/Y][K/R]) in the cytoplasmic tails of BBSome-mediated cargoes (Klink et al., 2017; S. Yang et al., 2020). While the recognition of ubiquitinated chains by TOM1L2 and the subsequent binding of the BBSome are crucial for receptor removal from the cilium, the BBSome also directly interacts with its cargo: direct interaction modeling identified BBS7 as the subunit that recognizes the BBSome-binding motif in the cytoplasmic tail of SMO (Yang et al., 2020). Consistently, *Bbs7* knockout in MEF cells significantly reduces SMO retrieval from the cilium (Zhang et al., 2012a). However, despite the specific interaction described for BBS7 with SMO, my data, along with previous studies show that loss of several other BBSome units also results in increased ciliary SMO localization (Nozaki et al., 2018; Prasai et al.,

2020; Stubbs et al., 2023; Zhang et al., 2012a) (Fig. 35 a-b). Structurally, the interaction with SMO is facilitated by the β-propeller and coiled-coiled domain of BBS7 (S. Yang et al., 2020). BBS1, BBS2, and BBS9 share the β-propeller domain structure with BBS7 and may therefore also have the potential to bind this motif (Tian et al., 2023). Due to its unique domain structure, BBS8 is rather unlikely to bind SMO directly. Interestingly, the loss of BBS4, another TPR-containing subunit, also leads to increased ciliary SMO levels, suggesting a distinct role for this domain structure (Zhang et al., 2012a). TPR domains are important motifs for protein-protein interactions and are frequently found in multiprotein complexes, highlighting the central role of BBS8 within the BBSome and its importance in complex integrity (Das et al., 1998).

The absence of certain signaling receptors, such as the somatostatin receptor 3 (SSTR3), in some *Bbs* mutants led to a controversy about whether the BBSome also mediates ciliary entry of receptors (Berbari et al., 2008). Live-cell imaging has shown that activated GPCRs are packaged into extracellular vesicles, leading to their removal from the cilium along with bystander receptors (Nager et al., 2017). This offered an alternative mechanism by which the cilium eliminates activated receptors when BBSome-mediated retrieval fails. While I did not observe absence of receptors in *Bbs8*$^{-/-}$ cells *per se*, Christina Klausen in the Wachten lab demonstrated in her doctoral thesis that the Neuropeptide Y receptor Y2 (NPY2R) is absent from *Bbs8*-mutant neuronal cilia (Klausen, 2020). Therefore, cell type-specific differences need to be considered when investigating different *Bbs* mutants.

The fact that various BBSome mutants display a similar phenotype – increased ciliary SMO and GPR161 localization – suggests that the subunits are interdependent and function collectively in BBSome-mediated retrieval of cargo. The exact molecular mechanisms how BBS8 impacts BBSome integrity and function remain to be determined.

4.2 The role of Hh signaling in controlling cell fate

The Hh pathway plays a crucial role during development in orchestrating cell specification programs. In most adult tissues, the Hh signaling is only active in discrete stem- and progenitor-cell populations in various organs, including the brain, skin, or bladder, among others (Blanpain & Fuchs, 2009; Daynac et al., 2016; Pyczek et al., 2016; Shin et al., 2014; X. Sun et al., 2020). It remains not fully understood how Hh signaling in the adult

functions to control cell-fate specification. My results show that Hh signaling guides the identity of APCs in the WAT. Loss of BBS8 increased transcription of Hh target genes due to increased ciliary SMO localization at the basal state (Fig. 25 a, e). Ectopic activation of the Hh pathway reduces the P1 population in *Bbs8*$^{-/-}$ mice before the onset of obesity, thereby depleting the pool essential for tissue plasticity. Using a *Pdgfra*-conditional knockout model, I demonstrated that the effect is cell-autonomous and that the phenotype is driven by the *Pdgfra*-expressing APCs (Fig. 13 b). Single-cell analysis reveals an altered trajectory of *Bbs8*$^{-/-}$ P1 cells, showing a direct transition into fibrogenic progenitors (Fig. 19 i). In turn, fibrogenic CD9^{high} -expressing cells are increased in WAT of *Bbs8*$^{-/-}$ mice, which are characterized by their low adipogenic potential and inducing fibrotic remodeling of the tissue (Fig. 17 c-g). In the muscle, the fate of mesenchymal progenitors, so-called fibro-adipogenic progenitors (FAPs), has also been shown to be regulated by Hh signaling (Kopinke et al., 2017). Upon injury, FAPs promote muscle regeneration by supporting the recruitment and differentiation of MuSCs into myocytes. However, FAPs can also drive fatty degeneration and scarring of the muscle by undergoing adipogenesis or adopting a fibrogenic phenotype (Kopinke et al., 2017). Hh signaling modulates the balance between physiological and pathological outcomes. A short pulse of Hh pathway activation enhances myogenesis and promotes muscle regeneration, whereas sustained Hh signaling leads to extensive fibrosis (Kopinke et al., 2017). Additionally, the mechanism of Hh activation is relevant for the fate decision-making: Physiological activation by a Hh ligand drives muscle regeneration, while ectopic Hh activation upon loss of PTCH1 restricts muscle regeneration by pushing FAPs to adopt a myofibroblast fate (Norris et al., 2023). Thus, precise and temporal regulation of Hh signaling is essential for proper cell fate and function. Consistently, my results indicated that loss of BBS8 dysregulated Hh signaling and intrinsically altered the cell fate of APCs, pushing them towards a fibrogenic phenotype.

But how can Hh signaling influence different cell fates? Previous studies have established a connection between epithelial-to-mesenchymal transition (EMT) programs and Hh signaling (Guen et al., 2017; Omenetti et al., 2008; F. Wang et al., 2016). EMT is a biological process in which epithelial cells change their fate by acquiring an MSC phenotype, which is accompanied by cytoskeletal changes, loss of cell polarity, and altered cell-cell adhesion (J. Yang et al., 2020). Hh pathway activation coordinates

downstream signaling events via the GLI family transcription factors, which interact with each other and with co-regulators, thereby enabling various transcriptional responses based on the cellular and tissue context (Sigafoos et al., 2021). A direct target gene of GLI1, Snail, promotes EMT in basal cell carcinoma as well as during development (X. Li et al., 2006; Louro et al., 2002). Snail represses transcription of the cell adhesion molecule E-cadherin, leading to loss of cell polarity which initiates EMT (Lamouille et al., 2014). Thus, Hh signaling can directly regulate cell fate by altering cellular gene transcription programs.

In the retinal pigment epithelium (RPE), loss of BBS8 disrupts cell morphology and alter cell fate by inducing EMT (Schneider et al., 2021). Snail transcription progressively increases in *Bbs8*$^{-/-}$ RPE during postnatal development, suggesting that dysregulated Hh signaling influences RPE fate via the GLI1/Snail axis (Schneider et al., 2021). The role of Snail in MSC is less well studied. Snail expression seems to gradually decrease during adipogenic differentiation of 3T3-L1 cells and Snail directly binds to the E-box motif of the PPARγ promotor to inhibit adipogenesis (Lee et al., 2013). My findings showed that CD9^{high} cells were resistant to undergoing adipogenesis in response to cilia-specific cues (Fig. 17 f-g). Thus, investigating Snail transcription in CD9^{high} cells may help to understand whether the anti-adipogenic phenotype is also mediated via the GLI1/Snail axis. Another transcription factor that is regulated by Snail in 3T3-L1 cells is paired related homeobox 1 (PRRX1) (Peláez-García et al., 2015). Interestingly, PRRX1 has been described as a master regulator of myofibroblast lineage progression in cancer-associated fibroblasts (Lee et al., 2022). PRRX1 promotes lineage progression via the tumor growth factor β (TGFβ) signaling pathway (Lee et al., 2022). Indeed, Hh signaling is not the only pathway mediating fibrotic progression; rather, it acts in concert with other pathways, such as the TGFβ pathway or PDGFRα pathway (Contreras et al., 2019; Teves et al., 2019). The respective receptors for these pathways also localize to the cilium, opening different possibilities for the cell organelle to coordinate crosstalk between various signaling pathways to balance the biological output (Christensen et al., 2017). Crosstalk between the TGFβ pathway and Hh signaling was demonstrated when SMAD3, a downstream mediator of TGFβ signaling, activated GLI1 and GLI2 expression in fibroblasts, independent of Hh receptor engagement (Dennler et al., 2007). Conversely, *Tgfb* gene expression has been shown to be regulated by GLI2 in hepatic stellate cells (Yan et al.,

2021). Thus, cross-activation of the TGFβ pathway by ectopic Hh signaling may further drive the fibrogenic phenotype in APCs.

PDGFRα, a receptor tyrosine kinase, mediates various cellular functions through the mitogen-activated protein (MAP) kinase and phosphatidylinositol 3 kinase (PI3K). Enhancing PDGFRα tyrosine kinase via the D842V mutation drastically increases the number of the pro-fibrotic CD9^{high} cells in WAT and is proposed to drive this phenotypic switch (Iwayama et al., 2015; Marcelin et al., 2017). Given the role of the BBSome in mediating receptor export and the observation that loss of BBS8 results in increased receptor localization in the cilium, BBS8 may directly influence PDGFRα localization and, consequently, signaling. However, since the PDGFRα is a receptor tyrosine kinase, it is not typical cargo for the BBSome. Moreover, a study showed that mutations affecting the retrograde IFT machinery do not alter PDGFRα receptor levels in the cilium (Umberger & Caspary, 2015). While loss of BBS8 may not directly impact PDGFRα localization, experimental evidence supports crosstalk between the Hh- and PDGFRα-signaling pathways. During alveolar septum formation, these signaling pathways collectively support myofibroblast/fibroblast function (Yie et al., 2023). Here, inhibition of the Hh pathway leads to concomitant decrease of *Pdgfra* expression and directly alters expression of PDGF signaling target genes (Yie et al., 2023). It would be interesting to investigate whether the opposite effect – namely increased Hh signaling resulting in upregulated PDGFRα target gene expression – underlies the fate shift observed in *Bbs8*$^{-/-}$ APCs. Further studies will shed light on how Hh pathway activation, both alone and in combination with other pathways, remodels cell fate and function of APCs. Taken together, my data link aberrant Hh signaling with the loss of the stem cell identity with a shift towards a fibrogenic phenotype (Fig. 35).

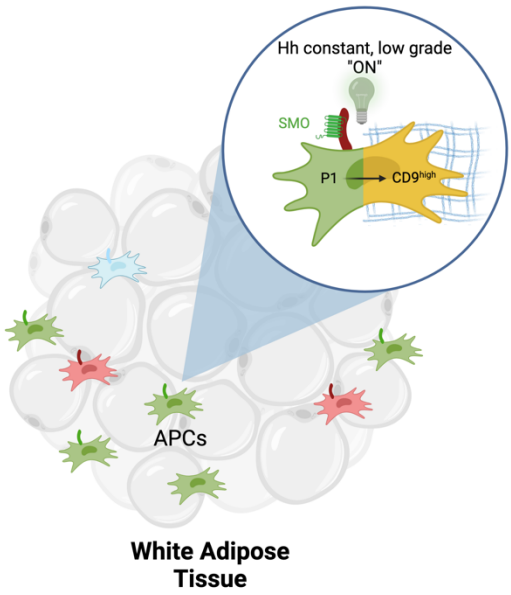

Fig. 35: Model of Hedgehog (Hh)-dependent, fibrogenic fate change in adipocyte precursor cells.

4.3. Fibrogenic remodeling in WAT of *Bbs8*$^{-/-}$ mice

In most diet-induced obesity models, prolonged overnutrition leads to hypoxia in WAT, which triggers chronic low-grade inflammation and upregulates ECM genes, ultimately promoting obesity-driven adipose tissue fibrosis (Debari & Abbott, 2020; Jääskeläinen et al., 2023). However, in *Bbs8*$^{-/-}$ mice, fibrotic remodeling was not a consequence of obesity but was already observed in the lean state, driven by *Pdgfra*-expressing cells (Fig. 16). A key question is how this early fibrogenic phenotype influences WAT remodeling during later stages of obesity.

Bbs8$^{-/-}$ mice developed obesity (Fig. 9 b-c), and other BBS mouse models show a similar phenotype, which is primarily driven by hyperphagia (Marion et al., 2012; Rahmouni et al., 2008). While a previous study reported hyperplasia-driven WAT expansion in *Bbs12*$^{-/-}$ mice (Marion et al., 2012), WAT expansion in *Bbs8*$^{-/-}$ mice occurred through hypertrophy (Fig. 11). This suggests that different BBSome components distinctly affect APC behavior. The loss of BBS4, BBS10, or BBS12 enhances APC proliferation and adipogenesis, promoting hyperplasia (Aksanov et al., 2014; Marion et al., 2008; Marion et al., 2012). In contrast, the loss of BBS8 induced ectopic Hh activation, which promoted a fibrogenic switch towards CD9^{high}-expressing cells and resulted in a depletion of the progenitor pool. A decreased progenitor pool at a pre-obese stage limits WAT expansion by hyperplasia during prolonged states of excess energy of hyperphagic *Bbs8*$^{-/-}$ mice. Instead, it shifts the balance towards hypertrophic expansion, which is typically associated with pathophysiological alterations of the tissue, as it limits oxygen diffusion, leading to adipocyte death which ultimately triggers a pro-inflammatory response (Lindhorst et al., 2021). However, Nora Winnerling demonstrated in her thesis that the WAT of *Bbs8*$^{-/-}$ mice remains relatively healthy during obesity, exhibiting minimal signs of adipocyte death and macrophage infiltration, as indicated by the scarcity of crown-like structures (Winnerling, 2022). Thus, other mechanisms may help to preserve adipose tissue functionality to combat the effects of the depleted progenitor pool.

The fibrogenic CD9^{high} population was resistant to adipogenesis (Fig. 17 f-g), in line with previous studies showing that the fibrogenic switch to CD9^{high} expression during obesity diminishes adipogenic potential (J. H. Lee et al., 2022; Marcelin et al., 2017). Therefore, these cells cannot take on the burden of excess energy, and other cells may need to

compensate by taking up more lipids. Interestingly, the *in vitro* lipidomics data showed an increase of total TAGs in *Bbs8*$^{-/-}$ cells during adipocyte maturation (Fig. 18 f-g). It remains unclear whether the increased lipid-uptake potential originates from APCs during late-stage adipogenesis or is facilitated by mature adipocytes. As adipocytes are not ciliated, loss of BBS8 might impact them in a non-ciliary fashion. Indeed, BBS proteins can localize to the nucleus and have been implicated in regulating gene expression (Ewerling et al., 2023; Gascue et al., 2012). Whether this plays a role in adipocytes needs to be investigated further. Nevertheless, the increased propensity to take up lipids further underlines the hypertrophic expansion of WAT of obese *Bbs8*$^{-/-}$ mice.

The fibrogenic fate change in *Bbs8*$^{-/-}$ APCs also led to increased ECM deposition, evidenced by an upregulation in collagen type I, fibronectin, and cross-linking enzymes (Fig. 16). While the ECM provides structural support at steady state, ECM components must be degraded and reassembled to accommodate tissue growth during WAT expansion. Excessive ECM deposition increases tissue stiffness, thereby restricting expansion and leading to ectopic lipid deposition (Gliniak et al., 2023). However, despite increased ECM deposition, *Bbs8*$^{-/-}$ mice exhibited significant WAT expandability during obesity progression (Fig. 9 d-e), suggesting a compensatory mechanism to allow tissue growth and to preserve tissue functionality. ECM degradation is regulated by matrix metalloproteinases (MMPs), which solubilize ECM components. MMP14, the predominant MMP in adipose tissue, modulates stiff pericellular collagens to facilitate adipocyte growth (Chun et al., 2010). Interestingly, overexpression of MMP14 at an early pre-obese stage prevents fibrosis and inflammation upon HFD feeding, likely by digesting dense ECM and thereby alleviating mechanical stress (X. Li et al., 2020). Interestingly, I observed increased expression of genes encoding for various *Mmps*, including *Mmp14*, in *Bbs8*$^{-/-}$ P1 cells compared to wild-type P1 cells (Fig. 36).

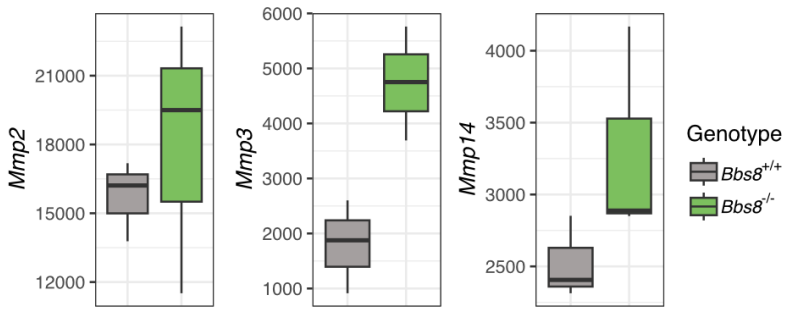

Fig. 36: *Matrix Metalloproteinase (Mmp)* expression in *Bbs8*$^{-/-}$ P1 cells. Expression level of various *Mmp* genes in *Bbs8*$^{+/+}$ and *Bbs8*$^{-/-}$ P1 APCs.

In turn, this may allow dynamic remodeling of the ECM in response to excess energy and would help to balance between increased ECM expression at an early stage and the demand for tissue expansion during obesity.

To combat hypoxia in expanding WAT, vascular adaptation is crucial for maintaining tissue homeostasis. Growth of new blood vessels (angiogenesis) supports healthy tissue expansion by supplying nutrients and oxygen while preventing hypoxia (Rupnick et al., 2002). My data indicated increased interaction between a specific P2 subcluster, P2_1, and endothelial cells via the upregulation of collagen and laminin pathways (Fig. 20 b). While little is known about APC-endothelial crosstalk during fibrotic remodeling, studies show that collagen- and integrin-interactions increase during obesity (Corvera et al., 2022; Reggio et al., 2016). Loss of BBS8 further increased the collagen- and laminin-interactions, suggesting that *Bbs8*$^{-/-}$ APCs behave similarly to progenitor cells found in obese tissue. The vascular endothelial growth factor (VEGF)/ VEGF-receptor system is the main regulator of angiogenesis in WAT and the contribution of APCs is essential for this process (Herold & Kalucka, 2021). Further studies should investigate whether the fibrogenic fate change in *Bbs8*$^{-/-}$ APCs also alters VEGF secretion and, consequently, the vascular-modulating capabilities of APCs, as this may provide crucial insights into adipose tissue health.

To counteract the fibrogenic fate change, I used vismodegib as a treatment to suppress ectopic Hh signaling, which concomitantly reduced the fibrogenic gene signature (Fig. 32 c). Vismodegib has already been shown to act as an anti-fibrotic drug by decreasing the population of liver myofibroblasts and attenuating early liver fibrosis through Hh signaling inhibition (Philips et al., 2011; Pratap et al., 2012). These findings suggest that targeting Hh signaling could be a promising strategy to remodel early-stage fibrosis during tissue remodeling in obesity.

5. Abstract

The primary cilium serves as a cellular antenna, transducing extracellular stimuli into an intracellular response. In white adipose tissue (WAT), adipocyte precursor cells (APCs) but not mature adipocytes display a primary cilium. APCs replenish the adipocyte pool by undergoing adipogenesis. Advances in single-cell analysis have revealed the heterogeneity of APCs as they consist of multiple functionally distinct subpopulations in the WAT. The regulation of cell fate and differentiation of APCs is key to maintaining WAT homeostasis. Primary cilia have been proposed to regulate APC function and, thereby, WAT physiology. The role of cilia in regulating whole-body energy metabolism is also reflected in the Bardet-Biedl syndrome (BBS), where primary cilia dysfunction leads to obesity due to hyperphagia and WAT remodeling. However, how ciliary signaling might impact APC fate decision making is not known.

To address that, I comprehensively investigated the APC subpopulations in WAT under physiological conditions and during primary cilia dysfunction in a BBS mouse model before the onset of obesity. In mice that recapitulated the ciliopathy BBS (*Bbs8*$^{-/-}$), I demonstrated that loss of BBS8 reduced the stem cell-like P1 APC subpopulation due to a phenotypic switch towards a fibrogenic phenotype. This was accompanied by extracellular matrix remodeling of the WAT and an increase of the profibrotic CD9^{high} APC subpopulation. Single-cell RNA sequencing revealed an altered trajectory of *Bbs8*$^{-/-}$ cells, as they directly transitioned into fibrogenic progenitors, bypassing the committed P2 APCs. Ciliary hedgehog (Hh) signaling emerged as a central driver of the molecular changes in *Bbs8*$^{-/-}$ APCs. Controlled activation of the Hh pathway is essential for maintaining stem cell fates. However, loss of BBS8 promoted ectopic Hh activation in APCs and, in turn, induced the fibrogenic fate change.

These findings reveal a novel role of primary cilia in APC fate determination, balancing adipogenesis and fibrogenesis. The identified molecular mechanisms can serve as a basis to refine potential therapeutic targets for obesity.

6. List of figures

7. List of tables

8. References

Ahmadian, M., Duncan, R. E., Jaworski, K., Sarkadi-Nagy, E., & Sul, H. S. (2007). Triacylglycerol metabolism in adipose tissue. In *Future Lipidology* (Vol. 2, Issue 2, pp. 229–237). https://doi.org/10.2217/17460875.2.2.229

Aksanov, O., Green, P., & Birk, R. Z. (2014). BBS4 directly affects proliferation and differentiation of adipocytes. *Cellular and Molecular Life Sciences*, *71*(17), 3381–3392. https://doi.org/10.1007/s00018-014-1571-x

Ansley, S. J., Badano, J. L., Blacque, O. E., Hill, J., Hoskins, B. E., Leitch, C. C., Kim, J. C., Ross, A. J., Eichers, E. R., Teslovich, T. M., Mah, A. K., Johnsen, R. C., Cavender, J. C., Lewis, R. A., Leroux, M. R., Beales, P. L., & Katsanis, N. (2003). Basal body dysfunction is a likely cause of pleiotropic Bardet-Biedl syndrome. *Nature*, *425*(6958). https://doi.org/10.1038/nature02030

Armas-López, L., Zúñiga, J., Arrieta, O., & Ávila-Moreno, F. (2017). *The Hedgehog-GLI pathway in embryonic development and cancer: implications for pulmonary oncology therapy* (Vol. 8, Issue 36). www.impactjournals.com/oncotarget

Ayers, K. L., Glicksberg, B. S., Garfield, A. S., Longerich, S., White, J. A., Yang, P., Du, L., Chittenden, T. W., Gulcher, J. R., Roy, S., Fiedorek, F., Gottesdiener, K., Cohen, S., North, K. E., Schadt, E. E., Li, S. D., Chen, R., & Van Der Ploeg, L. H. T. (2018). Melanocortin 4 Receptor Pathway Dysfunction in Obesity: Patient Stratification Aimed at MC4R Agonist Treatment. *Journal of Clinical Endocrinology and Metabolism*, *103*(7), 2601–2612. https://doi.org/10.1210/jc.2018-00258

Badgandi, H. B., Hwang, S. H., Shimada, I. S., Loriot, E., & Mukhopadhyay, S. (2017). Tubby family proteins are adapters for ciliary trafficking of integral membrane proteins. *The Journal of Cell Biology*, *216*(3), 743–760. https://doi.org/10.1083/jcb.201607095

Barak, Y., Nelson, M. C., Ong, E. S., Jones, Y. Z., Ruiz-Lozano, P., Chien, K. R., Koder, A., & Evans, R. M. (1999). PPARγ Is Required for Placental, Cardiac, and Adipose Tissue Development. *Molecular Cell*, *4*(4), 585–595. https://doi.org/10.1016/S1097-2765(00)80209-9

Bear, R. M., & Caspary, T. (2024). Uncovering cilia function in glial development. In *Annals of Human Genetics* (Vol. 88, Issue 1, pp. 27–44). John Wiley and Sons Inc. https://doi.org/10.1111/ahg.12519

Behnke, O., & Forer, A. (1967). Evidence for four classes of microtubules in individual cells. *Journal of Cell Science*, *2*(2), 169–192. https://doi.org/10.1242/jcs.2.2.169

Berbari, N. F., Lewis, J. S., Bishop, G. A., Askwith, C. C., & Mykytyn, K. (2008). *Bardet-Biedl syndrome proteins are required for the localization of G protein-coupled receptors to primary cilia*. www.pnas.org/cgi/content/full/

Berry, R., & Rodeheffer, M. S. (2013). Characterization of the adipocyte cellular lineage in vivo. *Nature Cell Biology*, *15*(3), 302–308. https://doi.org/10.1038/ncb2696

Bisgrove, B. W., & Yost, H. J. (2006). The roles of cilia in developmental disorders and disease. In *Development* (Vol. 133, Issue 21, pp. 4131–4143). https://doi.org/10.1242/dev.02595

Blanpain, C., & Fuchs, E. (2009). Epidermal homeostasis: A balancing act of stem cells in the skin. In *Nature Reviews Molecular Cell Biology* (Vol. 10, Issue 3, pp. 207–217). Nature Publishing Group. https://doi.org/10.1038/nrm2636

Bradshaw, A. D., & Sage, E. H. (2001). SPARC, a matricellular protein that functions in cellular differentiation and tissue response to injury. In *Journal of Clinical Investigation* (Vol. 107, Issue 9). https://doi.org/10.1172/JCI12939

Brown, D. C., & Gatter, K. C. (2002). Ki67 protein: the immaculate deception? *Histopathology*, *40*(1), 2–11. https://doi.org/https://doi.org/10.1046/j.1365-2559.2002.01343.x

Brown, J. A. L., Santra, T., Owens, P., Barry, F., & Morrison, A. M. (2014). Primary cilium-associated genes mediate bone marrow stromal cell response to hypoxia. *Stem Cell Research*, *13*(2), 284–299. https://doi.org/10.1016/j.scr.2014.06.006

Brun, C. E., Sincennes, M. C., Lin, A. Y. T., Hall, D., Jarassier, W., Feige, P., Le Grand, F., & Rudnicki, M. A. (2022). GLI3 regulates muscle stem cell entry into GAlert and self-renewal. *Nature Communications*, *13*(1). https://doi.org/10.1038/s41467-022-31695-5

Burl, R. B., Ramseyer, V. D., Rondini, E. A., Pique-Regi, R., Lee, Y. H., & Granneman, J. G. (2018). Deconstructing Adipogenesis Induced by β3-Adrenergic Receptor

Activation with Single-Cell Expression Profiling. *Cell Metabolism*, *28*(2), 300-309.e4. https://doi.org/10.1016/j.cmet.2018.05.025

Cao, Z., Umek, R. M., & Mcknight, S. L. (1991). *Regulated expression of three C/EBP Isoforms during adipose conversion of 3T3-L1 cells*.

Cardoso, F., Klein Wolterink, R. G. J., Godinho-Silva, C., Domingues, R. G., Ribeiro, H., da Silva, J. A., Mahú, I., Domingos, A. I., & Veiga-Fernandes, H. (2021). Neuro-mesenchymal units control ILC2 and obesity via a brain–adipose circuit. *Nature*, *597*(7876), 410–414. https://doi.org/10.1038/s41586-021-03830-7

Carnicero, H. H. (1984). Changes in the metabolism of long chain fatty acids during adipose differentiation of 3T3 L1 cells. *Journal of Biological Chemistry*, *259*(6), 3844–3850. https://doi.org/10.1016/s0021-9258(17)43174-7

Chakrabarti, S., Hoque, M., Jamil, N. Z., Singh, V. J., Pollacksmith, D., Meer, N., & Pezzano, M. T. (2022). Bone Marrow-Derived Cells Contribute to the Maintenance of Thymic Stroma including TECs. *Journal of Immunology Research*, *2022*. https://doi.org/10.1155/2022/6061746

Chaudhry, P., Singh, M., Triche, T. J., Guzman, M., & Merchant, A. A. (2017). GLI3 repressor determines Hedgehog pathway activation and is required for response to SMO antagonist glasdegib in AML. *Blood*, *129*(26), 3465–3475. https://doi.org/10.1182/blood-2016-05-718585

Chen, J. K., Taipale, J., Young, K. E., Maiti, T., & Beachy, P. A. (2002). Small molecule modulation of smoothened activity. *Proceedings of the National Academy of Sciences of the United States of America*, *99*(22). https://doi.org/10.1073/pnas.182542899

Chiang, C., Litingtung, Y., Lee, E., Youngt, K. E., Cordent, J. L., Westphal, H., & Beachyt, P. A. (1996). *Cyclopia and defective axial patterning in mice lacking Sonic hedgehog gene function*.

Chirgwin, J. M., Przybyla, A. E., MacDonald, R. J., & Rutter, W. J. (1979). Isolation of Biologically Active Ribonucleic Acid from Sources Enriched in Ribonuclease. *Biochemistry*, *18*(24). https://doi.org/10.1021/bi00591a005

Cho, D. S., Lee, B., & Doles, J. D. (2019). Refining the adipose progenitor cell landscape in healthy and obese visceral adipose tissue using single-cell gene

expression profiling. *Life Science Alliance*, *2*(6). https://doi.org/10.26508/lsa.201900561

Chou, H. T., Apelt, L., Farrell, D. P., White, S. R., Woodsmith, J., Svetlov, V., Goldstein, J. S., Nager, A. R., Li, Z., Muller, J., Dollfus, H., Nudler, E., Stelzl, U., DiMaio, F., Nachury, M. V., & Walz, T. (2019). The Molecular Architecture of Native BBSome Obtained by an Integrated Structural Approach. *Structure*, *27*(9), 1384-1394.e4. https://doi.org/10.1016/j.str.2019.06.006

Christensen, S. T., Morthorst, S. K., Mogensen, J. B., & Pedersen, L. B. (2017). Primary cilia and coordination of receptor tyrosine kinase (RTK) and transforming growth factor β (TGF-β) signaling. In *Cold Spring Harbor Perspectives in Biology* (Vol. 9, Issue 6). Cold Spring Harbor Laboratory Press. https://doi.org/10.1101/cshperspect.a028167

Christodoulides, C., Lagathu, C., Sethi, J. K., & Vidal-Puig, A. (2009). Adipogenesis and WNT signalling. In *Trends in Endocrinology and Metabolism* (Vol. 20, Issue 1, pp. 16–24). https://doi.org/10.1016/j.tem.2008.09.002

Chun, T. H., Inoue, M., Morisaki, H., Yamanaka, I., Miyamoto, Y., Okamura, T., Sato-Kusubata, K., & Weiss, S. J. (2010). Genetic link between obesity and MMP14-dependent adipogenic collagen turnover. *Diabetes*, *59*(10), 2484–2494. https://doi.org/10.2337/db10-0073

Cignarelli, A., Genchi, V. A., Perrini, S., Natalicchio, A., Laviola, L., & Giorgino, F. (2019). Insulin and insulin receptors in adipose tissue development. In *International Journal of Molecular Sciences* (Vol. 20, Issue 3). MDPI AG. https://doi.org/10.3390/ijms20030759

Coleman, J. L. J., Brennan, K., Ngo, T., Balaji, P., Graham, R. M., & Smith, N. J. (2015). Rapid knockout and reporter mouse line generation and breeding colony establishment using EUCOMM conditional-ready embryonic stem cells: A case study. *Frontiers in Endocrinology*, *6*(JUN). https://doi.org/10.3389/fendo.2015.00105

Conkar, D., & Firat-Karalar, E. N. (2021). Microtubule-associated proteins and emerging links to primary cilium structure, assembly, maintenance, and disassembly. In *FEBS Journal* (Vol. 288, Issue 3, pp. 786–798). Blackwell Publishing Ltd. https://doi.org/10.1111/febs.15473

Contreras, O., Cruz-Soca, M., Theret, M., Soliman, H., Tung, L. W., Groppa, E., Rossi, F. M., & Brandan, E. (2019). Cross-talk between TGF-β and PDGFRα signaling pathways regulates the fate of stromal fibro-adipogenic progenitors. *Journal of Cell Science*, *132*(19). https://doi.org/10.1242/jcs.232157

Cook, L. B., Ophardt, H. D., Shen, R., Pratt, B. H., & Galbier, L. A. (2021). Transcriptome analysis of ciliary-dependent MCH signaling in differentiating 3T3-L1 pre-adipocytes. *Scientific Reports*, *11*(1). https://doi.org/10.1038/s41598-021-84138-4

Corvera, S., Solivan-Rivera, J., & Yang Loureiro, Z. (2022). Angiogenesis in adipose tissue and obesity. In *Angiogenesis* (Vol. 25, Issue 4, pp. 439–453). Springer Science and Business Media B.V. https://doi.org/10.1007/s10456-022-09848-3

Creanga, A., Glenn, T. D., Mann, R. K., Saunders, A. M., Talbot, W. S., & Beachy, P. A. (2012). Scube/You activity mediates release of dually lipid-modified Hedgehog signal in soluble form. *Genes and Development*, *26*(12). https://doi.org/10.1101/gad.191866.112

Crompton, T., Outram, S. V., & Hager-Theodorides, A. L. (2007). Sonic hedgehog signalling in T-cell development and activation. In *Nature Reviews Immunology* (Vol. 7, Issue 9). https://doi.org/10.1038/nri2151

Das, A. K., Cohen, P. W., & Barford, D. (1998). The structure of the tetratricopeptide repeats of protein phosphatase 5: implications for TPR-mediated protein-protein interactions. In *The EMBO Journal* (Vol. 17, Issue 5).

Daynac, M., Tirou, L., Faure, H., Mouthon, M. A., Gauthier, L. R., Hahn, H., Boussin, F. D., & Ruat, M. (2016). Hedgehog Controls Quiescence and Activation of Neural Stem Cells in the Adult Ventricular-Subventricular Zone. *Stem Cell Reports*, *7*(4), 735–748. https://doi.org/10.1016/j.stemcr.2016.08.016

Dean, S., Moreira-Leite, F., Varga, V., & Gull, K. (2016). Cilium transition zone proteome reveals compartmentalization and differential dynamics of ciliopathy complexes. *Proceedings of the National Academy of Sciences of the United States of America*, *113*(35), E5135–E5143. https://doi.org/10.1073/pnas.1604258113

Debari, M. K., & Abbott, R. D. (2020). Adipose tissue fibrosis: Mechanisms, models, and importance. In *International Journal of Molecular Sciences* (Vol. 21, Issue 17, pp. 1–24). MDPI AG. https://doi.org/10.3390/ijms21176030

Dennler, S., André, J., Alexaki, I., Li, A., Magnaldo, T., Ten Dijke, P., Wang, X. J., Verrecchia, F., & Mauviel, A. (2007). Induction of sonic hedgehog mediators by transforming growth factor-β: Smad3-dependent activation of Gli2 and Gli1 expression in vitro and in vivo. *Cancer Research*, *67*(14), 6981–6986. https://doi.org/10.1158/0008-5472.CAN-07-0491

Deretic, J., Odabasi, E., & Firat-Karalar, E. N. (2023). The multifaceted roles of microtubule-associated proteins in the primary cilium and ciliopathies. In *Journal of Cell Science* (Vol. 136, Issue 23). Company of Biologists Ltd. https://doi.org/10.1242/jcs.261148

Deshpande, I., Liang, J., Hedeen, D., Roberts, K. J., Zhang, Y., Ha, B., Latorraca, N. R., Faust, B., Dror, R. O., Beachy, P. A., Myers, B. R., & Manglik, A. (2019). Smoothened stimulation by membrane sterols drives Hedgehog pathway activity. *Nature*, *571*(7764), 284–288. https://doi.org/10.1038/s41586-019-1355-4

Dilan, T. L., Singh, R. K., Saravanan, T., Moye, A., Goldberg, A. F. X., Stoilov, P., & Ramamurthy, V. (2018). Bardet-Biedl syndrome-8 (BBS8) protein is crucial for the development of outer segments in photoreceptor neurons. *Human Molecular Genetics*, *27*(2), 283–294. https://doi.org/10.1093/hmg/ddx399

Divoux, A., Tordjman, J., Lacasa, D., Veyrie, N., Hugol, D., Aissat, A., Basdevant, A., Guerre-Millo, M., Poitou, C., Zucker, J. D., Bedossa, P., & Clément, K. (2010). Fibrosis in human adipose tissue: Composition, distribution, and link with lipid metabolism and fat mass loss. *Diabetes*, *59*(11), 2817–2825. https://doi.org/10.2337/db10-0585

Dobin, A., Davis, C. A., Schlesinger, F., Drenkow, J., Zaleski, C., Jha, S., Batut, P., Chaisson, M., & Gingeras, T. R. (2013). STAR: Ultrafast universal RNA-seq aligner. *Bioinformatics*, *29*(1). https://doi.org/10.1093/bioinformatics/bts635

Dobrzanski, P., Noguchi, T., Kovary, K., Rizzo, C. A., Lazo, P. S., & Bravo, R. (1991). Both Products of the fos B Gene, FosB and Its Short Form, FosB/SF, Are Transcriptional Activators in Fibroblasts . *Molecular and Cellular Biology*, *11*(11). https://doi.org/10.1128/mcb.11.11.5470-5478.1991

Doheny, D., Manore, S. G., Wong, G. L., & Lo, H. W. (2020). Hedgehog signaling and truncated gli1 in cancer. In *Cells* (Vol. 9, Issue 9, pp. 1–31). Multidisciplinary Digital Publishing Institute (MDPI). https://doi.org/10.3390/cells9092114

Domire, J. S., Green, J. A., Lee, K. G., Johnson, A. D., Askwith, C. C., & Mykytyn, K. (2011). Dopamine receptor 1 localizes to neuronal cilia in a dynamic process that requires the Bardet-Biedl syndrome proteins. *Cellular and Molecular Life Sciences*, *68*(17), 2951–2960. https://doi.org/10.1007/s00018-010-0603-4

Dong, H., Sun, W., Shen, Y., Baláz, M., Balázová, L., Ding, L., Löffler, M., Hamilton, B., Klöting, N., Blüher, M., Neubauer, H., Klein, H., & Wolfrum, C. (2022). Identification of a regulatory pathway inhibiting adipogenesis via RSPO2. *Nature Metabolism*, *4*(1), 90–105. https://doi.org/10.1038/s42255-021-00509-1

Ewels, P. A., Peltzer, A., Fillinger, S., Patel, H., Alneberg, J., Wilm, A., Garcia, M. U., Di Tommaso, P., & Nahnsen, S. (2020). The nf-core framework for community-curated bioinformatics pipelines. In *Nature Biotechnology* (Vol. 38, Issue 3). https://doi.org/10.1038/s41587-020-0439-x

Ewerling, A., Maissl, V., Wickstead, B., & May-Simera, H. L. (2023). Neofunctionalization of ciliary BBS proteins to nuclear roles is likely a frequent innovation across eukaryotes. *IScience*, *26*(4). https://doi.org/10.1016/j.isci.2023.106410

Fabian, S. L., Penchev, R. R., St-Jacques, B., Rao, A. N., Sipil, P., West, K. A., McMahon, A. P., & Humphreys, B. D. (2012). Hedgehog-Gli pathway activation during kidney fibrosis. *American Journal of Pathology*, *180*(4), 1441–1453. https://doi.org/10.1016/j.ajpath.2011.12.039

Fan, Y., Esmail, M. A., Ansley, S. J., Blacque, O. E., Boroevich, K., Ross, A. J., Moore, S. J., Badano, J. L., May-Simera, H., Compton, D. S., Green, J. S., Lewis, R. A., Van Haelst, M. M., Parfrey, P. S., Baillie, D. L., Beales, P. L., Katsanis, N., Davidson, W. S., & Leroux, M. R. (2004). Mutations in a member of the Ras superfamily of small GTP-binding proteins causes Bardet-Biedl syndrome. *Nature Genetics*, *36*(9), 989–993. https://doi.org/10.1038/ng1414

Farag, T. I., & Teebi, A. S. (1989). High incidence of Bardet Biedl syndrome among the Bedouin. *Clinical Genetics*, *36*(6), 463–464. https://doi.org/https://doi.org/10.1111/j.1399-0004.1989.tb03378.x

Felix, J. B., Cox, A. R., & Hartig, S. M. (2021). Acetyl-CoA and Metabolite Fluxes Regulate White Adipose Tissue Expansion. In *Trends in Endocrinology and Metabolism* (Vol. 32, Issue 5). https://doi.org/10.1016/j.tem.2021.02.008

Ferrero, R., Rainer, P., & Deplancke, B. (2020). Toward a Consensus View of Mammalian Adipocyte Stem and Progenitor Cell Heterogeneity. In *Trends in Cell Biology* (Vol. 30, Issue 12, pp. 937–950). Elsevier Ltd. https://doi.org/10.1016/j.tcb.2020.09.007

Foglia, B., Cannito, S., Bocca, C., Parola, M., & Novo, E. (2019). ERK pathway in activated, myofibroblast-like, hepatic stellate cells: A critical signaling crossroad sustaining liver fibrosis. In *International Journal of Molecular Sciences* (Vol. 20, Issue 11). MDPI AG. https://doi.org/10.3390/ijms20112700

Fontaine, C., Cousin, W., Plaisant, M., Dani, C., & Peraldi, P. (2008). Hedgehog Signaling Alters Adipocyte Maturation of Human Mesenchymal Stem Cells. *Stem Cells*, *26*(4), 1037–1046. https://doi.org/10.1634/stemcells.2007-0974

Forcioli-Conti, N., Lacas-Gervais, S., Dani, C., & Peraldi, P. (2015). The primary cilium undergoes dynamic size modifications during adipocyte differentiation of human adipose stem cells. *Biochemical and Biophysical Research Communications*, *458*(1), 117–122. https://doi.org/10.1016/j.bbrc.2015.01.078

Forsythe, E., & Beales, P. L. (2013). Bardet-Biedl syndrome. *European Journal of Human Genetics*, *21*(1), 8–13. https://doi.org/10.1038/ejhg.2012.115

Galindo, E. P. (2024). *The role of primary cilia in controlling metaflammation*.

Garamszegi, N., Garamszegi, S. P., Samavarchi-Tehrani, P., Walford, E., Schneiderbauer, M. M., Wrana, J. L., & Scully, S. P. (2010). Extracellular matrix-induced transforming growth factor-B receptor signaling dynamics. *Oncogene*, *29*(16), 2368–2380. https://doi.org/10.1038/onc.2009.514

Garcia, G., Raleigh, D. R., & Reiter, J. F. (2018). How the Ciliary Membrane Is Organized Inside-Out to Communicate Outside-In. In *Current Biology* (Vol. 28, Issue 8, pp. R421–R434). Cell Press. https://doi.org/10.1016/j.cub.2018.03.010

Garcia-Gonzalo, F. R., & Reiter, J. F. (2017). Open Sesame: How transition fibers and the transition zone control ciliary composition. *Cold Spring Harbor Perspectives in Biology*, *9*(2). https://doi.org/10.1101/cshperspect.a028134

Gascue, C., Tan, P. L., Cardenas-Rodriguez, M., Libisch, G., Fernandez-Calero, T., Liu, Y. P., Astrada, S., Robello, C., Naya, H., Katsanis, N., & Badano, J. L. (2012). Direct role of Bardet-Biedl syndrome proteins in transcriptional regulation. *Journal of Cell Science*, *125*(2), 362–375. https://doi.org/10.1242/jcs.089375

Ghaben, A. L., & Scherer, P. E. (2019). Adipogenesis and metabolic health. In *Nature Reviews Molecular Cell Biology* (Vol. 20, Issue 4, pp. 242–258). Nature Publishing Group. https://doi.org/10.1038/s41580-018-0093-z

Gierahn, T. M., Wadsworth, M. H., Hughes, T. K., Bryson, B. D., Butler, A., Satija, R., Fortune, S., Christopher Love, J., & Shalek, A. K. (2017). Seq-Well: Portable, low-cost rna sequencing of single cells at high throughput. *Nature Methods*, *14*(4). https://doi.org/10.1038/nmeth.4179

Gliniak, C. M., Pedersen, L., & Scherer, P. E. (2023). Adipose tissue fibrosis: the unwanted houseguest invited by obesity. In *Journal of Endocrinology* (Vol. 259, Issue 3). BioScientifica Ltd. https://doi.org/10.1530/JOE-23-0180

Gopalakrishnan, J., Feistel, K., Friedrich, B. M., Grapin-Botton, A., Jurisch-Yaksi, N., Mass, E., Mick, D. U., Müller, R., May-Simera, H., Schermer, B., Schmidts, M., Walentek, P., & Wachten, D. (2023). Emerging principles of primary cilia dynamics in controlling tissue organization and function. *The EMBO Journal*, *42*(21). https://doi.org/10.15252/embj.2023113891

Green, H., & Meuth, M. (1974). An Established Pre-Adipose Cell Line and its Differentiation in Culture. In *Cell* (Vol. 3).

Guen, V. J., Chavarria, T. E., Kröger, C., Ye, X., Weinberg, R. A., & Lees, J. A. (2017). EMT programs promote basal mammary stem cell and tumor-initiating cell stemness by inducing primary ciliogenesis and Hedgehog signaling. *Proceedings of the National Academy of Sciences of the United States of America*, *114*(49), E10532–E10539. https://doi.org/10.1073/pnas.1711534114

Guo, D. F., Cui, H., Zhang, Q., Morgan, D. A., Thedens, D. R., Nishimura, D., Grobe, J. L., Sheffield, V. C., & Rahmouni, K. (2016). The BBSome Controls Energy Homeostasis by Mediating the Transport of the Leptin Receptor to the Plasma Membrane. *PLoS Genetics*, *12*(2). https://doi.org/10.1371/journal.pgen.1005890

Guo, D. F., Lin, Z., Wu, Y., Searby, C., Thedens, D. R., Richerson, G. B., Usachev, Y. M., Grobe, J. L., Sheffield, V. C., & Rahmouni, K. (2019). The BBSome in POMC and AgRP neurons is necessary for body weight regulation and sorting of metabolic receptors. *Diabetes*, *68*(8), 1591–1603. https://doi.org/10.2337/db18-1088

Gupta, R. K., Mepani, R. J., Kleiner, S., Lo, J. C., Khandekar, M. J., Cohen, P., Frontini, A., Bhowmick, D. C., Ye, L., Cinti, S., & Spiegelman, B. M. (2012). Zfp423

expression identifies committed preadipocytes and localizes to adipose endothelial and perivascular cells. *Cell Metabolism*, *15*(2). https://doi.org/10.1016/j.cmet.2012.01.010

Gurnell, M., Savage, D. B., Chatterjee, V. K. K., & O'Rahilly, S. (2003). The Metabolic Syndrome: Peroxisome Proliferator-Activated Receptor γ and Its Therapeutic Modulation. *The Journal of Clinical Endocrinology & Metabolism*, *88*(6), 2412–2421. https://doi.org/10.1210/jc.2003-030435

Hansen, J. N., Rassmann, S., Stüven, B., Jurisch-Yaksi, N., & Wachten, D. (2021). CiliaQ: a simple, open-source software for automated quantification of ciliary morphology and fluorescence in 2D, 3D, and 4D images. *European Physical Journal E*, *44*(2). https://doi.org/10.1140/epje/s10189-021-00031-y

Hepler, C., Shan, B., Zhang, Q., Henry, G. H., Shao, M., Vishvanath, L., Ghaben, A. L., Mobley, A. B., Strand, D., Hon, G. C., & Gupta, R. K. (2018). Identification of functionally distinct fibro-inflammatory and adipogenic stromal subpopulations in visceral adipose tissue of adult mice. *ELife*, *7*. https://doi.org/10.7554/eLife.39636

Herold, J., & Kalucka, J. (2021). Angiogenesis in Adipose Tissue: The Interplay Between Adipose and Endothelial Cells. In *Frontiers in Physiology* (Vol. 11). Frontiers Media S.A. https://doi.org/10.3389/fphys.2020.624903

Hildebrandt, F., Benzing, T., & Katsanis, N. (2011). Ciliopathies. *New England Journal of Medicine*, *364*(16), 1533–1543. https://doi.org/10.1056/nejmra1010172

Hildreth, A. D., Ma, F., Wong, Y. Y., Sun, R., Pellegrini, M., & O'Sullivan, T. E. (2021). Single-cell sequencing of human white adipose tissue identifies new cell states in health and obesity. *Nature Immunology*, *22*(5), 639–653. https://doi.org/10.1038/s41590-021-00922-4

Hilgendorf, K. I., Johnson, C. T., Mezger, A., Rice, S. L., Norris, A. M., Demeter, J., Greenleaf, W. J., Reiter, J. F., Kopinke, D., & Jackson, P. K. (2019). Omega-3 Fatty Acids Activate Ciliary FFAR4 to Control Adipogenesis. *Cell*, *179*(6), 1289-1305.e21. https://doi.org/10.1016/j.cell.2019.11.005

Hill, D. A., Lim, H. W., Kim, Y. H., Ho, W. Y., Foong, Y. H., Nelson, V. L., Nguyen, H. C. B., Chegireddy, K., Kim, J., Habertheuer, A., Vallabhajosyula, P., Kambayashi, T., Won, K. J., & Lazar, M. A. (2018). Distinct macrophage populations direct inflammatory versus physiological changes in adipose tissue. *Proceedings of the*

National Academy of Sciences of the United States of America, *115*(22). https://doi.org/10.1073/pnas.1802611115

Hjortshøj, T. D., Gronskov, K., Philp, A. R., Nishimura, D. Y., Adeyemo, A., Rotimi, C. N., Sheffield, V. C., Rosenberg, T., & Brøndum-Nielsen, K. (2008). Novel mutations in BBS5 highlight the importance of this gene in non-caucasian Bardet-Biedl syndrome patients [3]. In *American Journal of Medical Genetics, Part A* (Vol. 146, Issue 4, pp. 517–520). https://doi.org/10.1002/ajmg.a.32136

Hu, S., Xiao, Q., Gao, R., Qin, J., Nie, J., Chen, Y., Lou, J., Ding, M., Pan, Y., & Wang, S. (2024). Identification of BGN positive fibroblasts as a driving factor for colorectal cancer and development of its related prognostic model combined with machine learning. *BMC Cancer*, *24*(1). https://doi.org/10.1186/s12885-024-12251-4

Hu, Y., Peng, L., Zhuo, X., Yang, C., & Zhang, Y. (2024). Hedgehog Signaling Pathway in Fibrosis and Targeted Therapies. In *Biomolecules* (Vol. 14, Issue 12). Multidisciplinary Digital Publishing Institute (MDPI). https://doi.org/10.3390/biom14121485

Huang, P., Wierbowski, B. M., Lian, T., Chan, C., García-Linares, S., Jiang, J., & Salic, A. (2022). Structural basis for catalyzed assembly of the Sonic hedgehog–Patched1 signaling complex. *Developmental Cell*, *57*(5), 670-685.e8. https://doi.org/10.1016/j.devcel.2022.02.008

Hughes, T. K., Wadsworth, M. H., Gierahn, T. M., Do, T., Weiss, D., Andrade, P. R., Ma, F., de Andrade Silva, B. J., Shao, S., Tsoi, L. C., Ordovas-Montanes, J., Gudjonsson, J. E., Modlin, R. L., Love, J. C., & Shalek, A. K. (2020). Second-Strand Synthesis-Based Massively Parallel scRNA-Seq Reveals Cellular States and Molecular Features of Human Inflammatory Skin Pathologies. *Immunity*, *53*(4). https://doi.org/10.1016/j.immuni.2020.09.015

Hwang, B., Lee, J. H., & Bang, D. (2018). Single-cell RNA sequencing technologies and bioinformatics pipelines. In *Experimental and Molecular Medicine* (Vol. 50, Issue 8). https://doi.org/10.1038/s12276-018-0071-8

Imbeault, P., Lemieux, S., Prud'homme, D., Tremblay, A., Nadeau, A., Després, J. P., & Mauriège, P. (1999). Relationship of visceral adipose tissue to metabolic risk factors for coronary heart disease: Is there a contribution of subcutaneous fat cell

hypertrophy? *Metabolism: Clinical and Experimental*, *48*(3). https://doi.org/10.1016/S0026-0495(99)90085-9

Iwayama, T., Steele, C., Yao, L., Dozmorov, M. G., Karamichos, D., Wren, J. D., & Olson, L. E. (2015). PDGFRα signaling drives adipose tissue fibrosis by targeting progenitor cell plasticity. *Genes and Development*, *29*(11), 1106–1119. https://doi.org/10.1101/gad.260554.115

Jääskeläinen, I., Petäistö, T., Mirzarazi Dahagi, E., Mahmoodi, M., Pihlajaniemi, T., Kaartinen, M. T., & Heljasvaara, R. (2023). Collagens Regulating Adipose Tissue Formation and Functions. In *Biomedicines* (Vol. 11, Issue 5). MDPI. https://doi.org/10.3390/biomedicines11051412

James, A. W., Leucht, P., Levi, B., Carre, A. L., Xu, Y., Helms, J. A., & Longaker, M. T. (2010). *Sonic Hedgehog Influences the Balance of Osteogenesis and Adipogenesis in Mouse Adipose-Derived Stromal Cells*. https://doi.org/10.1089/ten.tea.2010.0048

Januszyk, M., Rennert, R., Sorkin, M., Maan, Z., Wong, L., Whittam, A., Whitmore, A., Duscher, D., & Gurtner, G. (2015). Evaluating the Effect of Cell Culture on Gene Expression in Primary Tissue Samples Using Microfluidic-Based Single Cell Transcriptional Analysis. *Microarrays*, *4*(4). https://doi.org/10.3390/microarrays4040540

Jenkinson, E. J., & Anderson, G. (1994). Fetal thymic organ cultures. In *Current Opinion in Immunology* (Vol. 6).

Jin, H., White, S. R., Shida, T., Schulz, S., Aguiar, M., Gygi, S. P., Bazan, J. F., & Nachury, M. V. (2010). The conserved bardet-biedl syndrome proteins assemble a coat that traffics membrane proteins to Cilia. *Cell*, *141*(7), 1208–1219. https://doi.org/10.1016/j.cell.2010.05.015

Jin, S., Guerrero-Juarez, C. F., Zhang, L., Chang, I., Ramos, R., Kuan, C. H., Myung, P., Plikus, M. V., & Nie, Q. (2021). Inference and analysis of cell-cell communication using CellChat. *Nature Communications*, *12*(1). https://doi.org/10.1038/s41467-021-21246-9

Jing, J., Wu, Z., Wang, J., Luo, G., Lin, H., Fan, Y., & Zhou, C. (2023). Hedgehog signaling in tissue homeostasis, cancers, and targeted therapies. In *Signal Transduction and Targeted Therapy* (Vol. 8, Issue 1). Springer Nature. https://doi.org/10.1038/s41392-023-01559-5

Joan Blanchette-Mackie, E., Dwyer, N. K., Therese Barber, L., Coxey, R. A., Takeda, T., Rondinone, C. M., Theodorakis, J. L., Greenberg, A. S., Londost, C., Dwyer, N. K., Barber, T., Coxey, R. A., Takeda, T., Rondinone, C. M., Theodorakis, J. L., Greenberg, A. S., & Londos Perilipin, C. (1995). *Perilipin is located on the surface layer of intracellular lipid droplets in adipocytes*.

Joffin, N., Paschoal, V. A., Gliniak, C. M., Crewe, C., Elnwasany, A., Szweda, L. I., Zhang, Q., Hepler, C., Kusminski, C. M., Gordillo, R., Oh, D. Y., Gupta, R. K., & Scherer, P. E. (2021). Mitochondrial metabolism is a key regulator of the fibro-inflammatory and adipogenic stromal subpopulations in white adipose tissue. *Cell Stem Cell*, *28*(4). https://doi.org/10.1016/j.stem.2021.01.002

Johnson, G. P., Fair, S., & Hoey, D. A. (2021). Primary cilium-mediated MSC mechanotransduction is dependent on Gpr161 regulation of hedgehog signalling. *Bone*, *145*. https://doi.org/10.1016/j.bone.2021.115846

Kim, J. B., Sarraf, P., Wright, M., Yao, K. M., Mueller, E., Solanes, G., Lowell, B. B., & Spiegelman, B. M. (1998). Rapid Publication Nutritional and Insulin Regulation of Fatty Acid Synthetase and Leptin Gene Expression through ADD1/SREBP1 Key words: ADD1/SREBP1 • fatty acid synthetase • leptin • nutritional changes • insulin. In *J. Clin. Invest* (Vol. 101, Issue 1). http://www.jci.org

Kim, S., & Dynlacht, B. D. (2013). Assembling a primary cilium. In *Current Opinion in Cell Biology* (Vol. 25, Issue 4, pp. 506–511). https://doi.org/10.1016/j.ceb.2013.04.011

Klausen, C. (2020). *Analyzing the role of ciliary cAMP signaling in neurons*.

Klein, D., & Ammann, F. (1969). *The Syndrome of Laurence-Moon-Bardet-Biedl and Allied Diseases in Switzerland Clinical, Genetic and Epidemiological Studies*.

Klein, F., Veiga-Villauriz, C., Börsch, A., Maio, S., Palmer, S., Dhalla, F., Handel, A. E., Zuklys, S., Calvo-Asensio, I., Musette, L., Deadman, M. E., White, A. J., Lucas, B., Anderson, G., & Holländer, G. A. (2023). Combined multidimensional single-cell protein and RNA profiling dissects the cellular and functional heterogeneity of thymic epithelial cells. *Nature Communications*, *14*(1). https://doi.org/10.1038/s41467-023-39722-9

Klemm, D. J., Leitner, J. W., Watson, P., Nesterova, A., Reusch, J. E. B., Goalstone, M. L., & Draznin, B. (2001). Insulin-induced adipocyte differentiation: Activation of

CREB rescues adipogenesis from the arrest caused by inhibition of prenylation. *Journal of Biological Chemistry*, *276*(30), 28430–28435. https://doi.org/10.1074/jbc.M103382200

Klink, B. U., Gatsogiannis, C., Hofnagel, O., Wittinghofer, A., & Raunser, S. (2020). Structure of the human BBSome core complex. *ELife*, *9*. https://doi.org/10.7554/eLife.53910

Klink, B. U., Zent, E., Juneja, P., Kuhlee, A., Raunser, S., & Wittinghofer, A. (2017). A recombinant BBSome core complex and how it interacts with ciliary cargo. *ELife*, *6*. https://doi.org/10.7554/eLife.27434

Kopinke, D., Roberson, E. C., & Reiter, J. F. (2017). Ciliary Hedgehog Signaling Restricts Injury-Induced Adipogenesis. *Cell*, *170*(2), 340-351.e12. https://doi.org/10.1016/j.cell.2017.06.035

Kraus, N. A., Ehebauer, F., Zapp, B., Rudolphi, B., Kraus, B. J., & Kraus, D. (2016). Quantitative assessment of adipocyte differentiation in cell culture. *Adipocyte*, *5*(4), 351–358. https://doi.org/10.1080/21623945.2016.1240137

Krueger, K. C., Costa, M. J., Du, H., & Feldman, B. J. (2014). Characterization of cre recombinase activity for in vivo targeting of adipocyte precursor cells. *Stem Cell Reports*, *3*(6), 1147–1158. https://doi.org/10.1016/j.stemcr.2014.10.009

Kuerschner, L., & Thiele, C. (2022). Tracing Lipid Metabolism by Alkyne Lipids and Mass Spectrometry: The State of the Art. In *Frontiers in Molecular Biosciences* (Vol. 9). Frontiers Media S.A. https://doi.org/10.3389/fmolb.2022.880559

Lacey, S. E., & Pigino, G. (2024). The intraflagellar transport cycle. In *Nature Reviews Molecular Cell Biology*. Nature Research. https://doi.org/10.1038/s41580-024-00797-x

Laemmli, U. K. (1970). Cleavage of structural proteins during the assembly of the head of bacteriophage T4. *Nature*, *227*(5259). https://doi.org/10.1038/227680a0

Lamouille, S., Xu, J., & Derynck, R. (2014). Molecular mechanisms of epithelial-mesenchymal transition. In *Nature Reviews Molecular Cell Biology* (Vol. 15, Issue 3, pp. 178–196). https://doi.org/10.1038/nrm3758

Lechtreck, K. F., Johnson, E. C., Sakai, T., Cochran, D., Ballif, B. A., Rush, J., Pazour, G. J., Ikebe, M., & Witman, G. B. (2009). The Chlamydomonas reinhardtii BBSome is

an IFT cargo required for export of specific signaling proteins from flagella. *Journal of Cell Biology*, *187*(7), 1117–1132. https://doi.org/10.1083/jcb.200909183

Lee, J., Ekker, S., von Kessler, D., Porter, J., Sun, B., & Beachy, P. (1994). Autoproteolysis in hedgehog protein biogenesis. *Science*, *266*(5190). https://doi.org/10.1126/science.7985023

Lee, J. H., Ealey, K. N., Patel, Y., Verma, N., Thakkar, N., Park, S. Y., Kim, J. R., & Sung, H. K. (2022). Characterization of adipose depot-specific stromal cell populations by single-cell mass cytometry. *IScience*, *25*(4). https://doi.org/10.1016/j.isci.2022.104166

Lee, K. W., Yeo, S. Y., Gong, J. R., Koo, O. J., Sohn, I., Lee, W. Y., Kim, H. C., Yun, S. H., Cho, Y. B., Choi, M. A., An, S., Kim, J., Sung, C. O., Cho, K. H., & Kim, S. H. (2022). PRRX1 is a master transcription factor of stromal fibroblasts for myofibroblastic lineage progression. *Nature Communications*, *13*(1). https://doi.org/10.1038/s41467-022-30484-4

Lee, Y. H., Kim, S. H., Lee, Y. J., Kang, E. S., Lee, B. W., Cha, B. S., Kim, J. W., Song, D. H., & Lee, H. C. (2013). Transcription factor Snail is a novel regulator of adipocyte differentiation via inhibiting the expression of peroxisome proliferator-activated receptor γ. *Cellular and Molecular Life Sciences*, *70*(20), 3959–3971. https://doi.org/10.1007/s00018-013-1363-8

Lefterova, M. I., Zhang, Y., Steger, D. J., Schupp, M., Schug, J., Cristancho, A., Feng, D., Zhuo, D., Stoeckert, C. J., Liu, X. S., & Lazar, M. A. (2008). PPARγ and C/EBP factors orchestrate adipocyte biology via adjacent binding on a genome-wide scale. *Genes and Development*, *22*(21), 2941–2952. https://doi.org/10.1101/gad.1709008

Lewis, P. M., Dunn, M. P., McMahon, J. A., Logan, M., Martin, J. F., St-Jacques, B., & McMahon, A. P. (2001). Cholesterol modification of sonic hedgehog is required for long-range signaling activity and effective modulation of signaling by Ptc1. *Cell*, *105*(5). https://doi.org/10.1016/S0092-8674(01)00369-5

Li, C., & Wang, B. (2022). Mesenchymal Stem/Stromal Cells in Progressive Fibrogenic Involvement and Anti-Fibrosis Therapeutic Properties. In *Frontiers in Cell and Developmental Biology* (Vol. 10). https://doi.org/10.3389/fcell.2022.902677

Li, J., Wang, C., Wu, C., Cao, T., Xu, G., Meng, Q., & Wang, B. (2017). PKA-mediated Gli2 and Gli3 phosphorylation is inhibited by Hedgehog signaling in cilia and

reduced in Talpid3 mutant. *Developmental Biology*, *429*(1). https://doi.org/10.1016/j.ydbio.2017.06.035

Li, X., Deng, W., Nail, C. D., Bailey, S. K., Kraus, M. H., Ruppert, J. M., & Lobo-Ruppert, S. M. (2006). *Snail induction is an early response to Gli1 that determines the efficiency of epithelial transformation*.

Li, X., Yueshui, Z., Chuan, C., Li, Y., Hyun-ho, L., Zening, W., Ningyan, Z., Mikhail G., K., Zhiqiang, A., Xin, G., Philipp E., S., & and Sun, K. (2020). Critical Role of Matrix Metalloproteinase 14 in Adipose Tissue Remodeling during Obesity. *Molecular and Cellular Biology*, *40*(8), e00564-19. https://doi.org/10.1128/MCB.00564-19

Liao, Y., Smyth, G. K., & Shi, W. (2014). FeatureCounts: An efficient general purpose program for assigning sequence reads to genomic features. *Bioinformatics*, *30*(7). https://doi.org/10.1093/bioinformatics/btt656

Lindhorst, A., Raulien, N., Wieghofer, P., Eilers, J., Rossi, F. M. V., Bechmann, I., & Gericke, M. (2021). Adipocyte death triggers a pro-inflammatory response and induces metabolic activation of resident macrophages. *Cell Death and Disease*, *12*(6). https://doi.org/10.1038/s41419-021-03872-9

Liu, Y., Zou, D., Qi, D., Liu, Z., Du, Y., & Ma, J. (2021). Research Progress of Cell Immortalization Technology. *Chinese Journal of Wildlife*, *42*(2). https://doi.org/10.19711/j.cnki.issn2310-1490.2021.02.039

López-Jiménez, A. J., Basak, T., & Vanacore, R. M. (2017). Proteolytic processing of lysyl oxidase–like-2 in the extracellular matrix is required for crosslinking of basement membrane collagen IV. *Journal of Biological Chemistry*, *292*(41). https://doi.org/10.1074/jbc.M117.798603

Louro, I. R. D., Bailey, E. C., Li, X., South, L. S., Mckie-Bell, P. R., Yoder, B. K., Huang, C. C., Johnson, M. R., Hill, A. E., Johnson, R. L., & Ruppert, J. M. (2002). Comparative Gene Expression Profile Analysis of GLI and c-MYC in an Epithelial Model of Malignant Transformation. In *CANCER RESEARCH* (Vol. 62). http://www.informatics.jax.org.

Love, M., Anders, S., & Huber, W. (2013). Differential analysis of RNA-Seq data at the gene level using the DESeq package. In *European Molecular Biology Laboratory* (Vol. 10).

Lv, B., Stuck, M. W., Desai, P. B., Cabrera, O. A., & Pazour, G. J. (2021). E3 ubiquitin ligase wwp1 regulates ciliary dynamics of the hedgehog receptor smoothened. *Journal of Cell Biology*, *220*(9). https://doi.org/10.1083/jcb.202010177

Marcelin, G., Ferreira, A., Liu, Y., Atlan, M., Aron-Wisnewsky, J., Pelloux, V., Botbol, Y., Ambrosini, M., Fradet, M., Rouault, C., Hénégar, C., Hulot, J. S., Poitou, C., Torcivia, A., Nail-Barthelemy, R., Bichet, J. C., Gautier, E. L., & Clément, K. (2017). A PDGFRα-Mediated Switch toward CD9high Adipocyte Progenitors Controls Obesity-Induced Adipose Tissue Fibrosis. *Cell Metabolism*, *25*(3), 673–685. https://doi.org/10.1016/j.cmet.2017.01.010

Marion, V., Mockel, A., De Melo, C., Obringer, C., Claussmann, A., Simon, A., Messaddeq, N., Durand, M., Dupuis, L., Loeffler, J. P., King, P., Mutter-Schmidt, C., Petrovsky, N., Stoetzel, C., & Dollfus, H. (2012). BBS-induced ciliary defect enhances adipogenesis, causing paradoxical higher-insulin sensitivity, glucose usage, and decreased inflammatory response. *Cell Metabolism*, *16*(3), 363–377. https://doi.org/10.1016/j.cmet.2012.08.005

Marion, V., Stoetzel, C., Schlicht, D., Messaddeq, N., Koch, M., Flori, E., Danse, J. M., Mandel, J.-L., & Lè Ne Dollfus, H. (2008a). *Transient ciliogenesis involving Bardet-Biedl syndrome proteins is a fundamental characteristic of adipogenic differentiation*. http://www.bowserlab.org/primarycilia/cilialist.html

Marion, V., Stoetzel, C., Schlicht, D., Messaddeq, N., Koch, M., Flori, E., Danse, J. M., Mandel, J.-L., & Lè Ne Dollfus, H. (2008b). *Transient ciliogenesis involving Bardet-Biedl syndrome proteins is a fundamental characteristic of adipogenic differentiation*. http://www.bowserlab.org/primarycilia/cilialist.html

McCoy, M. G., Wei, J. M., Choi, S., Goerger, J. P., Zipfel, W., & Fischbach, C. (2018). Collagen Fiber Orientation Regulates 3D Vascular Network Formation and Alignment. *ACS Biomaterials Science & Engineering*, *4*(8), 2967–2976. https://doi.org/10.1021/acsbiomaterials.8b00384

Merrick, D., Sakers, A., Irgebay, Z., Okada, C., Calvert, C., Morley, M. P., Percec, I., & Seale, P. (2019). Identification of a mesenchymal progenitor cell hierarchy in adipose tissue. *Science*, *364*(6438). https://doi.org/10.1126/science.aav2501

Mouraõ, A., Nager, A. R., Nachury, M. V., & Lorentzen, E. (2014). Structural basis for membrane targeting of the BBSome by ARL6. *Nature Structural and Molecular Biology*, *21*(12), 1035–1041. https://doi.org/10.1038/nsmb.2920

Mukhopadhyay, S., Badgandi, H. B., Hwang, S. H., Somatilaka, B., Shimada, I. S., & Pal, K. (2017). Trafficking to the primary cilium membrane. In *Molecular Biology of the Cell* (Vol. 28, Issue 2, pp. 233–239). American Society for Cell Biology. https://doi.org/10.1091/mbc.E16-07-0505

Mukhopadhyay, S., Wen, X., Chih, B., Nelson, C. D., Lane, W. S., Scales, S. J., & Jackson, P. K. (2010). TULP3 bridges the IFT-A complex and membrane phosphoinositides to promote trafficking of G protein-coupled receptors into primary cilia. *Genes and Development*, *24*(19), 2180–2193. https://doi.org/10.1101/gad.1966210

Mukhopadhyay, S., Wen, X., Ratti, N., Loktev, A., Rangell, L., Scales, S. J., & Jackson, P. K. (2013). The ciliary G-protein-coupled receptor Gpr161 negatively regulates the sonic hedgehog pathway via cAMP signaling. *Cell*, *152*(1–2), 210–223. https://doi.org/10.1016/j.cell.2012.12.026

Nachury, M. V. (2018). The molecular machines that traffic signaling receptors into and out of cilia. In *Current Opinion in Cell Biology* (Vol. 51, pp. 124–131). Elsevier Ltd. https://doi.org/10.1016/j.ceb.2018.03.004

Nager, A. R., Goldstein, J. S., Herranz-Pérez, V., Portran, D., Ye, F., Garcia-Verdugo, J. M., & Nachury, M. V. (2017). An Actin Network Dispatches Ciliary GPCRs into Extracellular Vesicles to Modulate Signaling. *Cell*, *168*(1–2), 252-263.e14. https://doi.org/10.1016/j.cell.2016.11.036

Nahmgoong, H., Jeon, Y. G., Park, E. S., Choi, Y. H., Han, S. M., Park, J., Ji, Y., Sohn, J. H., Han, J. S., Kim, Y. Y., Hwang, I., Lee, Y. K., Huh, J. Y., Choe, S. S., Oh, T. J., Choi, S. H., Kim, J. K., & Kim, J. B. (2022). Distinct properties of adipose stem cell subpopulations determine fat depot-specific characteristics. *Cell Metabolism*, *34*(3), 458-472.e6. https://doi.org/10.1016/j.cmet.2021.11.014

Niederlova, V., Modrak, M., Tsyklauri, O., Huranova, M., & Stepanek, O. (2019). Meta-analysis of genotype-phenotype associations in Bardet-Biedl syndrome uncovers differences among causative genes. *Human Mutation*, *40*(11), 2068–2087. https://doi.org/https://doi.org/10.1002/humu.23862

Nielsen, R., Pedersen, T. Å., Hagenbeek, D., Moulos, P., Siersbæk, R., Megens, E., Denissov, S., Børgesen, M., Francoijs, K. J., Mandrup, S., & Stunnenberg, H. G. (2008). Genome-wide profiling of PPARγ:RXR and RNA polymerase II occupancy reveals temporal activation of distinct metabolic pathways and changes in RXR dimer composition during adipogenesis. *Genes and Development*, *22*(21), 2953–2967. https://doi.org/10.1101/gad.501108

Norris, A. M., Appu, A. B., Johnson, C. D., Zhou, L. Y., McKellar, D. W., Renault, M. A., Hammers, D., Cosgrove, B. D., & Kopinke, D. (2023). Hedgehog signaling via its ligand DHH acts as cell fate determinant during skeletal muscle regeneration. *Nature Communications*, *14*(1). https://doi.org/10.1038/s41467-023-39506-1

Novas, R., Cardenas-Rodriguez, M., Irigoín, F., & Badano, J. L. (2015). Bardet-Biedl syndrome: Is it only cilia dysfunction? In *FEBS Letters* (Vol. 589, Issue 22, pp. 3479–3491). Elsevier B.V. https://doi.org/10.1016/j.febslet.2015.07.031

Nozaki, S., Katoh, Y., Kobayashi, T., & Nakayama, K. (2018). BBS1 is involved in retrograde trafficking of ciliary GPCRs in the context of the BBSome complex. *PLoS ONE*, *13*(3). https://doi.org/10.1371/journal.pone.0195005

Okamura, M., Kudo, H., Wakabayashi, K.-I., Tanaka, T., Nonaka, A., Uchida, A., Tsutsumi, S., Sakakibara, I., Naito, M., Osborne, T. F., Hamakubo, T., Ito, S., Aburatani, H., Yanagisawa, M., Kodama, T., & Sakai, J. (2009). *COUP-TFII acts downstream of Wnt/-catenin signal to silence PPAR gene expression and repress adipogenesis*. https://doi.org/https://doi.org/10.1073/pnas.0901676106

Omenetti, A., Porrello, A., Jung, Y., Yang, L., Popov, Y., Choi, S. S., Witek, R. P., Alpini, G., Venter, J., Vandongen, H. M., Syn, W. K., Baroni, G. S., Benedetti, A., Schuppan, D., & Diehl, A. M. (2008). Hedgehog signaling regulates epithelial-mesenchymal transition during biliary fibrosis in rodents and humans. *Journal of Clinical Investigation*, *118*(10), 3331–3342. https://doi.org/10.1172/JCI35875

Owen, D. L., Mahmud, S. A., Sjaastad, L. E., Williams, J. B., Spanier, J. A., Simeonov, D. R., Ruscher, R., Huang, W., Proekt, I., Miller, C. N., Hekim, C., Jeschke, J. C., Aggarwal, P., Broeckel, U., LaRue, R. S., Henzler, C. M., Alegre, M. L., Anderson, M. S., August, A., … Farrar, M. A. (2019). Thymic regulatory T cells arise via two distinct developmental programs. *Nature Immunology*, *20*(2). https://doi.org/10.1038/s41590-018-0289-6

Pal, K., Hwang, S. hee, Somatilaka, B., Badgandi, H., Jackson, P. K., DeFea, K., & Mukhopadhyay, S. (2016). Smoothened determines β-arrestin-mediated removal of the G protein-coupled receptor Gpr161 from the primary cilium. *Journal of Cell Biology*, *212*(7), 861–875. https://doi.org/10.1083/jcb.201506132

Palla, A. R., Hilgendorf, K. I., Yang, A. V., Kerr, J. P., Hinken, A. C., Demeter, J., Kraft, P., Mooney, N. A., Yucel, N., Burns, D. M., Wang, Y. X., Jackson, P. K., & Blau, H. M. (2022). Primary cilia on muscle stem cells are critical to maintain regenerative capacity and are lost during aging. *Nature Communications*, *13*(1). https://doi.org/10.1038/s41467-022-29150-6

Palmer, B. F., & Clegg, D. J. (2015). The sexual dimorphism of obesity. In *Molecular and Cellular Endocrinology* (Vol. 402, pp. 113–119). Elsevier Ireland Ltd. https://doi.org/10.1016/j.mce.2014.11.029

Pan, C., Kumar, C., Bohl, S., Klingmueller, U., & Mann, M. (2009). Comparative proteomic phenotyping of cell lines and primary cells to assess preservation of cell type-specific functions. *Molecular and Cellular Proteomics*, *8*(3), 443–450. https://doi.org/10.1074/mcp.M800258-MCP200

Paten, J. A., Martin, C. L., Wanis, J. T., Siadat, S. M., Figueroa-Navedo, A. M., Ruberti, J. W., & Deravi, L. F. (2019). Molecular Interactions between Collagen and Fibronectin: A Reciprocal Relationship that Regulates De Novo Fibrillogenesis. *Chem*, *5*(8). https://doi.org/10.1016/j.chempr.2019.05.011

Peláez-García, A., Barderas, R., Batlle, R., Viñas-Castells, R., Bartolomé, R. A., Torres, S., Mendes, M., Lopez-Lucendo, M., Mazzolini, R., Bonilla, F., De Herreros, A. G., & Casal, J. I. (2015). A proteomic analysis reveals that snail regulates the expression of the nuclear orphan receptor nuclear receptor subfamily 2 group F member 6 (Nr2f6) and interleukin 17 (IL-17) to inhibit adipocyte differentiation. *Molecular and Cellular Proteomics*, *14*(2), 303–315. https://doi.org/10.1074/mcp.M114.045328

Peters, C., Wolf, A., Wagner, M., Rgen Kuhlmann, J., Waldmann, H., & Simons, K. (2004). *The cholesterol membrane anchor of the Hedgehog protein confers stable membrane association to lipid-modified proteins*. www.pnas.orgcgidoi10.1073pnas.0308449101

Petersen, R. K., Madsen, L., Pedersen, L. M., Hallenborg, P., Hagland, H., Viste, K., Døskeland, S. O., & Kristiansen, K. (2008). Cyclic AMP (cAMP)-Mediated

Stimulation of Adipocyte Differentiation Requires the Synergistic Action of Epac- and cAMP-Dependent Protein Kinase-Dependent Processes. *Molecular and Cellular Biology*, *28*(11), 3804–3816. https://doi.org/10.1128/mcb.00709-07

Pfaffl, M. (2004). Quantification strategies in real-time PCR Michael W . Pfaffl. *A-Z of Quantitative PCR*. https://doi.org/http://dx.doi.org/10.1007/s10551-011-0963-1

Philips, G. M., Chan, I. S., Swiderska, M., Schroder, V. T., Guy, C., Karaca, G. F., Moylan, C., Venkatraman, T., Feuerlein, S., Syn, W. K., Jung, Y., Witek, R. P., Choi, S., Michelotti, G. A., Rangwala, F., Merkle, E., Lascola, C., & Diehl, A. M. (2011). Hedgehog signaling antagonist promotes regression of both liver fibrosis and hepatocellular carcinoma in a murine model of primary liver cancer. *PLoS ONE*, *6*(9). https://doi.org/10.1371/journal.pone.0023943

Picelli, S., Faridani, O. R., Björklund, Å. K., Winberg, G., Sagasser, S., & Sandberg, R. (2014). Full-length RNA-seq from single cells using Smart-seq2. *Nature Protocols*, *9*(1). https://doi.org/10.1038/nprot.2014.006

Piirsalu, M., Chithanathan, K., Jayaram, M., Visnapuu, T., Lilleväli, K., Zilmer, M., & Vasar, E. (2022). Lipopolysaccharide-Induced Strain-Specific Differences in Neuroinflammation and MHC-I Pathway Regulation in the Brains of Bl6 and 129Sv Mice. *Cells*, *11*(6). https://doi.org/10.3390/cells11061032

Pinette, J. A., Myers, J. W., Park, W. Y., Bryant, H. G., Eddie, A. M., Wilson, G. A., Montufar, C., Shaikh, Z., Vue, Z., Nunn, E. R., Bessho, R., Cottam, M. A., Haase, V. H., Hinton, A. O., Spinelli, J. B., Cartailler, J.-P., & Zaganjor, E. (2024). Disruption of nucleotide biosynthesis reprograms mitochondrial metabolism to inhibit adipogenesis. *Journal of Lipid Research*, 100641. https://doi.org/10.1016/j.jlr.2024.100641

Poole, C. A., Flint, M. H., & Beaumont, B. W. (1985). Analysis of the morphology and function of primary cilia in connective tissues:A cellular cybernetic probe? *Cell Motility*, *5*(3), 175–193. https://doi.org/10.1002/cm.970050302

Porter, J. A., Ekker, S. C., Park, W. J., Von Kessler, D. P., Young, K. E., Chen, C. H., Ma, Y., Woods, A. S., Cotter, R. J., Koonin, E. V., & Beachy, P. A. (1996). Hedgehog patterning activity: Role of a lipophilic modification mediated by the carboxy-terminal autoprocessing domain. *Cell*, *86*(1). https://doi.org/10.1016/S0092-8674(00)80074-4

Prasai, A., Cernohorska, M. S., Ruppova, K., Niederlova, V., Andelova, M., Draber, P., Stepanek, O., & Huranova, M. (2020). The BBSome assembly is spatially controlled by BBS1 and BBS4 in human cells. *Journal of Biological Chemistry*, *295*(42), 14279–14290. https://doi.org/10.1074/jbc.RA120.013905

Pratap, A., Singh, S., Mundra, V., Yang, N., Panakanti, R., Eason, J. D., & Mahato, R. I. (2012). Attenuation of early liver fibrosis by pharmacological inhibition of smoothened receptor signaling. *Journal of Drug Targeting*, *20*(9), 770–782. https://doi.org/10.3109/1061186X.2012.719900

Proctor, A. E., Thompson, L. A., & O'Bryant, C. L. (2014). Vismodegib: An Inhibitor of the Hedgehog Signaling Pathway in the Treatment of Basal Cell Carcinoma. In *Annals of Pharmacotherapy* (Vol. 48, Issue 1). https://doi.org/10.1177/1060028013506696

Pyczek, J., Buslei, R., Schult, D., Hölsken, A., Buchfelder, M., Heß, I., Hahn, H., & Uhmann, A. (2016). Hedgehog signaling activation induces stem cell proliferation and hormone release in the adult pituitary gland. *Scientific Reports*, *6*. https://doi.org/10.1038/srep24928

Rahmouni, K., Fath, M. A., Seo, S., Thedens, D. R., Berry, C. J., Weiss, R., Nishimura, D. Y., & Sheffield, V. C. (2008). Leptin resistance contributes to obesity and hypertension in mouse models of Bardet-Biedl syndrome. *Journal of Clinical Investigation*, *118*(4), 1458–1467. https://doi.org/10.1172/JCI32357

Reggio, S., Rouault, C., Poitou, C., Bichet, J. C., Prifti, E., Bouillot, J. L., Rizkalla, S., Lacasa, D., Tordjman, J., & Clément, K. (2016). Increased basement membrane components in adipose tissue during obesity: Links with TGF- And metabolic phenotypes. *Journal of Clinical Endocrinology and Metabolism*, *101*(6), 2578–2587. https://doi.org/10.1210/jc.2015-4304

Reiter, J. F., & Leroux, M. R. (2017). Genes and molecular pathways underpinning ciliopathies. In *Nature Reviews Molecular Cell Biology* (Vol. 18, Issue 9, pp. 533–547). Nature Publishing Group. https://doi.org/10.1038/nrm.2017.60

Robarge, K. D., Brunton, S. A., Castanedo, G. M., Cui, Y., Dina, M. S., Goldsmith, R., Gould, S. E., Guichert, O., Gunzner, J. L., Halladay, J., Jia, W., Khojasteh, C., Koehler, M. F. T., Kotkow, K., La, H., LaLonde, R. L., Lau, K., Lee, L., Marshall, D., … Xie, M. (2009). GDC-0449-A potent inhibitor of the hedgehog pathway.

Bioorganic and Medicinal Chemistry Letters, *19*(19). https://doi.org/10.1016/j.bmcl.2009.08.049

Rodeheffer, M. S., Birsoy, K., & Friedman, J. M. (2008). Identification of White Adipocyte Progenitor Cells In Vivo. *Cell*, *135*(2), 240–249. https://doi.org/10.1016/j.cell.2008.09.036

Rodríguez, C. I., Buchholz, F., Galloway, J., Sequerra, R., Kasper, J., Ayala, R., Stewart, A. F., & Dymecki, S. M. (2000). High-efficiency deleter mice show that FLPe is an alternative to Cre- loxP. In *Nature Genetics* (Vol. 25, Issue 2). https://doi.org/10.1038/75973

Rohatgi, R., Milenkovic, L., & Scott, M. P. (2007). Patched1 regulates hedgehog signaling at the primary cilium. *Science*, *317*(5836). https://doi.org/10.1126/science.1139740

Rohatgi, R., & Snell, W. J. (2010). The ciliary membrane. In *Current Opinion in Cell Biology* (Vol. 22, Issue 4, pp. 541–546). https://doi.org/10.1016/j.ceb.2010.03.010

Rosen, E. D., Hsu, C. H., Wang, X., Sakai, S., Freeman, M. W., Gonzalez, F. J., & Spiegelman, B. M. (2002). C/EBPα induces adipogenesis through PPARγ: A unified pathway. *Genes and Development*, *16*(1). https://doi.org/10.1101/gad.948702

Rosen, E. D., & MacDougald, O. A. (2006). Adipocyte differentiation from the inside out. In *Nature Reviews Molecular Cell Biology* (Vol. 7, Issue 12, pp. 885–896). https://doi.org/10.1038/nrm2066

Rosenbaum, J. L., & Witman, G. B. (2002). Intraflagellar transport. In *Nature Reviews Molecular Cell Biology* (Vol. 3, Issue 11, pp. 813–825). https://doi.org/10.1038/nrm952

Rupnick, M. A., Panigrahy, D., Zhang, C.-Y., Dallabrida, S. M., Lowell, B. B., Langer, R., & Folkman, M. J. (2002). *Adipose tissue mass can be regulated through the vasculature*. www.pnas.orgcgidoi10.1073pnas.162349799

Sakers, A., De Siqueira, M. K., Seale, P., & Villanueva, C. J. (2022). Adipose-tissue plasticity in health and disease. In *Cell* (Vol. 185, Issue 3, pp. 419–446). Elsevier B.V. https://doi.org/10.1016/j.cell.2021.12.016

Saldaña, J. I., Solanki, A., Lau, C. I., Sahni, H., Ross, S., Furmanski, A. L., Ono, M., Holländer, G., & Crompton, T. (2016). Sonic Hedgehog regulates thymic epithelial

cell differentiation. *Journal of Autoimmunity*, *68*, 86–97. https://doi.org/10.1016/j.jaut.2015.12.004

Samulin, J., Berget, I., Lien, S., & Sundvold, H. (2008). Differential gene expression of fatty acid binding proteins during porcine adipogenesis. *Comparative Biochemistry and Physiology - B Biochemistry and Molecular Biology*, *151*(2), 147–152. https://doi.org/10.1016/j.cbpb.2008.06.010

Sari, I. N., Phi, L. T. H., Jun, N., Wijaya, Y. T., Lee, S., & Kwon, H. Y. (2018). Hedgehog signaling in cancer: A prospective therapeutic target for eradicating cancer stem cells. In *Cells* (Vol. 7, Issue 11). MDPI. https://doi.org/10.3390/cells7110208

Saygin, C., Wiechert, A., Rao, V. S., Alluri, R., Connor, E., Thiagarajan, P. S., Hale, J. S., Li, Y., Chumakova, A., Jarrar, A., Parker, Y., Lindner, D. J., Nagaraj, A. B., Kim, J. J., DiFeo, A., Abdul-Karim, F. W., Michener, C., Rose, P. G., DeBernardo, R., … Reizes, O. (2017). CD55 regulates self-renewal and cisplatin resistance in endometrioid tumors. *Journal of Experimental Medicine*, *214*(9), 2715–2732. https://doi.org/10.1084/jem.20170438

Scheidecker, S., Etard, C., Pierce, N. W., Geoffroy, V., Schaefer, E., Muller, J., Chennen, K., Flori, E., Pelletier, V., Poch, O., Marion, V., Stoetzel, C., Strähle, U., Nachury, M. V., & Dollfus, H. (2014). Exome sequencing of Bardet-Biedl syndrome patient identifies a null mutation in the bbsome subunit BBIP1 (BBS18). *Journal of Medical Genetics*, *51*(2), 132–136. https://doi.org/10.1136/jmedgenet-2013-101785

Schmidt, U., Weigert, M., Broaddus, C., & Myers, G. (2018). Cell detection with star-convex polygons. *Lecture Notes in Computer Science (Including Subseries Lecture Notes in Artificial Intelligence and Lecture Notes in Bioinformatics)*, *11071 LNCS*, 265–273. https://doi.org/10.1007/978-3-030-00934-2_30

Schneider, S., De Cegli, R., Nagarajan, J., Kretschmer, V., Matthiessen, P. A., Intartaglia, D., Hotaling, N., Ueffing, M., Boldt, K., Conte, I., & May-Simera, H. L. (2021). Loss of Ciliary Gene Bbs8 Results in Physiological Defects in the Retinal Pigment Epithelium. *Frontiers in Cell and Developmental Biology*, *9*. https://doi.org/10.3389/fcell.2021.607121

Schwalie, P. C., Dong, H., Zachara, M., Russeil, J., Alpern, D., Akchiche, N., Caprara, C., Sun, W., Schlaudraff, K. U., Soldati, G., Wolfrum, C., & Deplancke, B. (2018). A

stromal cell population that inhibits adipogenesis in mammalian fat depots. *Nature*, *559*(7712), 103–108. https://doi.org/10.1038/s41586-018-0226-8

Sekulic, A., Migden, M. R., Oro, A. E., Dirix, L., Lewis, K. D., Hainsworth, J. D., Solomon, J. A., Yoo, S., Arron, S. T., Friedlander, P. A., Marmur, E., Rudin, C. M., Chang, A. L. S., Low, J. A., Mackey, H. M., Yauch, R. L., Graham, R. A., Reddy, J. C., & Hauschild, A. (2012). Efficacy and Safety of Vismodegib in Advanced Basal-Cell Carcinoma. *New England Journal of Medicine*, *366*(23). https://doi.org/10.1056/nejmoa1113713

Senk, A., & Djonov, V. (2021). Collagen fibers provide guidance cues for capillary regrowth during regenerative angiogenesis in zebrafish. *Scientific Reports*, *11*(1). https://doi.org/10.1038/s41598-021-98852-6

Seo, S., Guo, D. F., Bugge, K., Morgan, D. A., Rahmouni, K., & Sheffield, V. C. (2009). Requirement of Bardet-Biedl syndrome proteins for leptin receptor signaling. *Human Molecular Genetics*, *18*(7), 1323–1331. https://doi.org/10.1093/hmg/ddp031

Seo, S., Zhang, Q., Bugge, K., Breslow, D. K., Searby, C. C., Nachury, M. V., & Sheffield, V. C. (2011). A novel protein LZTFL1 regulates ciliary trafficking of the BBSome and smoothened. *PLoS Genetics*, *7*(11). https://doi.org/10.1371/journal.pgen.1002358

Seong, J., Tajik, A., Sun, J., Guan, J. L., Humphries, M. J., Craig, S. E., Shekaran, A., García, A. J., Lu, S., Lin, M. Z., Wang, N., & Wang, Y. (2013). Distinct biophysical mechanisms of focal adhesion kinase mechanoactivation by different extracellular matrix proteins. *Proceedings of the National Academy of Sciences of the United States of America*, *110*(48), 19372–19377. https://doi.org/10.1073/pnas.1307405110

Shan, T., Liu, W., & Kuang, S. (2013). Fatty acid binding protein 4 expression marks a population of adipocyte progenitors in white and brown adipose tissues. *FASEB Journal*, *27*(1). https://doi.org/10.1096/fj.12-211516

Shao, M., Hepler, C., Zhang, Q., Shan, B., Vishvanath, L., Henry, G. H., Zhao, S., An, Y. A., Wu, Y., Strand, D. W., & Gupta, R. K. (2021). Pathologic HIF1α signaling drives adipose progenitor dysfunction in obesity. *Cell Stem Cell*, *28*(4), 685-701.e7. https://doi.org/10.1016/j.stem.2020.12.008

Shen, X., Peng, Y., & Li, H. (2017). The injury-related activation of hedgehog signaling pathway modulates the repair-associated inflammation in liver fibrosis. In *Frontiers*

in Immunology (Vol. 8, Issue NOV). Frontiers Media S.A. https://doi.org/10.3389/fimmu.2017.01450

Shimada, I. S., & Kato, Y. (2022). Ciliary signaling in stem cells in health and disease: Hedgehog pathway and beyond. In *Seminars in Cell and Developmental Biology* (Vol. 129, pp. 115–125). Elsevier Ltd. https://doi.org/10.1016/j.semcdb.2022.04.011

Shin, K., Lim, A., Zhao, C., Sahoo, D., Pan, Y., Spiekerkoetter, E., Liao, J. C., & Beachy, P. A. (2014). Hedgehog signaling restrains bladder cancer progression by eliciting stromal production of urothelial differentiation factors. *Cancer Cell*, *26*(4), 521–533. https://doi.org/10.1016/j.ccell.2014.09.001

Shinde, S. R., Mick, D. U., Aoki, E., Rodrigues, R. B., Gygi, S. P., & Nachury, M. V. (2023). The ancestral ESCRT protein TOM1L2 selects ubiquitinated cargoes for retrieval from cilia. *Developmental Cell*, *58*(8), 677-693.e9. https://doi.org/10.1016/j.devcel.2023.03.003

Shinde, S. R., Nager, A. R., & Nachury, M. V. (2020). Ubiquitin chains earmark GPCRs for BBSome-mediated removal from cilia. *Journal of Cell Biology*, *219*(12). https://doi.org/10.1083/JCB.202003020

Sieckmann, K., Winnerling, N., Huebecker, M., Leyendecker, P., Silva Ribeiro, D. J., Gnad, T., Pfeifer, A., Wachten, D., & Hansen, J. N. (2022). AdipoQ—a simple, open-source software to quantify adipocyte morphology and function in tissues and in vitro. *Molecular Biology of the Cell*, *33*(12). https://doi.org/10.1091/mbc.E21-11-0592

Sieckmann, K., Winnerling, N., Juliana, D., Ribeiro, S., Kardinal, R., Steinheuer, L. M., Schermann, G., Klausen, C., Blank-Stein, N., Schulte-Schrepping, J., Osei-Sarpong, C., Becker, M., Bonaguro, L., Beyer, M., Thurley, K., May-Simera, H. L., Zurkovic, J., Thiele, C., Ruiz De Almodovar, C., … Wachten, D. (2024). BBSome-dependent ciliary Hedgehog signaling governs cell fate in the white adipose tissue. *BioRxiv*.

Sigafoos, A. N., Paradise, B. D., & Fernandez-Zapico, M. E. (2021). Hedgehog/gli signaling pathway: Transduction, regulation, and implications for disease. *Cancers*, *13*(14). https://doi.org/10.3390/cancers13143410

Singh, S., Gui, M., Koh, F., Yip, M. C. J., & Brown, A. (2020). Structure and activation mechanism of the BBsome membrane protein trafficking complex. *ELife*, *9*. https://doi.org/10.7554/eLife.53322

Skarnes, W. C., Rosen, B., West, A. P., Koutsourakis, M., Bushell, W., Iyer, V., Mujica, A. O., Thomas, M., Harrow, J., Cox, T., Jackson, D., Severin, J., Biggs, P., Fu, J., Nefedov, M., De Jong, P. J., Stewart, A. F., & Bradley, A. (2011). A conditional knockout resource for the genome-wide study of mouse gene function. *Nature*, *474*(7351), 337–344. https://doi.org/10.1038/nature10163

Solanki, A., Yanez, D. C., Ross, S., Lau, C. I., Papaioannou, E., Li, J., Saldaña, J. I., & Crompton, T. (2018). Gli3 in fetal thymic epithelial cells promotes thymocyte positive selection and differentiation by repression of Shh. *Development (Cambridge)*, *145*(3). https://doi.org/10.1242/dev.146910

Spallanzani, R. G., Zemmour, D., Xiao, T., Jayewickreme, T., Li, C., Bryce, P. J., Benoist, C., & Mathis, D. (2019). Distinct immunocyte-promoting and adipocyte-generating stromal components coordinate adipose tissue immune and metabolic tenors. In *Sci. Immunol* (Vol. 4). http://immunology.sciencemag.org/

Spandl, J., White, D. J., Peychl, J., & Thiele, C. (2009). Live cell multicolor imaging of lipid droplets with a new dye, LD540. *Traffic*, *10*(11), 1579–1584. https://doi.org/10.1111/j.1600-0854.2009.00980.x

Spencer, V. A., Xu, R., & Bissell, M. J. (2007). Extracellular Matrix, Nuclear and Chromatin Structure, and Gene Expression in Normal Tissues and Malignant Tumors: A Work in Progress. In *Advances in Cancer Research* (Vol. 97). https://doi.org/10.1016/S0065-230X(06)97012-2

Spinella-Jaegle, S., Rawadi, G., Kawai, S., Gallea, S., Faucheu, C., Mollat, P., Courtois, B., Bergaud, B., Ramez, V., Blanchet, A. M., Adelmant, G., Baron, R., & Roman-Roman, S. (2001). Sonic hedgehog increases the commitment of pluripotent mesenchymal cells into the osteoblastic lineage and abolishes adipocytic differentiation. *Journal of Cell Science*, *114*(11), 2085–2094. https://doi.org/10.1242/jcs.114.11.2085

Stamati, K., Priestley, J. V., Mudera, V., & Cheema, U. (2014). Laminin promotes vascular network formation in 3D in vitro collagen scaffolds by regulating VEGF

uptake. *Experimental Cell Research*, *327*(1), 68–77. https://doi.org/10.1016/j.yexcr.2014.05.012

Stubbs, T., Bingman, J. I., Besse, J., & Mykytyn, K. (2023). Ciliary signaling proteins are mislocalized in the brains of Bardet-Biedl syndrome 1-null mice. *Frontiers in Cell and Developmental Biology*, *10*. https://doi.org/10.3389/fcell.2022.1092161

Suh, J. M., Gao, X., McKay, J., McKay, R., Salo, Z., & Graff, J. M. (2006). Hedgehog signaling plays a conserved role in inhibiting fat formation. *Cell Metabolism*, *3*(1), 25–34. https://doi.org/10.1016/j.cmet.2005.11.012

Sun, K., Li, X., & Scherer, P. E. (2023). Extracellular Matrix (ECM) and Fibrosis in Adipose Tissue: Overview and Perspectives. *Comprehensive Physiology*, *13*(1), 4387–4407. https://doi.org/10.1002/cphy.c220020

Sun, X., Are, A., Annusver, K., Sivan, U., Jacob, T., Dalessandri, T., Joost, S., Füllgrabe, A., Gerling, M., & Kasper, M. (2020). Coordinated hedgehog signaling induces new hair follicles in adult skin. *ELife*, *9*. https://doi.org/10.7554/eLife.46756

Tadenev, A. L. D., Kulaga, H. M., May-Simera, H. L., Kelley, M. W., Katsanis, N., & Reed, R. R. (2011). Loss of Bardet - Biedl syndrome protein-8 (BBS8) perturbs olfactory function, protein localization, and axon targeting. *Proceedings of the National Academy of Sciences of the United States of America*, *108*(25), 10320–10325. https://doi.org/10.1073/pnas.1016531108

Takebe, N., Miele, L., Harris, P. J., Jeong, W., Bando, H., Kahn, M., Yang, S. X., & Ivy, S. P. (2015). Targeting Notch, Hedgehog, and Wnt pathways in cancer stem cells: Clinical update. In *Nature Reviews Clinical Oncology* (Vol. 12, Issue 8). https://doi.org/10.1038/nrclinonc.2015.61

Tang, Q.-Q., Otto, T. C., & Daniel Lane, M. (2002). *Mitotic clonal expansion: A synchronous process required for adipogenesis*. https://www.pnas.org

Tang, W., Zeve, D., Suh, J. M., Bosnakovski, D., Kyba, M., Hammer, R. E., Tallquist, M. D., & Graff, J. M. (2008). White fat progenitor cells reside in the adipose vasculature. *Science*, *322*(5901), 583–586. https://doi.org/10.1126/science.1156232

Tanos, B. E., Yang, H. J., Soni, R., Wang, W. J., Macaluso, F. P., Asara, J. M., & Tsou, M. F. B. (2013). Centriole distal appendages promote membrane docking, leading to cilia initiation. *Genes and Development*, *27*(2), 163–168. https://doi.org/10.1101/gad.207043.112

Targett-Adams, P., Chambers, D., Gledhill, S., Hope, R. G., Coy, J. F., Girod, A., & McLauchlan, J. (2003). Live cell analysis and targeting of the lipid droplet-binding adipocyte differentiation-related protein. *Journal of Biological Chemistry*, *278*(18), 15998–16007. https://doi.org/10.1074/jbc.M211289200

Teves, M. E., Strauss, J. F., Sapao, P., Shi, B., & Varga, J. (2019). The Primary Cilium: Emerging Role as a Key Player in Fibrosis. In *Current Rheumatology Reports* (Vol. 21, Issue 6). Current Medicine Group LLC 1. https://doi.org/10.1007/s11926-019-0822-0

Tian, X., Zhao, H., & Zhou, J. (2023). Organization, functions, and mechanisms of the BBSome in development, ciliopathies, and beyond. *ELife*, *12*. https://doi.org/10.7554/eLife.87623

To, W. S., & Midwood, K. S. (2011). Plasma and cellular fibronectin: Distinct and independent functions during tissue repair. In *Fibrogenesis and Tissue Repair* (Vol. 4, Issue 1). https://doi.org/10.1186/1755-1536-4-21

Tran, K. Van, Gealekman, O., Frontini, A., Zingaretti, M. C., Morroni, M., Giordano, A., Smorlesi, A., Perugini, J., De Matteis, R., Sbarbati, A., Corvera, S., & Cinti, S. (2012). The vascular endothelium of the adipose tissue gives rise to both white and brown fat cells. *Cell Metabolism*, *15*(2), 222–229. https://doi.org/10.1016/j.cmet.2012.01.008

Tschaikner, P. M., Regele, D., Röck, R., Salvenmoser, W., Meyer, D., Bouvier, M., Geley, S., Stefan, E., & Aanstad, P. (2021). Feedback control of the Gpr161-Gαs-PKA axis contributes to basal Hedgehog repression in zebrafish. *Development (Cambridge)*, *148*(4). https://doi.org/10.1242/dev.192443

Ucar, A., Ucar, O., Klug, P., Matt, S., Brunk, F., Hofmann, T. G., & Kyewski, B. (2014). Adult thymus contains foxN1- epithelial stem cells that are bipotent for medullary and cortical thymic epithelial lineages. *Immunity*, *41*(2). https://doi.org/10.1016/j.immuni.2014.07.005

Ullah, A., Umair, M., Yousaf, M., Khan, S. A., Nazim-Ud-Din, M., Shah, K., Ahmad, F., Azeem, Z., Ali, G., Alhaddad, B., Rafique, A., Jan, A., Haack, T. B., Strom, T. M., Meitinger, T., Ghous, T., Ahmad, W., Jammu, A., & Kashmir, P. ; (2017). *Sequence variants in four genes underlying Bardet-Biedl syndrome in consanguineous families*. http://www.molvis.org/molvis/v23/482

Umberger, N. L., & Caspary, T. (2015). Ciliary transport regulates PDGF-AA/αα signaling via elevated mammalian target of rapamycin signaling and diminished PP2A activity. *Molecular Biology of the Cell*, *26*(2), 350–358. https://doi.org/10.1091/mbc.E14-05-0952

Varghese, M., Griffin, C., McKernan, K., Eter, L., Lanzetta, N., Agarwal, D., Abrishami, S., & Singer, K. (2019). Sex differences in inflammatory responses to adipose tissue lipolysis in diet-induced obesity. *Endocrinology*, *160*(2), 293–312. https://doi.org/10.1210/en.2018-00797

Vegiopoulos, A., Rohm, M., & Herzig, S. (2017). Adipose tissue: between the extremes. *The EMBO Journal*, *36*(14), 1999–2017. https://doi.org/10.15252/embj.201696206

Venugopal, N., Ghosh, A., Gala, H., Aloysius, A., Vyas, N., & Dhawan, J. (2020). The primary cilium dampens proliferative signaling and represses a G2/M transcriptional network in quiescent myoblasts. *BMC Molecular and Cell Biology*, *21*(1). https://doi.org/10.1186/s12860-020-00266-1

Wachten, D., & Mick, D. U. (2021). Signal transduction in primary cilia – analyzing and manipulating GPCR and second messenger signaling. In *Pharmacology and Therapeutics* (Vol. 224). Elsevier Inc. https://doi.org/10.1016/j.pharmthera.2021.107836

Wang, B., Fallon, J. F., & Beachy, P. A. (2000). Hedgehog-Regulated Processing of Gli3 Produces an Anterior / Posterior Repressor Gradient in the Developing Vertebrate Limb University of Wisconsin at Madison. *Cell*, *100*.

Wang, F., Ma, L., Zhang, Z., Liu, X., Gao, H., Zhuang, Y., Yang, P., Kornmann, M., Tian, X., & Yang, Y. (2016). Hedgehog signaling regulates epithelial-mesenchymal transition in pancreatic cancer stem-like cells. *Journal of Cancer*, *7*(4), 408–417. https://doi.org/10.7150/jca.13305

Wang, H., Du, Y., Huang, S., Sun, X., Ye, Y., Sun, H., Chu, X., Shan, X., Yuan, Y., Shen, L., & Bi, Y. (2024). Single-cell analysis reveals a subpopulation of adipose progenitor cells that impairs glucose homeostasis. *Nature Communications*, *15*(1). https://doi.org/10.1038/s41467-024-48914-w

Wiegering, A., Petzsch, P., Köhrer, K., Rüther, U., & Gerhardt, C. (2019). GLI3 repressor but not GLI3 activator is essential for mouse eye patterning and morphogenesis. *Developmental Biology*, *450*(2). https://doi.org/10.1016/j.ydbio.2019.02.018

Wilson, S. L., Wilson, J. P., Wang, C., Wang, B., & Mcconnell, S. K. (2012). Primary cilia and Gli3 activity regulate cerebral cortical size. *Developmental Neurobiology*, *72*(9), 1196–1212. https://doi.org/10.1002/dneu.20985

Winnerling, N. L. (2022). *Cilia-dependent signaling pathways controlling adipose tissue plasticity*.

Wloga, D., & Gaertig, J. (2010). Post-translational modifications of microtubules. *Journal of Cell Science*, *123*(20), 3447–3455. https://doi.org/10.1242/jcs.063727

Wloga, D., Joachimiak, E., Louka, P., & Gaertig, J. (2017). Posttranslational modifications of Tubulin and cilia. *Cold Spring Harbor Perspectives in Biology*, *9*(6). https://doi.org/10.1101/cshperspect.a028159

Wu/'^, Z., Xie/'^, Y., Bucher, N. L. R., & Farmer^, S. R. (1995). *Conditional ectopic expression of C/EBPP in NIH-3T3 cells induces PPAR7 and stimulates adipogenesis*.

Wu, M., Mi, J., Qu, G. X., Zhang, S., Jian, Y., Gao, C., Cai, Q., Liu, J., Jiang, J., & Huang, H. (2024). Role of Hedgehog Signaling Pathways in Multipotent Mesenchymal Stem Cells Differentiation. In *Cell Transplantation* (Vol. 33). SAGE Publications Ltd. https://doi.org/10.1177/09636897241244943

Wunderling, K., Zurkovic, J., Zink, F., Kuerschner, L., & Thiele, C. (2023). Triglyceride cycling enables modification of stored fatty acids. *Nature Metabolism*, *5*(4). https://doi.org/10.1038/s42255-023-00769-z

Xing, Y., & Hogquist, K. A. (2014). Isolation, identification, and purification of murine thymic epithelial cells. *Journal of Visualized Experiments*, *90*. https://doi.org/10.3791/51780

Yamada, T., Pfaff, S. L., Edlund, T., & Jessell, T. M. (1993). Control of Cell Pattern in the Neural Tube: Motor Neuron Induction by Diffusible Factors from Notochord and Floor Plate. In *Cell* (Vol. 73).

Yan, J., Hu, B., Shi, W., Wang, X., Shen, J., Chen, Y., Huang, H., & Jin, L. (2021). Gli2-regulated activation of hepatic stellate cells and liver fibrosis by TGF-β signaling. *American Journal of Physiology - Gastrointestinal and Liver Physiology*, *320*(5), G720–G728. https://doi.org/10.1152/AJPGI.00310.2020

Yan, L., & Zheng, Y. F. (2022). Cilia and their role in neural tube development and defects. In *Reproductive and Developmental Medicine* (Vol. 6, Issue 2, pp. 67–78). Lippincott Williams and Wilkins. https://doi.org/10.1097/RD9.0000000000000014

Yang, J., Antin, P., Berx, G., Blanpain, C., Brabletz, T., Bronner, M., Campbell, K., Cano, A., Casanova, J., Christofori, G., Dedhar, S., Derynck, R., Ford, H. L., Fuxe, J., García de Herreros, A., Goodall, G. J., Hadjantonakis, A. K., Huang, R. J. Y., Kalcheim, C., … Sheng, G. (2020). Guidelines and definitions for research on epithelial–mesenchymal transition. In *Nature Reviews Molecular Cell Biology* (Vol. 21, Issue 6, pp. 341–352). Nature Research. https://doi.org/10.1038/s41580-020-0237-9

Yang Loureiro, Z., Joyce, S., DeSouza, T., Solivan-Rivera, J., Desai, A., Skritakis, P., Yang, Q., Ziegler, R., Zhong, D., Nguyen, T. T., MacDougald, O. A., & Corvera, S. (2023). Wnt signaling preserves progenitor cell multipotency during adipose tissue development. *Nature Metabolism*, *5*(6), 1014–1028. https://doi.org/10.1038/s42255-023-00813-y

Yang, S., Bahl, K., Chou, H. T., Woodsmith, J., Stelzl, U., Walz, T., & Nachury, M. V. (2020). Near-atomic structures of the BBSome reveal the basis for BBSome activation and binding to GPCR cargoes. *ELife*, *9*, 1–21. https://doi.org/10.7554/eLife.55954

Yayon, N., Kedlian, V. R., Boehme, L., Suo, C., Wachter, B. T., Beuschel, R. T., Amsalem, O., Polanski, K., Koplev, S., Tuck, E., Dann, E., Van Hulle, J., Perera, S., Putteman, T., Predeus, A. V., Dabrowska, M., Richardson, L., Tudor, C., Kreins, A. Y., … Teichmann, S. A. (2024). A spatial human thymus cell atlas mapped to a continuous tissue axis. *Nature*, *635*(8039), 708–718. https://doi.org/10.1038/s41586-024-07944-6

Ye, F., Nager, A. R., & Nachury, M. V. (2018). BBSome trains remove activated GPCRs from cilia by enabling passage through the transition zone. *Journal of Cell Biology*, *217*(5), 1847–1868. https://doi.org/10.1083/jcb.201709041

Yeh, W.-C., Cao, Z., Classon, M., & Mcknight, S. L. (1995). *Cascade regulation of terminal adipocyte differentiation by three members of the C/EBP family of leucine zipper proteins*.

Yie, T. A., Loomis, C. A., Nowatzky, J., Khodadadi-Jamayran, A., Lin, Z., Cammer, M., Barnett, C., Mezzano, V., Alu, M., Novick, J. A., Munger, J. S., & Kugler, M. C. (2023). Hedgehog and Platelet-derived Growth Factor Signaling Intersect during Postnatal Lung Development. *American Journal of Respiratory Cell and Molecular Biology*, *68*(5), 523–536. https://doi.org/10.1165/rcmb.2022-0269OC

Zeng, X., Goetz, J. A., Suber, L. M., Scott, W. J., Schreiner, C. M., & Robbins, D. J. (2001). A freely diffusible form of Sonic hedgehog mediates long-range signalling. *Nature*, *411*(6838). https://doi.org/10.1038/35079648

Zhang, Q., Nishimura, D., Seo, S., Vogel, T., Morgan, D. A., Searby, C., Bugge, K., Stone, E. M., Rahmouni, K., & Sheffield, V. C. (2011). Bardet-Biedl syndrome 3 (Bbs3) knockout mouse model reveals common BBS-associated phenotypes and Bbs3 unique phenotypes. *Proceedings of the National Academy of Sciences of the United States of America*, *108*(51), 20678–20683. https://doi.org/10.1073/pnas.1113220108

Zhang, Q., Seo, S., Bugge, K., Stone, E. M., & Sheffield, V. C. (2012). BBS proteins interact genetically with the IFT pathway to influence SHH-related phenotypes (2012a). *Human Molecular Genetics*, *21*(9), 1945–1953. https://doi.org/10.1093/hmg/dds004

Zhang, Q., Yu, D., Seo, S., Stone, E. M., & Sheffield, V. C. (2012). Intrinsic protein-protein interaction-mediated and chaperonin-assisted sequential assembly of stable Bardet-Biedl syndrome protein complex, the BBSome (2012b). *Journal of Biological Chemistry*, *287*(24), 20625–20635. https://doi.org/10.1074/jbc.M112.341487

Zhao, M. L., Rabiee, A., Kovary, K. M., Bahrami-Nejad, Z., Taylor, B., & Teruel, M. N. (2020). Molecular Competition in G1 Controls When Cells Simultaneously Commit to Terminally Differentiate and Exit the Cell Cycle. *Cell Reports*, *31*(11). https://doi.org/10.1016/j.celrep.2020.107769

Zhao, X. K., Cheng, Y., Liang Cheng, M., Yu, L., Mu, M., Li, H., Liu, Y., Zhang, B., Yao, Y., Guo, H., Wang, R., & Zhang, Q. (2016). Focal adhesion kinase regulates fibroblast migration via integrin beta-1 and plays a central role in fibrosis. *Scientific Reports*, *6*. https://doi.org/10.1038/srep19276

Zhu, D., Shi, S., Wang, H., & Liao, K. (2009). Growth arrest induces primary-cilium formation and sensitizes IGF-1-receptor signaling during differentiation induction of

3T3-L1 preadipocytes. *Journal of Cell Science*, *122*(15). https://doi.org/10.1242/jcs.046276

9. Appendix

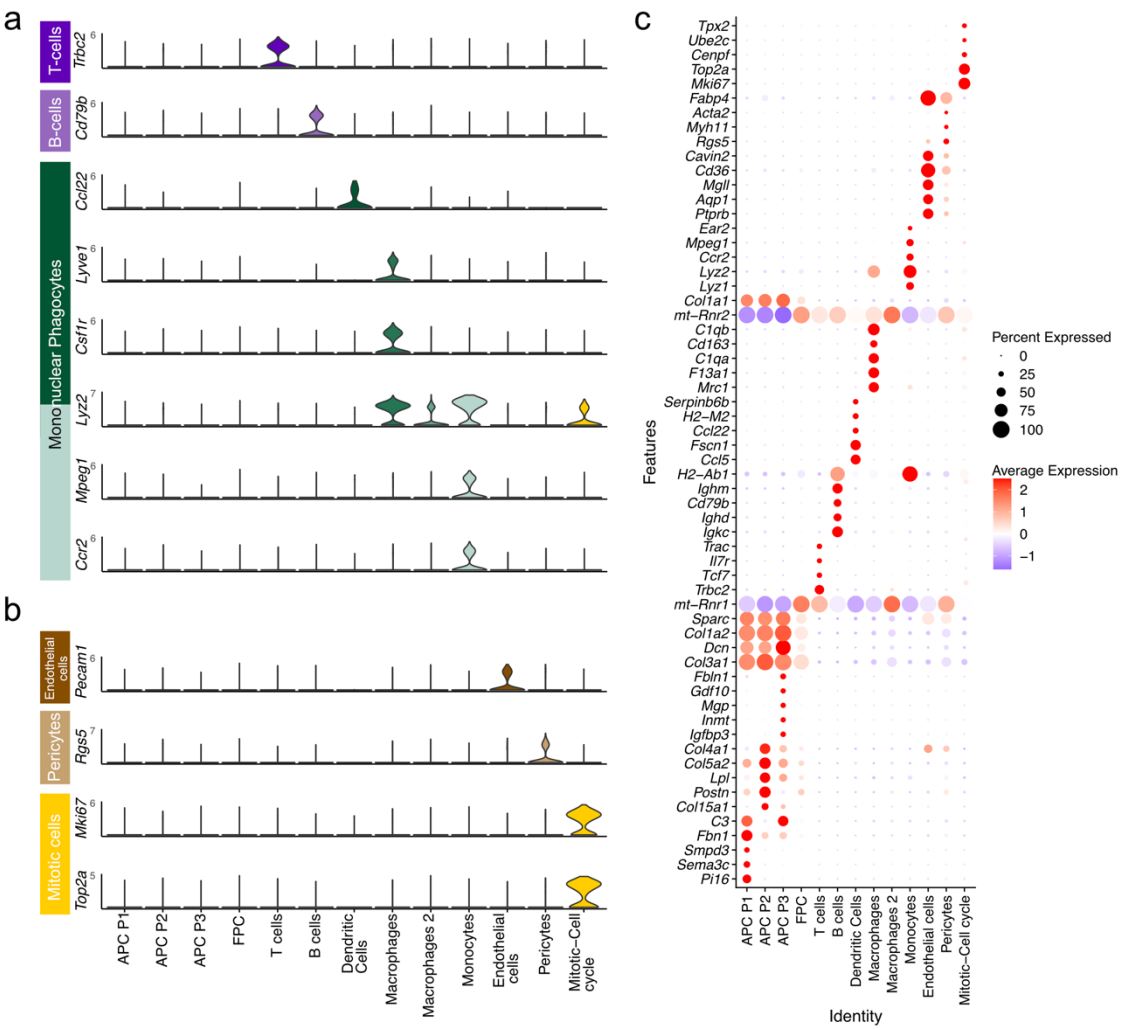

Fig. S1: Annotation of single-cell analysis of iWAT from lean *Bbs8*$^{-/-}$ mice. a-b. Violin plots of published markers for all (**a**) immune cell, (**b**) vascular and cycling cell cluster determined in Fig. 19 b**. c.** Dot plot for top 5 marker genes in all cell clusters determined in Fig. 19 b.

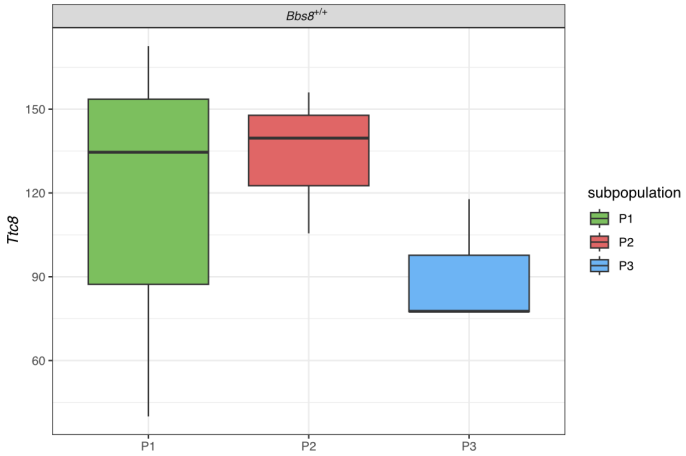

Fig. S2: *Bbs8* (*Ttc8*) expression in wild-type APC subpopulations. Expression level of the gene encoding for *Bbs8* (*Ttc8*) in APC subpopulations from *Bbs8*$^{+/+}$ iWAT. Data are shown as mean ± SD

10. Acknowledgement

This work was performed in the research group of Prof. Dr. Dagmar Wachten at the Institute of Innate Immunity from the University of Bonn.

In particular, I would like to thank the following people:

- Prof. Dr. Dagmar Wachten for the opportunity to work on this project and the outstanding supervision during these years. Her dedication to science has always inspired me to believe in myself and to try my hardest. Without her constant support, I would not be where I am today.
- Prof. Dr. Elvira Mass for her participation as formal supervisor and second reviewer in the examination committee, as well as for her input during the thesis committee. I also want to thank Elvira for being part of my scientific journey during my master program as well as during my PhD thesis.
- Prof. Dr. Eicke Latz for his participation as a third reviewer in the examination committee.
- Prof. Dr. Veronika Lukacs-Kornek for her participation as fourth reviewer in the examination committee.
- Prof. Dr. Jan-Wilhelm Kornfeld as a member of my doctoral thesis advisory committee (TAC), for his input and great scientific discussions.
- The Deutsche Studiensstiftung for funding my PhD.
- The Flow Cytometry Core Facility (FCCF) of the Medical Faculty of the University of Bonn for the help, service and equipment funded by the Deutsche Forschungsgemeinschaft (DFG, German Research Foundation). I especially want to thank Peter Wurst for his help in sorting all my subpopulations.
- The Microscopy Core Facility (MCF) of the Medical Faculty of the University of Bonn for the help, service and equipment funded by the Deutsche Forschungsgemeinschaft (DFG, German Research Foundation). Especially, I want to thank Dr. Gabor Horvath for answering every single question I had regarding the microscopy.
- The Core Unit for Bioinformatics Data Analysis (CUBA) of the Medical Faculty of the University of Bonn help, service and equipment funded by the Deutsche Forschungsgemeinschaft (DFG, German Research Foundation).

- The Histology Platform of the Medical Faculty of the University of Bonn for their help, service, and the instruments.
- Dr. Nora Winnerling for supervising me beginning from my first lab rotation until my PhD thesis. Nora was a big reason to start my scientific career, and I am deeply thankful for her emotional support.
- Dr. Dalila Juliana Silva Ribeiro for her scientific input during my PhD and in helping my while writing the thesis. I also want to thank her for her friendship, that I can always talk to her and for her constant emotional support.
- Ronja Kardinal for knowing I can always count on her help and her friendship and emotional support throughout these years.
- Maximilian Rothe and Romina Kaiser for their great support with the mouse work and other experiments.
- All current members of the Wachten Lab for their help and support. Especially Fabian Frechen, Seniz Yüksel, Ernesto Galindo-Picon, and Rudolfo Karl.
- Dr. Fabian Kaiser, Dr. Christina Klausen, Dr. Mylene Hübecker, Dr. Jan-Niklas Hansen, Kim Dressler, and all other former members of the Wachten Lab for supporting me in the early stages of my PhD and for their friendship throughout.
- Dr. Nelli Blank from the Mass Lab, for her help in generating the single-cell RNAseq data.
- Dr. Jelena Zurkovich from the Thiele Lab, for her work in generating the lipidomics data.
- Dr. Lisa Steinheuer from the Thurley Lab, for helping me analyze the single-cell RNAseq data and for interesting scientific discussions.
- Dr. Geza Schermann and Prof. Dr. Carmen Ruiz Vasquenz de Almodovar for helping me analyze the single-cell RNAseq data and for interesting scientific discussions.
- Florian Barnikel für seine Liebe, seine emotionale Unterstützung und, dass er immer für mich da ist, egal ob es mir gut oder schlecht geht.
- Ich danke meiner gesamten Familie, dir mir immer Rückhalt gegeben hat. Besonderer Dank meinen Eltern Margit Lang und Ralf Sieckmann, durch deren Unterstützung ich immer sorglos durch mein Leben schreiten konnte.